HgTe shells on CdTe nanowires

A low-dimensional topological insulator from crystal growth to quantum transport

Dissertation

zur Erlangung des naturwissenschaftlichen Doktorgrades
der Julius-Maximilians-Universität Würzburg
vorgelegt von

Maximilian Kessel
aus Neuss

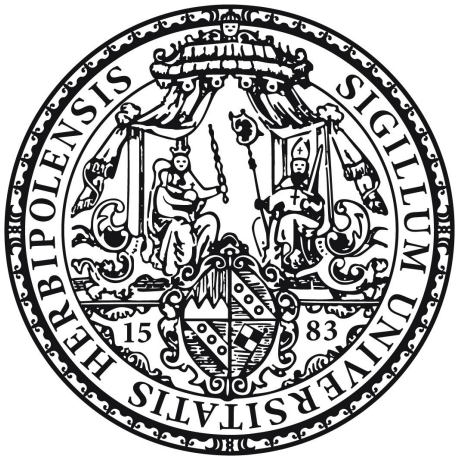

Würzburg, 2016

Eingereicht am: 23.11.2016

bei der Fakultät für Physik und Astronomie

1. Gutachter: Prof. Dr. Hartmut Buhmann

2. Gutachter: Prof. dr. hab. Grzegorz Karczewski

3. Gutachter: –

der Dissertation

Vorsitzender: Prof. Dr. Sven Höfling

1. Prüfer: Prof. Dr. Hartmut Buhmann

2. Prüfer: Prof. dr. hab. Grzegorz Karczewski

3. Prüfer: Prof. Dr. Björn Trauzettel

im Promotionskolloquium

Tag des Promotionskolloquiums: 19.05.2017

Doktorurkunde ausgehändigt am:

To get the results presented in this thesis,
approximately 10^{10} CdTe nanowires have been grown
in more than 100 growth runs.
Stagged in one row, they would have a length of about 10 km.
One third of them are shelled with HgTe.
Metallic contacts are defined for hundreds of nanowires
and thousands of images were recorded with the electron microscope.

Contents

III Integration of nanowires into electronic circuits

IV Charge transport in HgTe nanowires

Summary and outlook

Appendix

Introduction

Topological insulators (TIs) are a fascinating field in condensed matter physics. These materials have insulating bulk, but host conductive surface states. They are very interesting due to the topologically protected nature,[1] having distinct properties such as spin-momentum locking.[2, 3] Furthermore characterized by a linear energy dispersion, the surface states can be described like Dirac-fermions. Recently, many theoretical and experimental contributions discuss TIs.[4] Two-dimensional, [5, 6] bulk-like [7, 8] and quasi-one-dimensional [9, 10] TIs are a quite new field, but they already attracted a lot of attention.

As introduced above, an ideal TI has an insulating bulk. However, in many material systems, charge transport investigations reveal a significant bulk contribution. Some topological materials, such as Bi_2Te_3 and Bi_2Se_3, tend to be unintentionally doped and show low carrier mobility. With that, the predicted properties of surface transport are obscured by the contribution of bulk carriers. Contrary, strained HgTe layers show very mobile surface states at low charge carrier density.[11] Compared to a sample with macroscopic volume, the properties of the surface play a larger role for mesoscopic samples like nanowires (NWs). They are now in focus, as the NW geometry gives rise to additional periodic boundary conditions for the surface state along the short perimeter of the NW.

Generally, the reduction of size increases the surface to volume ratio. The ratio is further enhanced for a TI formed in the shape of a tube, making CdTe NWs shelled with the TI HgTe promising candidates to observe phenomena related to the surface states. Strained HgTe has proven to be a high-mobility TI in two- and three-dimensional structures.[6, 11] We report on a novel growth method for quasi-one-dimensional heterostructures containing the TI material HgTe. The concept of a hollow TI NW, having a trivial insulator as a core, is realized in this thesis for the first time.

The semimetal HgTe develops an energy gap for bulk charge carriers under strain or constriction to low dimensions. The energy gap for electronic bulk states in HgTe is

approximately proportional to the uniaxial strain, reducing the symmetry of the zinc blende unit cell. Regarding this restriction, a free-standing and relaxed HgTe-NW has bulk conductance. To open a bulk energy gap, we grow free-standing CdTe NWs and use them as a core to strain an epitaxial HgTe shell. The bottom-up approach has many advantages compared to a top-down fabrication, because low dimensional structures fabricated by lithography are usually damaged by the processing. If the size is determined by self-organized growth mechanisms, then the core-shell interface is of high epitaxial quality.

Beside the fundamental research on TI states in low dimensions, the heterostructures have promising properties for developing optoelectronic devices. The possibility to tune the band gap in the quaternary (Hg,Cd,Zn)Te system and the high surface to volume ratio reached by nanowires allow for the realization of effective photodetectors with a wide spectral range. In both cases, first the fundamental research on TIs and second the development of functional devices, the crystalline quality and strain play a crucial role for the properties of the heterostructures.

Boundary conditions in mesoscopic heterostructures can be used as building blocks to achieve the desired electronic structure. One example is the periodic condition for the surface states of a NW, which allows to tune the band dispersion in a device.[9] To give another example, quasi-one-dimensional TIs are predicted to host Majorana bound states in combination with a superconductor.[12, 13] Their detection and manipulation attracted a strong interest because of anyonic braiding statistics. For this reason, Majorana states are possibly the basis for a topological quantum computer.[14] But before thinking about applications, they primarily can serve to analyze Majorana physics in condensed matter and to prove the concept of a particle existing, that is its own antiparticle.

This manuscript gives methods for growing high-quality NW heterostructures and furthermore to integrate the NWs into electronic circuits. Different microscopical and diffractive methods are used to characterize the samples. We analyze the surface and crystal structure of both the CdTe core and the HgTe covered heterostructures. The developments in NW manipulation and device fabrication allow us to characterize the samples by charge transport measurements. We investigate transport with ohmic contacts. Furthermore, hybrid NW/superconductor structures are achieved, showing non-linear I-V characteristics. Results on charge transport are discussed at the end of this thesis. This first characterization of the HgTe-based NWs is a very promising base for the ongoing research.

Part I

Growth of CdTe nanowires with HgTe shells

1 State-of-the-art

Molecular beam epitaxy (MBE) is a very precise method for the growth of crystalline heterostructures down to atomic resolution. It is used for the growth of epilayers over a wide range of materials in recent decades.[15, 16] The growth chamber setup, which is used for the growth of samples containing HgTe, is explained in prior work.[19] Performed under ultra-high-vacuum (UHV) conditions, MBE allows for the growth of materials with controlled doping. The supplied materials have highest purity and behave beam-like in UHV. To grow a single crystal, the main challenge is to correctly tune the thermodynamic equilibrium of adsorbate adsorption, incorporation into the crystal and desorption from the surface.[17] To do so, the substrate temperature is set specifically. This can be very delicate and slightly detuned conditions usually result in a high defect density. Defects can be point like, as for example vacancies, or extend over the entire crystal like a grain boundary. They are normally not intended as they alter the local electronic structure.[18]

One-dimensional crystallites can be grown with MBE by using a liquid catalyst droplet. For vapor-liquid-solid (VLS) growth, the thermodynamic equilibrium is tuned towards desorption by increasing the substrate temperature compared to layer MBE. Additionally, liquid droplets on the surface of the substrate are needed to catalyze nanowire (NW) growth.[20, 21] Their three-dimensional shape and liquid phase allows to carry much higher amounts of solved adsorbate compared to the bare surface. If the temperature is set correctly, then the concentration of solved materials reaches the solubility limit. If furthermore the energy for a nucleus is lowest at the interface to the substrate, then a single one-dimensional crystallite grows.

In this manuscript, focus is on low-dimensional HgTe-CdTe heterostructures. The growth of such crystals is challenging due to the narrow limits for single-crystalline growth. Heterostructures in this material system have attracted strong interest, as they host topologically protected electronic states.[6, 22] HgTe is a semimetal with inverted band order. The Γ_8 bands are degenerated and have a higher ground state energy compared to the Γ_6 band. CdTe is a semiconductor with trivial band order $E_{\Gamma_6} > E_{\Gamma_8}$. These two zinc blende materials show a small lattice mismatch of

0.3%. Residual lattice strain is expected in mismatched core-shell NWs.[23] Uniaxial as well as shear strain lifts the degeneracy of Γ_8 states.[24, 25] This opens a bulk energy gap. Thus, strain turns the topological semimetal HgTe into a topological insulator.[11, 26] HgTe hosts the mentioned conductive surface states with a strong spin-momentum coupling and highly mobile carriers as a consequence of the band order inversion. If the Fermi-level is within the strain-induced energy gap for bulk charge carriers, then charge transport through the NW is governed by the surface states. Prior publications on HgTe focus on quantum wells [6] or bulk like samples [27, 28]. The self-organized growth of HgTe-NWs having minor crystal quality was reported already.[35, 36] In this work, a novel growth method is developed, allowing for the strained growth of quasi-one-dimensional HgTe on CdTe NWs. For this reason, free-standing CdTe NWs with a preferred orientation to the substrate are needed to ensure a uniform overgrowth with HgTe.

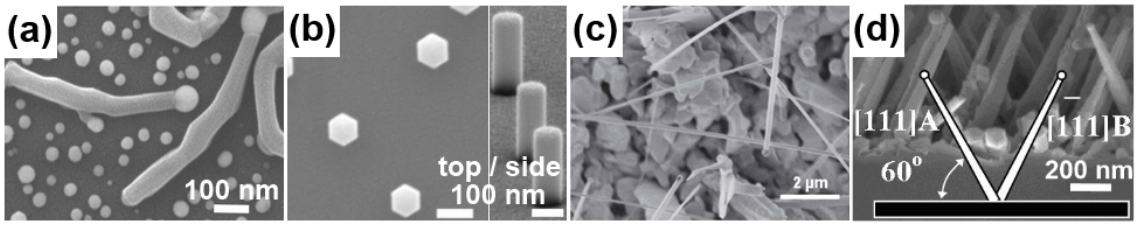

Figure 1.1: Prior attempts to grow CdTe NWs resulted in (a) laterally growing NWs, (b) small wurtzite NWs or (c) NWs without preferred orientation to the substrate.[29, 30] (d) Free-standing ZnTe-based NWs with preferred growth direction were reported.[33]

The self-organized growth of straight, free-standing, aligned and single crystalline zinc blende CdTe NWs with a high ensemble uniformity is not reported in literature so far. Figure 1.1 gives an overview on prior attempts to grow II-VI NWs. CdTe NWs show a tendency to grow laterally on the substrate, shown in (a). Short vertical CdTe NWs with wurtzite crystal structure in (b) have been demonstrated by altering the substrate preparation.[29] Other attempts in (c) achieved free-standing zinc blende CdTe NWs, but they were randomly oriented.[30] Wojtowicz *et al.* showed, that CdTe NWs can be grown on ZnTe NWs.[31] In (d) we see that such ZnTe NWs can be grown along <111> on GaAs substrates with a Gold-based catalyst.[32, 33] This approach is now refined to achieve the high CdTe NW ensemble uniformity presented in this work. The quality of the CdTe NWs obtained by the novel method allows for epitaxial HgTe overgrowth. The next chapter gives a recipe to grow the samples that are analyzed for crystalline strain and charge transport phenomena later.

2 Novel growth method

For one-dimensional CdTe growth by the VLS method, the substrate temperature turned out to be the most critical parameter during the growth process. If the temperature is set correctly, then straight NWs grow oriented along [111]B. Reflection high-energy electron diffraction (RHEED) is introduced as an effective tool additionally to the standard thermocouple, allowing for the required enhancement of temperature control. Subsequently the CdTe NWs are overgrown with HgTe shells.

Starting point of the experiments are Si doped GaAs substrates with (001), (110) and (111)B orientation glued to the sample mount by a liquid metallic film. The wafers are transferred into an UHV cluster. Three individual "Riber" MBE chambers (for III-V, wide- and narrow-gap II-VI materials) and a metallization chamber are used for preparation and growth process. Within the cluster, all samples are transferred without contact to air. Each MBE chamber is equipped with a RHEED system. The electron energy is 12 keV. RHEED patterns are recorded during different stages of growth. The electrons heat the wires, because only a small fraction is reflected. This additional heating affects the growth. Thus, the time the NWs are exposed to the electron beam must be short. A CCD camera is used to record a RHEED screen series during one full sample rotation.

Inside the MBE for III-V materials, the native oxide is thermally removed from the substrate, followed by the deposition of 0.4 to 1.0 nm Au in the metallization chamber. The NWs grow inside the MBE for wide-gap II-VI materials. One-dimensional growth is seeded by liquid Au-Ga droplets, formed by heating to 480 °C with a ramp rate of 50 K/min. This temperature is measured with a thermocouple at the backside center of the substrate mount. Then, the NWs grow with beam equivalent pressures in the range of $5{\cdot}10^{-7}$ to $1{\cdot}10^{-6}$ mbar. The droplets move and merge, pushed by lateral ZnTe growth for which we use a Zn:Te beam pressure ratio of 0.6:1 at 400 °C substrate temperature. The redistribution of droplets during the growth start is discussed in the next chapter. After 2 min, Zn is replaced by a Cd flux with a Cd:Te beam pressure ratio of 1.2:1. At a substrate temperature of 400 °C, CdTe growth is suppressed completely. At this stage no growth occurs, providing

controlled starting conditions. Layer growth remains suppressed during the whole process, but straight CdTe NWs grow within a narrow temperature limit slightly below 400 °C. In order to find the narrow limits, the temperature is lowered stepwise by 1 K every 10 min. A transition in the RHEED pattern indicates, that optimal growth conditions are established. The measured optimized substrate temperature is around 395 °C. Now the vertical CdTe NW growth takes place and the sample's radiative loss of energy changes significantly while the NWs grow. During growth, the substrate temperature is slowly increased by about 2 K/h for about 3 h to compensate this effect. For long NWs, most radiated heat remains in the ensemble, so the substrate temperature is constant at about 400 °C at the end to grow long NWs. The thermodynamics of NW growth are investigated in Chapter 4.

Finally, the CdTe NWs are epitaxially overgrown in the MBE for narrow-gap II-VI materials at 185 °C substrate temperature. For different samples, the Hg:Te ratio is varied precisely from 100:1 to 400:1 by a homebuilt Hg-cell. Hg is supplied with a beam equivalent pressure in the range of $1{\cdot}10^{-4}$ to $6{\cdot}10^{-4}$ mbar. With a Hg:Te ratio close to 200:1, HgTe grows on polar CdTe NW sides of opposite polarity forming a continuously closed shell, depicted by the scanning electron microscope (SEM) images in Fig. 2.1. A higher Hg:Te ratio suppresses growth on the B-polar NW facets resulting in a different heterostructure geometry. An electron beam is found to strongly affect the HgTe growth, therefore RHEED is not possible. Chapter 5 gives details on the growth process and the shell geometry.

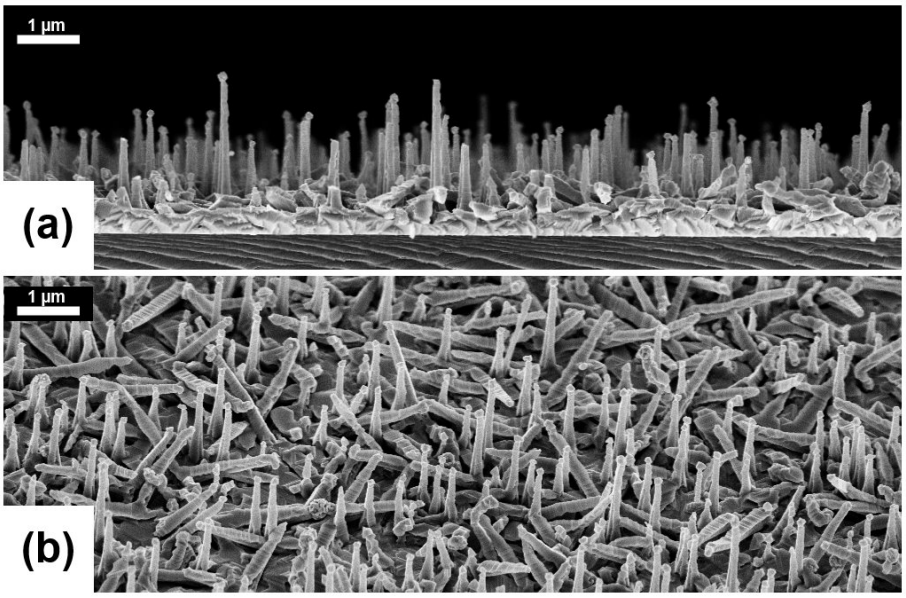

Figure 2.1: Images with (a) 90° and (b) 45° view angle of CdTe NWs with a HgTe shell grown by the novel method on a (111)B substrate.

3 Growth start details

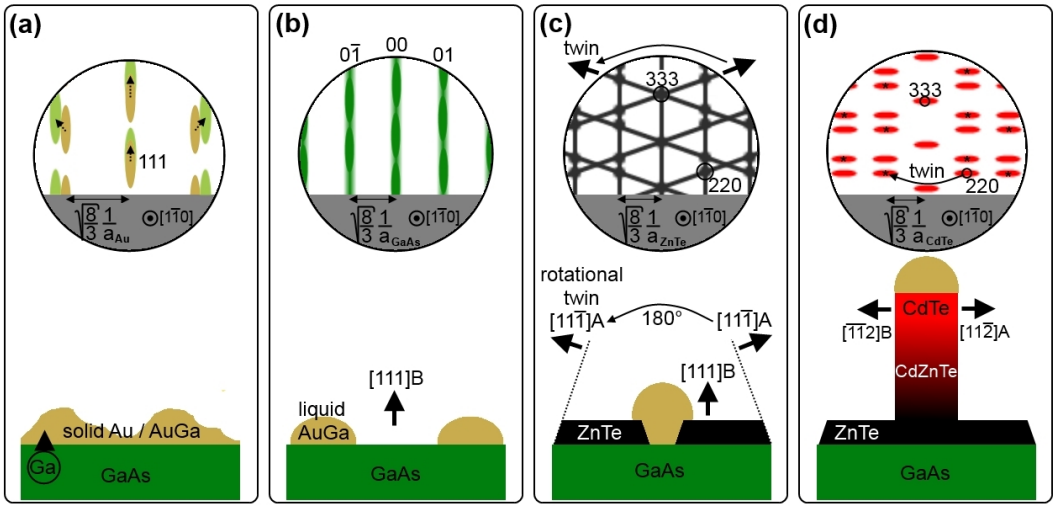

Figure 3.1: Illustration of RHEED screen and sample morphology during the growth process on a (111)B oriented substrate. By heating solid Au on GaAs in (a), liquid catalysts form in (b). In (c) the droplets redistribute by lateral growth of twinned ZnTe, followed by the growth of vertical CdTe NWs in (d).

The preparation results in oxide-free and Au wetted GaAs substrates, which are transferred into a MBE chamber, where the samples are heated to form the liquid growth seeds. In the beginning, the diffraction spots of rough, solid and twinned cubic Au can be observed, schematically shown in Fig. 3.1 (a). The formation of a Au-Ga solid solution is linked to a decrease of the lattice constant with increasing Ga content.[39] An expansion of the reciprocal lattice on the RHEED screen by approximately 15% while going from 350 °C to 400 °C substrate temperature shows, that Ga diffuses into the Au layer. While the temperature rises further, the diffraction spots vanish with the melting of the Au-Ga eutectic. At about 430 °C, small droplets are formed due to surface tension. As shown in Fig. 3.1 (b), this dewetting process leads to uncovered GaAs areas. Therefore, the RHEED pattern of the GaAs surface becomes clearly visible. The liquid droplets obtained are the seeds for the subsequent NW growth.

After Au-Ga droplet formation, the substrate temperature is stabilized at 400 °C. Subsequently, fluxes of elemental Zn and Te are supplied. Small lateral structures grow in the vicinity of the droplets, pushing the droplets across the substrate. These structures coalesce and several droplets merge to one. The density of the droplets decreases by roughly an order of magnitude during the first 2 min of growth. Small structures with catalytic droplets on ZnTe {111} facets are formed. This is verified by SEM images and RHEED diffraction pattern and is schematically shown in Fig. 3.1 (c). Now Zn is replaced by Cd to grow free-standing CdTe NWs as depicted in Fig. 3.1 (d).

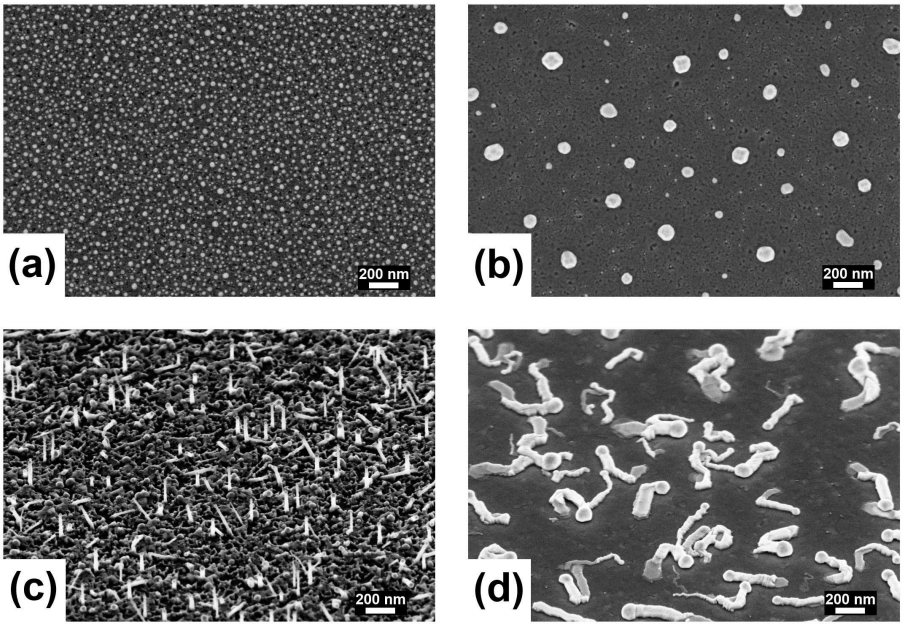

Figure 3.2: Top view of droplets formed by dewetting of (a) thin Au and (b) the same Au amount, covered by a thick amorphous Zn layer. ZnTe wires grown from (c) dense and (d) remote droplets are shown with an 45° perspective.

Alterations to the described starting sequence are tested, intended to explore the limits of controlling the NW density. Intuitively, the density of vertically grown NWs mainly depends on the density of droplets. Figure 3.2 compares the initial droplet distribution with the NW outcome for two differently prepared samples. For thin metallic layers, the surface is not wetted perfectly, which leads to a high droplet density in Fig. 3.2 (a). If the droplet density is high, then each droplet has a small volume. If the Au-layer is covered by a rather thick layer of amorphous Cd, Zn or Te before heating, then the droplet density is significantly lower. To give an

example, Fig. 3.2 (b) shows a sample having the same amount of Au as in (a), but a thick amorphous Zn layer was deposited before heating. During melting of the thick metallic layer, a continuous liquid film is formed. This allows for the formation of remote eutectic droplets of larger volume. The Cd, Zn or Te content is decreasing again by keeping those droplets at an elevated temperature. Figure 3.3 (a) to (c) summarize the processes, which influence the droplet density.

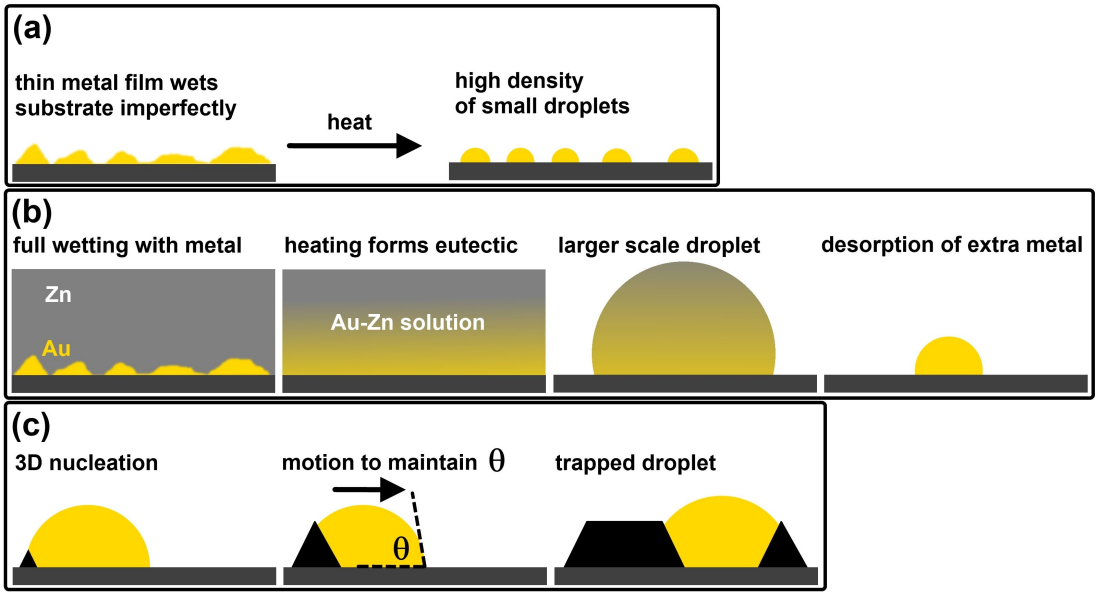

Figure 3.3: The droplet distribution is determined by (a) imperfect or (b) full initial wetting and (c) the lateral movement of droplets.

Proceeding with growth for the differently prepared droplets, we only observe vertical wire growth for the dense droplets. The samples obtained are shown in the lower images of Fig. 3.2. Initially, the NWs grow laterally on the substrate surface for both droplet arrangements. For dense droplets, the growing structures collide and some free-standing NWs grow in Fig. 3.2 (c). Wires grown from remote droplets have a low chance for multiple collisions and we only observe lateral growth. Regarding this observation, the coalescence of ZnTe structures grown from dense droplets seems to be very important to ensure vertical wire growth. The vertical growth is triggered by the localization of droplets in a self-grown ZnTe trap. On a flat substrate in Fig. 3.2 (d), remote droplets are pushed over the bare surface by growing ZnTe. Driving force of this motion is the surface tension of the droplet, which is altered locally by the growing solid nucleus. ZnTe grows as three-dimensional islands on GaAs to avoid strain caused by the lattice mismatch of both materials.[40, 41] The three-dimensional nucleus deforms the droplet, resulting in an asymmetric surface curvature. Curvature and surface tension are directly connected. To get back to

equilibrium and in order to maintain the wetting angle θ between solid and liquid, the deformed droplet needs to move. This motion proceeds until the asymmetric deformation by a single nucleus is compensated.

The detailed analysis in Chapter 6 shows, that crystallites of hexagonal Gallium-Telluride (h-GaTe) grow, when Ga-containing droplets are exposed to a Te flux. Looking carefully in Fig. 3.2 (d), a very flat part grows in the beginning. Different morphology and contrast indicate the switching to ZnTe. With our method, growth starts with a few layers h-GaTe until Zn saturation is reached or Ga is consumed. Being a layered van-der-Waals crystal, the flat morphology is in agreement with this finding. But for a flat nucleus, the argument of a three-dimensional structure altering the local curvature of the droplets no longer explains the lateral movement of the droplets. A h-GaTe nucleus might not change the curvature of a liquid droplet geometrically, but by altering the local surface potential. The potential on a bare GaAs surface with open bonds is different to the one on the van-der-Waals crystal h-GaTe, which has no bonds on the surface. The surface potential μ between a solid and a liquid has major influence on the contact angle θ and can be the driving force for self-propelled motion.[42, 43] Fig. 3.4 sketches the relation of surface potential, contact angle, curvature and motion.

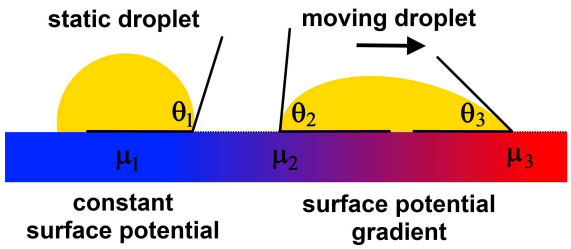

Figure 3.4: Relation of surface potential μ and wetting. For a gradient in surface potential, the contact angle θ is different on both sides of a droplet and the asymmetrically increased surface tension pushes the droplet.

The growth seed is found to be a superconducting alloy of unknown composition. After the complete growth process, it can be an alloy of all supplied metals (Au, Ga, Zn, Cd, Te and Hg). Charge transport measurements on NW/droplet junctions are discussed in Chapter 16. To the knowledge of the author, this is the first time, the droplet seeding VLS growth, is used as a superconducting contact in the final device.

Now we know, how the droplets are formed and trapped, to finally seed vertical wire growth. The following growth process requires fine tuning of the substrate temperature, which is explained in the next chapter.

4 Thermodynamics of growth

High quality CdTe NW growth requires a specific substrate temperature and is very sensitive for thermodynamic changes. CdTe growth is suppressed for temperatures around 400 °C. In a range of about 5 K below that temperature, when NW growth starts slowly, straight and uniform CdTe NWs grow along [111]B. The growth rate is highly temperature dependent. Growth rates of up to 0.2 nm/s are observed for straight wires with substrate temperatures around 395 °C. If the temperature at the growth front is too low, then the NWs' growth direction changes randomly and the wires show pronounced kinks. In order to achieve straight growth, the substrate temperature has to be controlled more precisely than by the indirect measurement with a thermocouple. By carefully studying the RHEED in many growth runs with varied temperatures and the comparison to the outcome by the SEM, we learn to interpret the diffraction pattern correctly. Doing so, we are now able to infer optimal growth conditions from the RHEED. Straight NWs show a characteristic pattern, which can be discerned from patterns obtained suppressing growth at high temperatures and from kinked NWs at low temperatures.

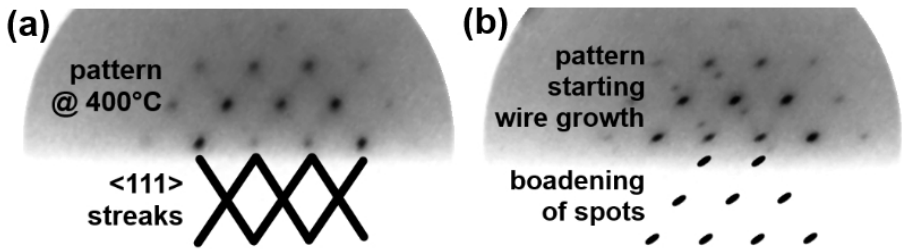

Figure 4.1: RHEED screen for (a) hot conditions suppressing CdTe growth and (b) optimized conditions with growing CdTe NWs. For better contrast, the images are inverted and schematically pointed out below.

In order to adjust the right conditions for straight CdTe NWs, the RHEED is monitored at substrate temperatures of 400 °C and below. As long as one can see broad and diffuse lines of {111} facets, which are shown in Fig. 4.1 (a), the substrate is too

hot. If the lines are even more clearly visible on the RHEED screen compared to the given example, then the substrate temperature needs to be decreased by several degrees. The <111> streaks are caused by diffraction during reflection from the lateral ZnTe structures. To proceed with vertical CdTe NW growth, the temperature is lowered stepwise. Somewhere between 400 °C and 390 °C, the <111> streaks vanish as the lateral structures are obscured by the vertically growing NWs. Instead, the pattern of NWs growing along [111]B becomes visible. The characteristic diffraction spot broadening perpendicular to the NW growth axis is shown in Fig. 4.1 (b). If the spots broaden like this, then the substrate temperature is adjusted correctly. The measured optimized temperature is different for each process. Most of the samples show the characteristic CdTe NW RHEED, which is depicted in Fig. 4.2, at temperatures around 395 °C.

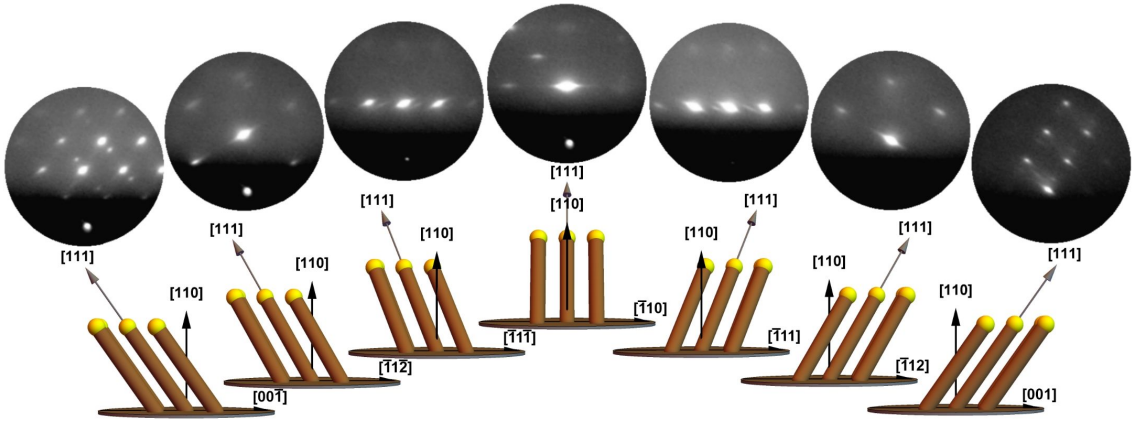

Figure 4.2: High symmetry diffraction patterns of CdTe NWs growing along [111] on a (110) oriented GaAs substrate for 180° azimuthal rotation. The diffraction spots are always broadened perpendicular to the NW growth axis.

The broadening of the diffraction spots in Fig. 4.1 and 4.2 is a size related effect. The NWs have a diameter of 30 to 80 nm and are too thick, compared to the penetration depth of electrons, in order to get a signal from the center. Therefore, the transmission diffraction spots origin from the thin NW rims, penetrated by the beam. If the NW length is much larger than the penetration depth, then the diffraction spots broaden perpendicular to the NW growth direction. After switching from Zn- to Cd-supply, the lattice constant changes gradually from ZnTe to CdTe within 20-30 min of growth corresponding to a 100-300 nm long transition region. This observation is explained by a container effect for Zn in the eutectic droplet described by Krimse *et al.*[44] In this sense, a container effect means, that after switching to Cd, the Zn solved in the droplet is consumed by crystal growth over time. The probability for

the incorporation into the crystal depends on the Zn concentration in the droplet, asymptotically decreasing to zero while the residual Zn is consumed. The influence of this effect on the crystal structure of the CdTe NWs is investigated in Chapter 10.

One can see additional lines in the diffraction pattern in Fig. 4.2, as the NWs probed here are grown long enough to develop sufficiently large side facets, which reflect the electron beam. Being caused by diffraction during reflection, these lines are perpendicular to the NW surfaces. The symmetry and periodicity of the NW surfaces is analyzed by RHEED in detail in Chapter 8. During growth, the feedback from RHEED is used for finding and maintaining the narrow temperature limits of the CdTe-VLS growth process.

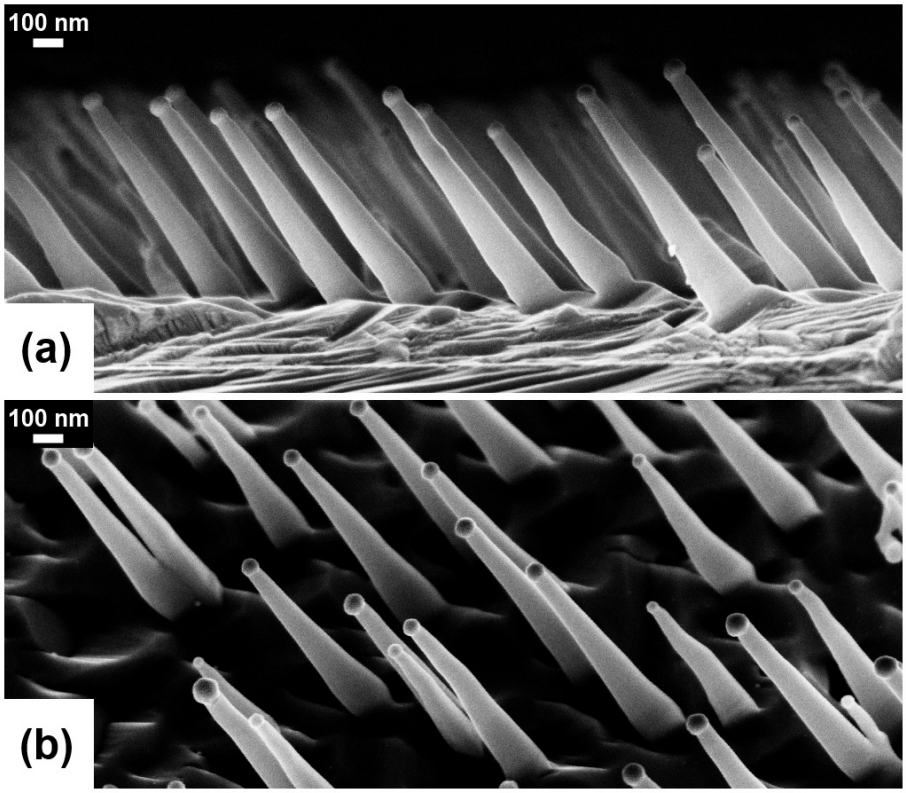

Figure 4.3: SEM images with (a) 90° and (b) 45° view angle of CdTe NWs on a (110) substrate grown RHEED controlled for 3 h. The substrate temperature was increased during growth, guided by changes in the RHEED.

The challenges arising for uniform and straight growth over several hours, in order to get longer NWs, are mainly due to the poor thermal conductivity of our material. For CdTe it is two orders of magnitude lower than for GaAs. For NWs, the thermal conductivity is even reduced compared to bulk material.[45, 46] Consequently, the ra-

diative heat loss along each wire plays an important role for the actual temperature at the growing wire's tip. The heat dissipation of a surface at a given temperature difference to its surrounding is mainly determined by the area of that surface. As NWs emerge on the substrate, the effective surface area increases drastically and with that the dissipated heat. To compensate this effect, the substrate temperature is continuously increased. Different ramp rates for the substrate temperature are tested. Depending on substrate orientation and wire density, a linear increase by 1-2 K/h for the first 3 h of growth is suitable to preserve straight growth. Figure 4.3 shows CdTe NWs grown under optimized conditions, where the temperature increase during NW growth is controlled by RHEED for a total of 3 h of growth. The growth rate for straight and single crystalline CdTe NWs is in the order of 0.1-0.2 nm/s. Lengths of up to 2.5 µm are achieved within a total of 6 h of growth. Figure 4.4 (a) is a SEM image of CdTe NWs grown without increasing the substrate temperature. The tips of the wires get colder, while the wires grow and they kink multiple times after a certain length of straight growth.

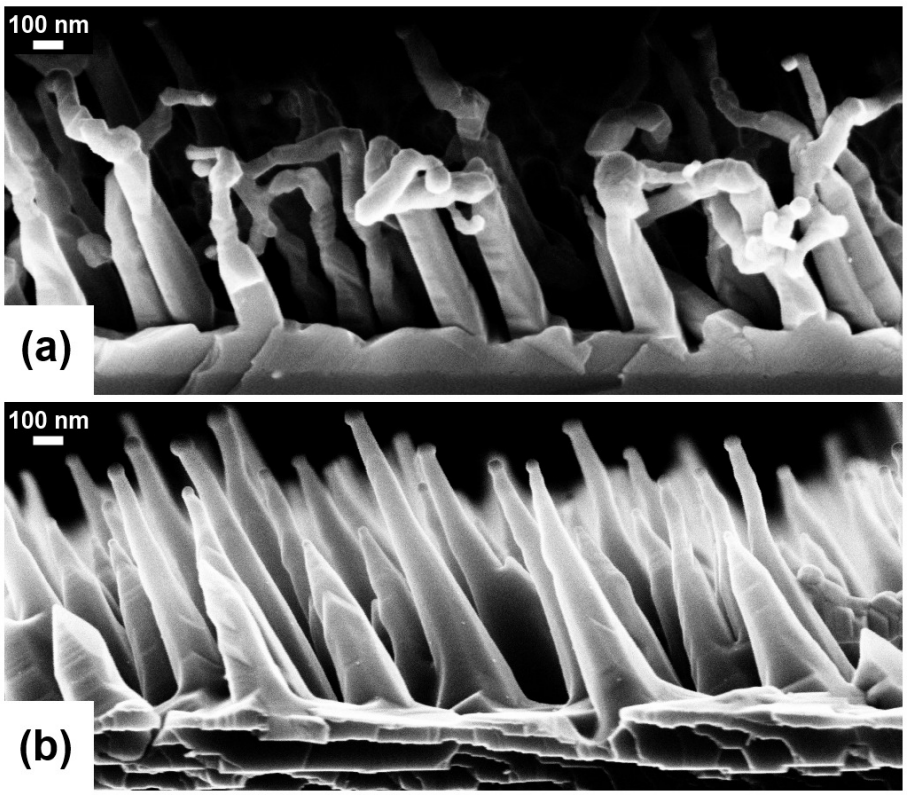

Figure 4.4: SEM images with 90° view angle of CdTe NWs grown on a (110) substrate (a) at constant temperature for 2 h and (b) with an increase of more than 2 K/h for 4 h.

For very long NWs, the situation is a bit different. With increasing length, the spacing-to-length ratio of the NW ensemble decreases and more and more heat radiated by an individual NW is reabsorbed by adjacent NWs, thus is remaining in the system. After 3 h of growth, corresponding to NWs longer than 1 µm, the growing ensemble radiatively behaves like a closed layer again. Based on this observation, samples with finally 2 µm long NWs grow at a constant substrate temperature of about 400 °C for another 3 h. If the temperature is further increased, then axial CdTe NW growth slows down, comparable to the growth rate of the radial growth. The pyramidal morphology of NWs grown under hot conditions is shown in Fig. 4.4 (b). The NWs have this shape, if the axial growth rate is less than 0.1 nm/s.

In summary, crystalline CdTe NWs can be grown by VLS MBE. For straight and long wires, the substrate temperature has to be controlled individually for each sample. RHEED is the most useful tool to monitor every step during preparation and growth. It gives real time feedback to react on changes in growth conditions caused by an alteration of the radiative energy loss with increasing NW length.

Since the wires loose power radiatively and heat dissipates slowly along the wires, the substrate temperature needs to be increased to keep the growing tips at a constant temperature. Free charge carriers would increase the heat transport along the wire drastically, otherwise carried only by phonons. Regarding the poor thermal conductivity, we do not expect charge transport in CdTe NWs without a shell. To test this, some CdTe NWs were contacted similar to the methods described in Part III. They show room temperature resistances in the MΩ range. In Part IV: "Charge transport in HgTe nanowires", the NW core is considered to be an insulator. The observation of no free charge carriers is in agreement with the poor thermal conductivity of the growing CdTe NWs.

Since the core determines the quality of the HgTe shell, this work also focuses on the characterization of the surface and bulk crystal structure of the CdTe NWs. The results are presented in Part II: "Crystallography". The crystallographic analysis not only gives insight to the inner structure of the grown samples, it also gives feedback to find the optimized growth recipe. The obtained RHEED proves the high crystal quality of the grown NW ensembles making them ideal candidates for HgTe overgrowth, which is discussed in the next chapter.

5 HgTe epitaxy on CdTe nanowires

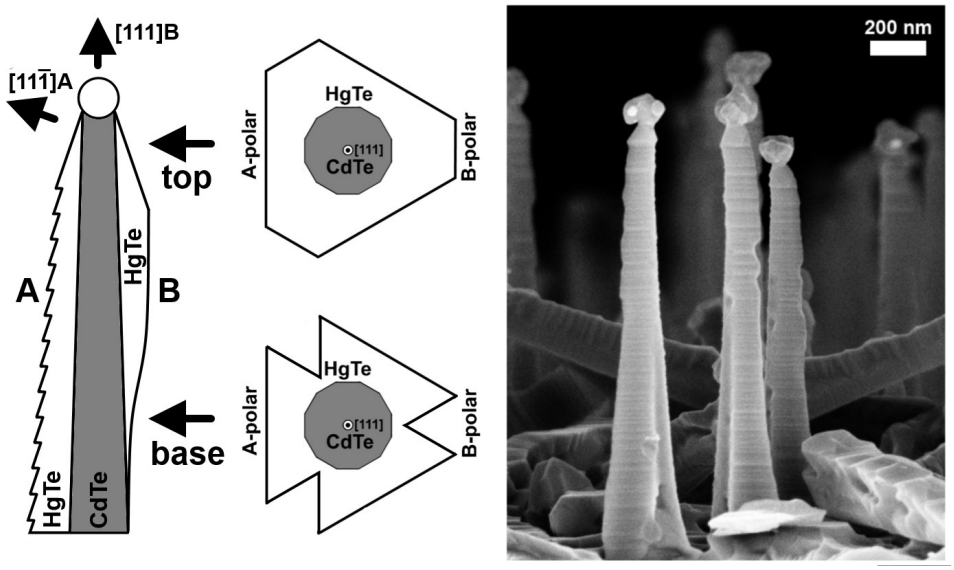

Figure 5.1: Cross-sectional schematic and SEM image of a closed HgTe shell around CdTe NWs on a (111)B substrate.

We find the growth of Hg-containing materials to be delicate, as briefly explained in the following.[47] Mercury has a low binding energy in most compounds. Only a very small fraction of supplied Hg atoms is incorporated into the growing crystal and instead many of them desorb from the substrate again. HgTe MBE requires relatively low growth temperatures of about 185 °C.[48] The sticking probability of Hg depends strongly on substrate polarity and substrate temperature. It is furthermore much smaller than that of Te.[49, 50, 51] The multifaceted nature of our NWs requires special attention to achieve single crystalline HgTe epitaxy on all facets. The twelve CdTe NW side-facets, which are investigated in Chapter 8, have alternating polarity: A-polar (group II terminated), non-polar, B-polar (group VI terminated), non-polar etc. By supplying a Hg:Te ratio of 200:1, a continuous HgTe shell grows. The nucleation starts at both polar types of facets. Adjacent non-polar facets are overgrown subsequently. CdTe NWs with continuous HgTe shells on a (111)B substrate are shown in Fig. 5.1.

Different growth rates on the polar sides lead to the characteristic shape. With HgTe overgrowth, the stepped A-polar surface exhibits larger faceted steps, resolved by the SEM. The angle between the A-polar $(11\overline{1})$ steps and the NWs' growth direction is determined by the crystal structure. For B-polar NW facets, no pronounced steps are observed in the SEM. From tip to base, the growth rate of HgTe is reduced gradually on B-polar facets and the reduction leads to uncovered areas near the NW bases, as shown in Fig. 5.1. Observations on the growth rate dependence on the Hg:Te ratio are taken into account to understand this reduction.

HgTe grows stoichiometrically on A-polar facets, but the growth on the B-polar facets is completely suppressed with a material ratio of 250:1 to 350:1. If this ratio is chosen for the CdTe wires grown on a (110) substrate, the beam facing $(11\overline{2})$A surface has a much larger growth rate compared to those oriented towards the substrate. NWs overgrown mainly on one side only are shown in Fig. 5.2.

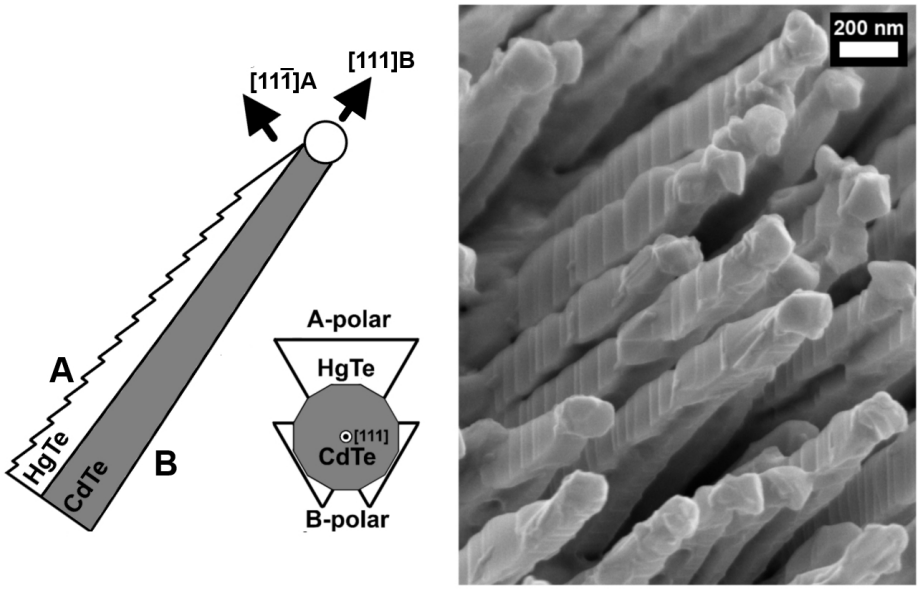

Figure 5.2: Cross-sectional schematic and SEM image of HgTe-NWs grown on one side facet of CdTe NWs on a (110) substrate.

The suppression of growth on B-polar sides for increasing Hg-supply is surprising. Obviously, both species must reach the growing crystal to grow a compound and if not enough material is supplied, then no growth occurs. For very high Hg:Te ratios, the physisorbed layer may saturate with Hg, but Te is effectively not present directly at the crystal. This effect occurs for the B-polar side, as there the sticking probability for Hg is larger compared to the A-polar side.[49, 50] The microscopical model for growth on polar sides is sketched in Fig. 5.3.

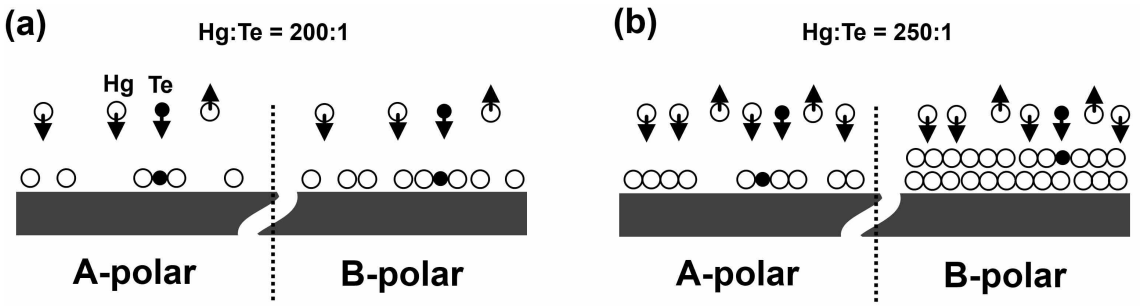

Figure 5.3: In (a), Hg (white) and Te (black) are physisorbed and HgTe growth occurs on all surfaces. The physisorbed layer saturates with Hg for the B-polar surface in (b), where Te atoms are incorporated only for the A-polar surface.

Knowing about the growth rate dependence on the Hg:Te ratio, the growth rate reduction on B-polar sides near the NW base can be explained. Due to the sample-source geometry, evaporated materials have to be multiply adsorbed and desorbed from the NW ensemble to reach the bases of long NWs. Thereby, Te is more likely incorporated and much less reflected by the NWs than Hg. Therefore, the effective Hg:Te ratio increases from the tops to the bases of the NWs, explaining the changing growth rate on B-polar facets in Fig. 5.1.

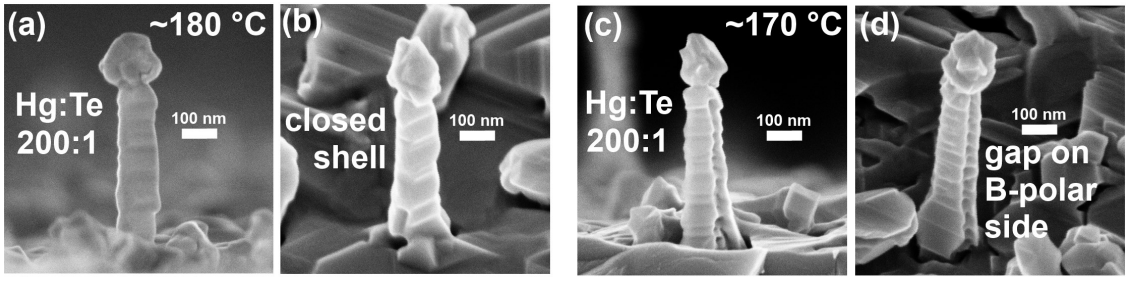

Figure 5.4: Due to the temperature dependent sticking probability of Hg, a temperature decrease from 180 ° in (a) and (b) to 170 ° in (c) and (d) can suppress growth on B-polar sides.

Since the sticking probability of Hg strongly depends on the temperature, changes in substrate temperature can have the same effect as changing the supplied Hg:Te ratio. For lower temperatures, the growth on B-polar sides is suppressed, similar to the case of an increased Hg:Te ratio. The growth temperature dependent shape of the HgTe-shells for fixed material ratio is shown in Fig. 5.4.

The steps observable in SEM images are a consequence of a subsequent step-flow growth mode sketched in Fig. 5.5. The $\{11\bar{2}\}$A NW sides are formed by $\{11\bar{1}\}$A steps. The probability for nuclei is highest at step edges. Nucleation is a statistical event and occurs delayed on adjacent steps. With proceeding nucleation, the step edge is moving. If nucleation occurs subsequently on adjacent steps, then step bunching leads to larger steps.

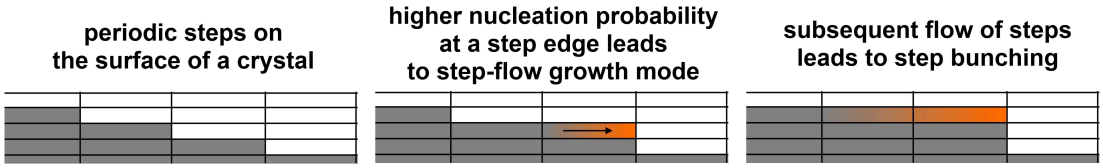

Figure 5.5: The subsequent nucleation at step edges leads to step bunching.

The achieved HgTe-heterostructure NWs are crystalline and exhibit a typical faceted geometry. Thus, the shape of the HgTe-based NW heterostructures is a result of the crystal structure of the cores. The two vertically oriented NWs in the front of Fig. 5.1 are rotational twins to each other. The underlying lattice is zinc blende and a rotation around [111] of 60° or equally 180° can be attributed to a rotational twin. Since the azimuthal orientation of the cross-section does not change along each individual wire, no further twinning occurs. Consequently, the origin of the twinning is at the interface to the substrate. The interface to the substrate, as well as the crystal structure of our core-shell NWs, are studied intensively in the next part. The different heterostructure geometries obtained in this work allow for an electrical characterization of quasi-one-dimensional HgTe. Charge transport experiments at the end of this thesis confirm that the HgTe-shelled NWs are conductive.

Part II

Crystallography

6 Nanowire crystal twins

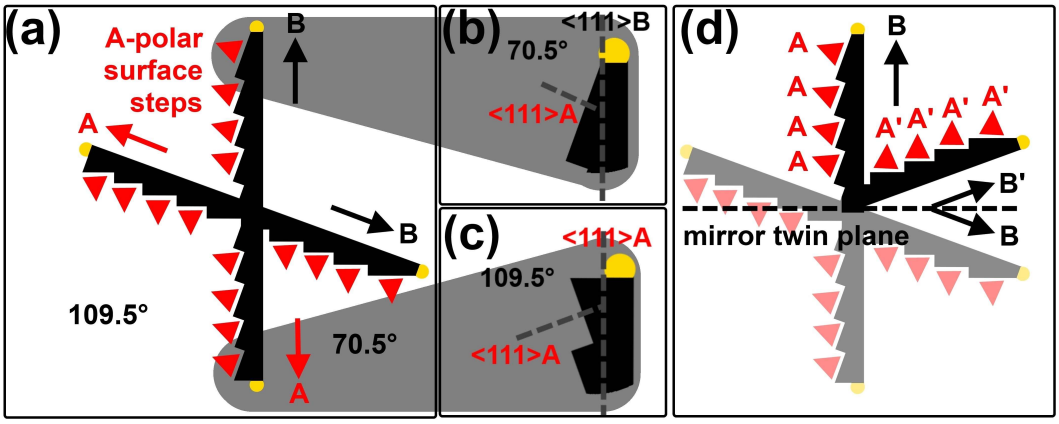

Figure 6.1: The A-polar step configuration (red arrowheads) for single-crystalline core-shell NWs growing along equivalent <111> A and B in the [1$\bar{1}$0] zone axis is depicted schematically in (a). To emphasize the difference, a detail for a B-polar growth direction is shown in (b) together with the theoretical configuration for a NW grown along an A-polar direction in (c). The twin growing along B' with A'-steps in (d) requires an additional symmetry operation with respect to a zinc blende single crystal.

In the previous part, characteristic heterostructure shapes are reported by tuning the Hg:Te beam pressure ratio. This observation is related to different growth rates on facets of opposite polarity. The morphology of the heterostructures is given by low indexed crystalline facets. By comparing the flux ratio dependent results with growth rates observed for layers with known polarity, it is possible to draw conclusions on the inner structure and polarity of individual NWs. The characteristic faceted surface reflects the high crystalline quality of the samples grown with the novel method. We know that the HgTe shell has a stepped shape for overgrown A-polar sides, while B-polar sides do not show steps in SEM images (see Fig. 5.1).

Assuming single-crystalline growth for the whole NW ensemble, the relative orientation of equivalent <111> directions in [1$\bar{1}$0] zone axis is shown in Fig. 6.1 (a). Some of the CdTe NWs on GaAs substrates grow along <111>A directions of the

substrate. They show steps like those growing along B-polar directions sketched in Fig. 6.1 (b). The steps have the same angle to the growth direction. Theoretically, the surface normal of the HgTe steps in Fig. 6.1 (c) should be inclined by 109.5° to the growth direction for wires growing along <111>A and not by 70.5° as for wires growing along <111>B in Fig. 6.1 (b). Thus, the single-crystalline picture does not hold for the whole NW ensemble. Instead, NWs grow along <111>A substrate orientation with <111>B growth direction according to their inner polarity. Figure 6.1 (d) sketches a possible twin, explaining the observation with an additional mirror operation. A polarity inversion equal to a mirror operation with respect to {111} is not known for the growth of zinc blende crystals. Figure 6.2 shows, that the mirror twin has a high probability on (111) substrates, where substrate surface and mirror plane are parallel.

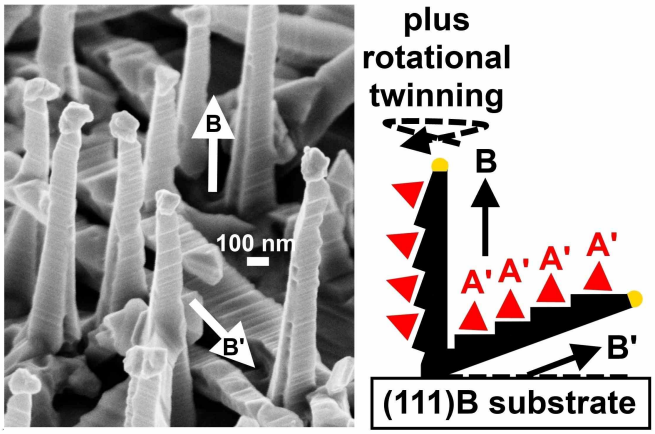

Figure 6.2: The mirror twin occurs often on (111) substrates. In this case the mirror plane (dashed line) and substrate surface are parallel.

In the following, the substrate/wire interface is studied to understand the twinning and polarity inversion with respect to the substrate. The interface is determined at the very beginning of growth. During the first seconds, the liquid Au-Ga droplets contain neither Zn nor Cd. Solely Ga from the saturated droplets can react chemically with the supplied Te. The SEM image in Fig. 6.3 shows, that growth starts with flat crystallites of hexagonal shape. The typical three-dimensional growth of ZnTe on GaAs takes over after some time. The amount of material growing as flat crystallites with this method is too low for further characterization. In order to grow enough material for analysis, we expose liquid Ga droplets on a (111)B GaAs substrate at 400 °C to a Te flux. To simulate the initial stage on a longer time scale, neither Zn nor Cd are supplied. The obtained sample is analyzed by X-ray diffraction in the following.

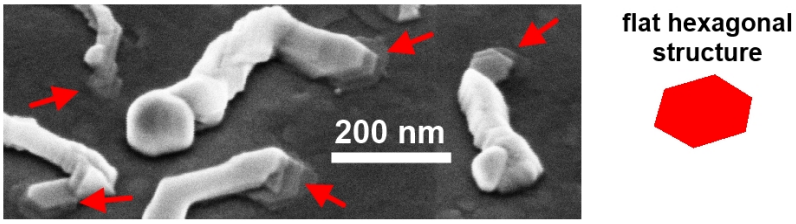

Figure 6.3: The image shows an early stage of growth, seeded by remote Au-Ga droplets exposed to simultaneous fluxes of Te and Zn. Before three-dimensional ZnTe growth takes over, flat hexagonal structures appear.

X-ray diffraction is the interference of monochromatic waves scattered from periodic structures. Bragg's law,

$$d \cdot \sin(\theta) = \frac{n\lambda}{2} \text{ (with } n \in \mathbb{N}\text{)}, \tag{6.1}$$

connects wavelength λ and the distance d of periodic scattering planes with θ, the angle between incoming beam and probed plane. For constructive interference of a known wavelength, the angle 2θ between incoming beam and detector is a measure for the distance of lattice planes tilted by θ to the incoming X-ray beam. In Fig. 6.4 (a) we find a reflection peak fitting to the vertical lattice constant $d = 1.6\,\text{nm}$ of the hexagonal layered phase of GaTe depicted in (b).[52]

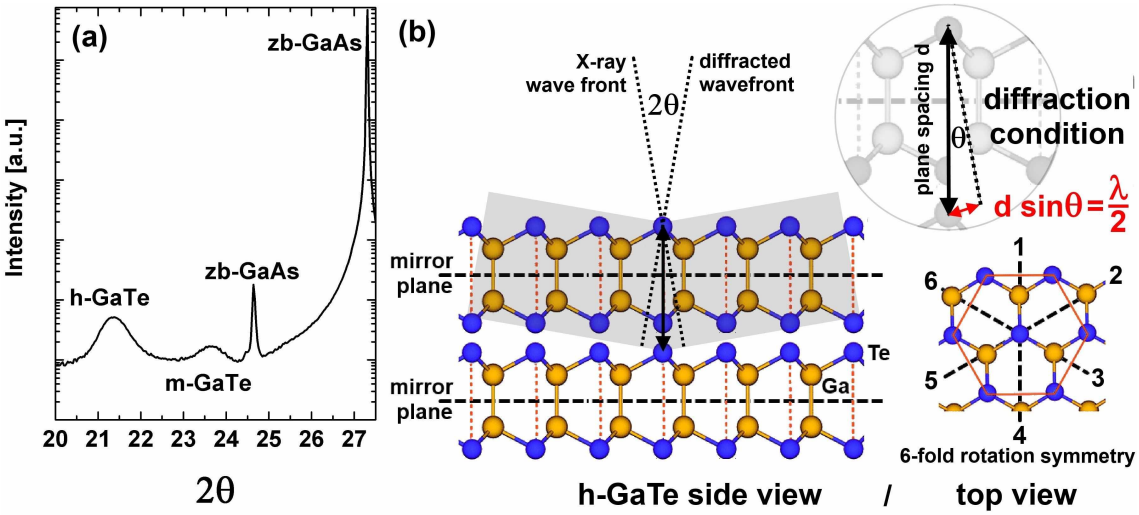

Figure 6.4: (a) 2θ-θ-scan of formerly liquid Ga on GaAs, which was exposed to Te. The sharp peaks are 111 reflections of the substrate for different wavelengths. The peak indexed by h-GaTe is the 001 reflection of the structure shown in (b). The monoclinic form (m-GaTe) is not stable.

The number of equivalent directions on the van-der-Waals surface is increased by additional rotational and mirror symmetries compared to the zinc blende surface of the GaAs substrate. The rotation by 60° around the growth axis as well as the mirror operation in growth direction are observed for our NWs, but which are not allowed for zinc blende single crystals. Having the same symmetries as zinc blende, plus the defined number of additional symmetry operations, the individual NWs can be viewed as crystal twins. The twins have the symmetry of the saturated surface of the hexagonal van-der-Waals crystal GaTe.[53] Thus, the twinning for the NWs growing along A-polar substrate directions can be explained, assuming crystallization from the Au-Ga droplets starts with a few monolayers of h-GaTe.

We know that the mirror twin has a high possibility on (111) substrates. Nucleation of GaTe on this surface allows for the mirror twinning. On (110) substrates, {111} planes are formed by roughening, but the overall surface orientation is different. Therefore, the mirror twin is observed less often, as can be seen from Fig. 6.5. The twins discussed so far are described by an additional symmetry operation acting on the whole NW. Thus, each NW can be treated as a single crystal. Twinning inside an individual wire is also observed some times and a topic of Chapter 9.

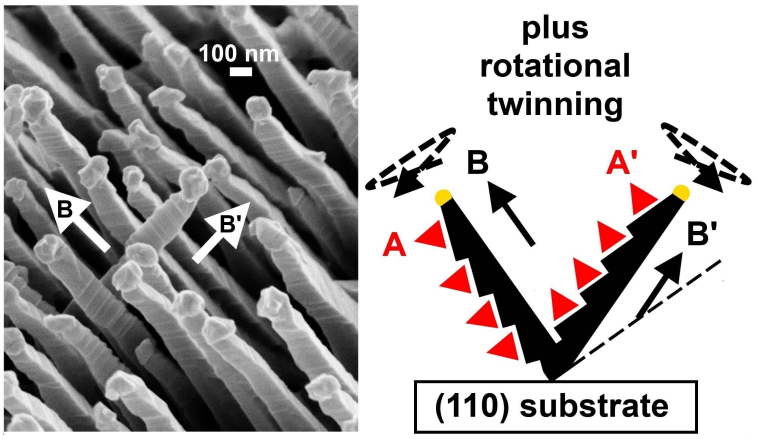

Figure 6.5: The probability for a mirror twin is much lower on (110) substrates, but it can be observed.

The morphology of the overgrown NWs changes with the Hg:Te flux ratio. Characteristic cross-sectional shapes related to the inner structure of the NWs allow for comparing the crystallographic orientation of individual NWs with SEM. This already indicates single crystallinity, making these NWs promising candidates for a detailed crystallographic analysis. We investigate the reciprocal lattice, which is introduced in the next chapter.

7 Introduction to the k-space

The simple example in the last chapter shows, that X-ray diffraction is a useful tool for the characterization of layered materials. This chapter explains the reciprocal lattice of a crystal and how it can be probed by diffraction. A crystal is a three-dimensional lattice of atoms with distinct symmetries. Cutting it along an arbitrary plane results in a two-dimensional array of atoms in the outermost plane. The bulk crystal below can be described as a periodic stack of equivalent planes shifted relatively to each other. As diffraction can be used to measure the distance between periodic planes of scatterers, symmetries in a crystal can be analyzed by waves. The planes are labeled by the Miller indices (hkl).[54] The diffracted intensity strongly depends on the density of atoms in the probed plane. Only low indexed planes can be probed experimentally, as they have a high density of atoms scattering the incoming wave. The phase relation of waves, scattered at the atomic positions in each unit cell, defines the intensity of different reflections.[55, 56] For a zinc blende crystal, reflections hkl with all indices being even or odd at the same time can be observed. We therefore are able to measure the distance of lattice planes for high symmetry directions of the crystal by diffraction. The reflections are at shifted positions when the unit cell is deformed by strain. In the following, a crystal is considered as a layered structure with a certain period along the probed direction. To analyze a three-dimensional distribution of planes we use the k-space. Each plane (hkl) with a distance d_{hkl} to the next equivalent plane is represented by a vector series $\vec{K}_{hkl}$ in k-space.

$$|\vec{K}_{hkl}| = \frac{n}{d_{hkl}}, \text{ with } \vec{K}_{hkl} \mid\mid \begin{pmatrix} h \\ k \\ l \end{pmatrix} \text{ (and } n \in \mathbb{N}). \tag{7.1}$$

For an undistorted zinc blende crystal with a cubic lattice constant a, one can calculate the theoretical spacing d_{hkl} by

$$d_{hkl} = \sqrt{\frac{a^2}{h^2 + k^2 + l^2}}. \tag{7.2}$$

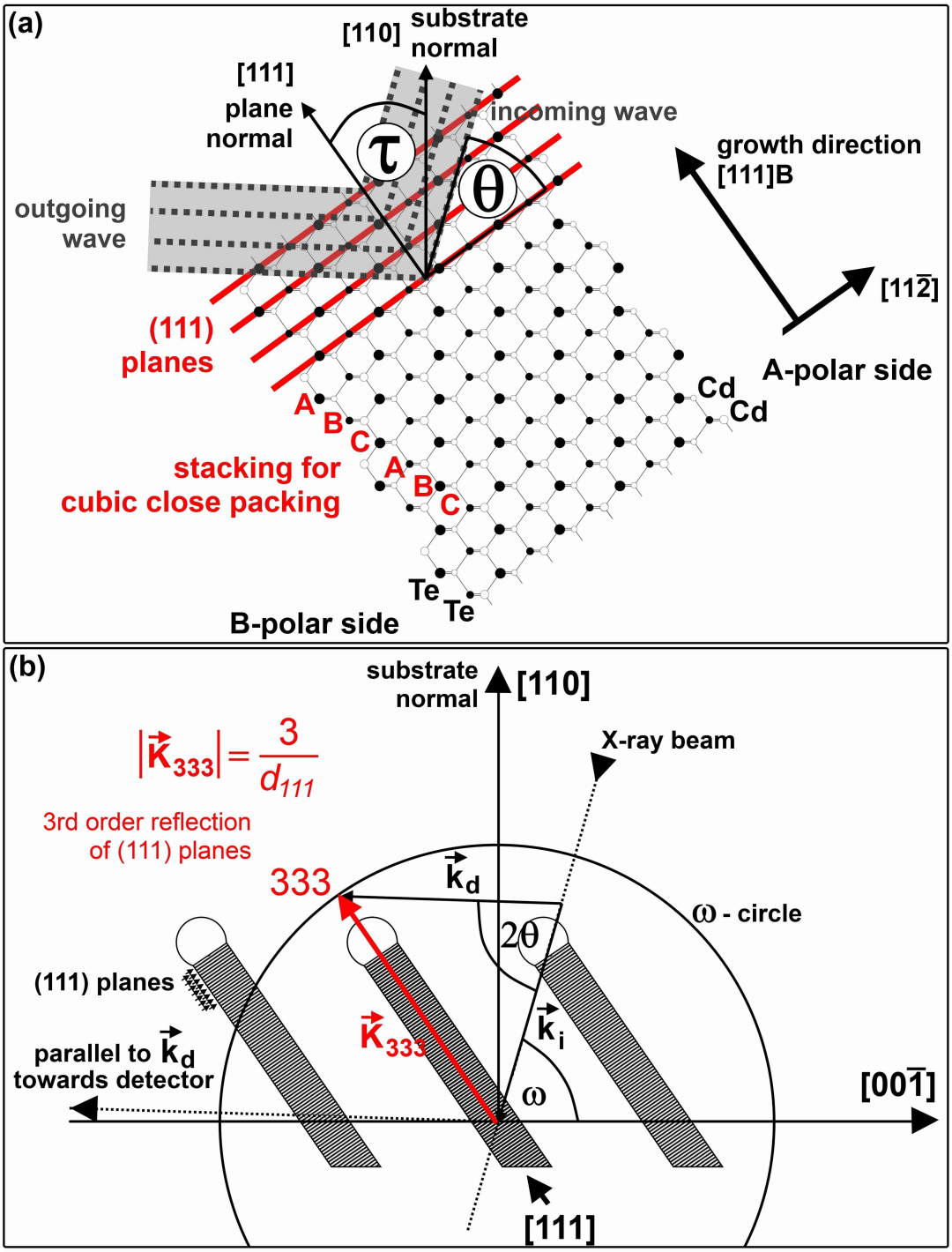

Figure 7.1: (a) Bragg-condition for 333 drawn in the [1$\bar{1}$0] zone axis of zinc blende CdTe NWs growing along [111]B on a (110) substrate. (b) Ewald-construction for 333 in k-space together with wires and (111) planes in real space.

An Ewald-construction connects measurement geometry and reciprocal space with reflections at $\vec{K}_{hkl}$.[59] For monochromatic waves, the incoming beam is represented by $\vec{k}_i$ with $|\vec{k}_i| = 1/\lambda$.[1] The diffracted wave $\vec{k}_d$ is measured at an angle of 2θ to the incoming beam. If $\vec{k}_d - \vec{k}_i = \vec{K}_{hkl}$, we measure the length

$$|\vec{K}_{hkl}| = \frac{2}{\lambda} \cdot \sin\frac{\theta}{2}. \tag{7.3}$$

$\vec{K}_{hkl}$ is called the scattering vector of the corresponding planes. As shown in the last chapter, X-ray diffraction is one way to probe periodic planes. To give an example, the relation of (111) planes to their third order reflection is sketched in Fig. 7.1 (a). The method averages over macroscopic sample areas. If the lattice of most of the NWs is identical and furthermore oriented the same, then the interference pattern is equal to the pattern of a single crystal. Thus, a high ensemble uniformity is needed to allow for detailed analysis. Twinning can be neglected on (110) substrates and overgrowth occurs mainly on one side of the NWs, making such samples ideal candidates for X-ray diffraction. Since the direction of strain in mismatched heterostructures is determined by the orientation of the hetero-interface, multiple interfaces, as for NW cores with a closed shell or for randomly oriented NWs, would smear out the diffracted intensity of differently strained regions.

The lattice of zinc blende CdTe ($a_{CdTe} = 6.4825\,\text{nm}$)[57, 58] and the wavelength $\lambda_{Cu,k_{\alpha 1}} = 0.154056\,\text{nm}$ is used to derive the Ewald-construction for 333 in Fig. 7.1 (b).

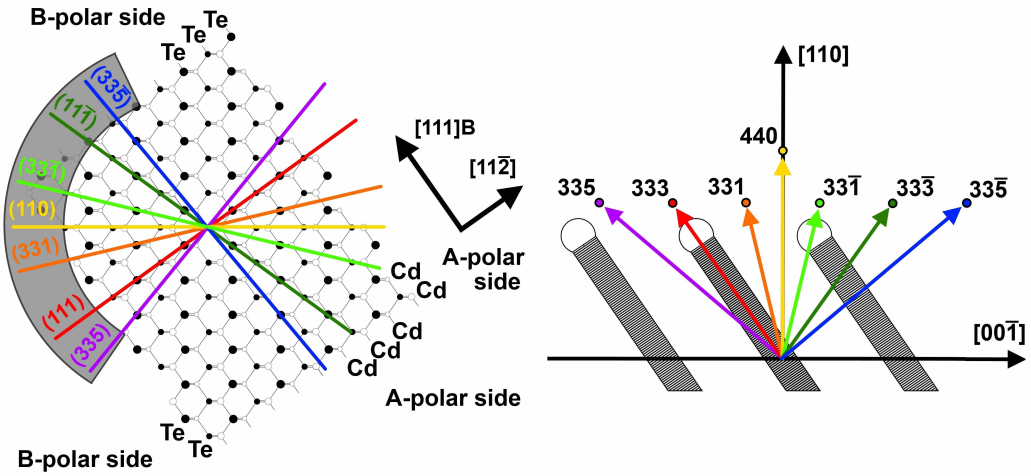

Figure 7.2: The differently oriented planes (left) are represented by vectors in k-space (right).

[1] The reciprocal space is normalized by 2π in this work.

We use high-resolution X-ray diffraction (HRXRD) to verify the plane spacing in the crystal structure of our NWs with an accuracy of 0.01%. To measure a certain reflection, it must be aligned in the plane of X-ray tube and detector. Changing ω by rotating the sample in front of the tube, the reciprocal space is scanned along a circle around the origin. Therefore, different ω probe differently oriented planes. When $\omega = \theta \pm \tau$, then reflections of planes tilted by τ to the substrate surface can be measured. To scan perpendicular to the ω-circle, the detector rotates with twice the angular speed around the sample as the sample rotates in front of the tube, called 2θ-ω scan, which probes different lengths $|\vec{K}_{hkl}|$. Comparing theoretically and experimentally derived spacings for different planes in Fig. 7.2 reveals strain in the lattice. The detailed analysis is done in chapters 10 and 11.

Not only X-rays, but also electrons can be used for diffraction. High-energy electrons have a smaller wavelength compared to the used X-rays, allowing for an easy forward geometry shown in Fig. 7.3.

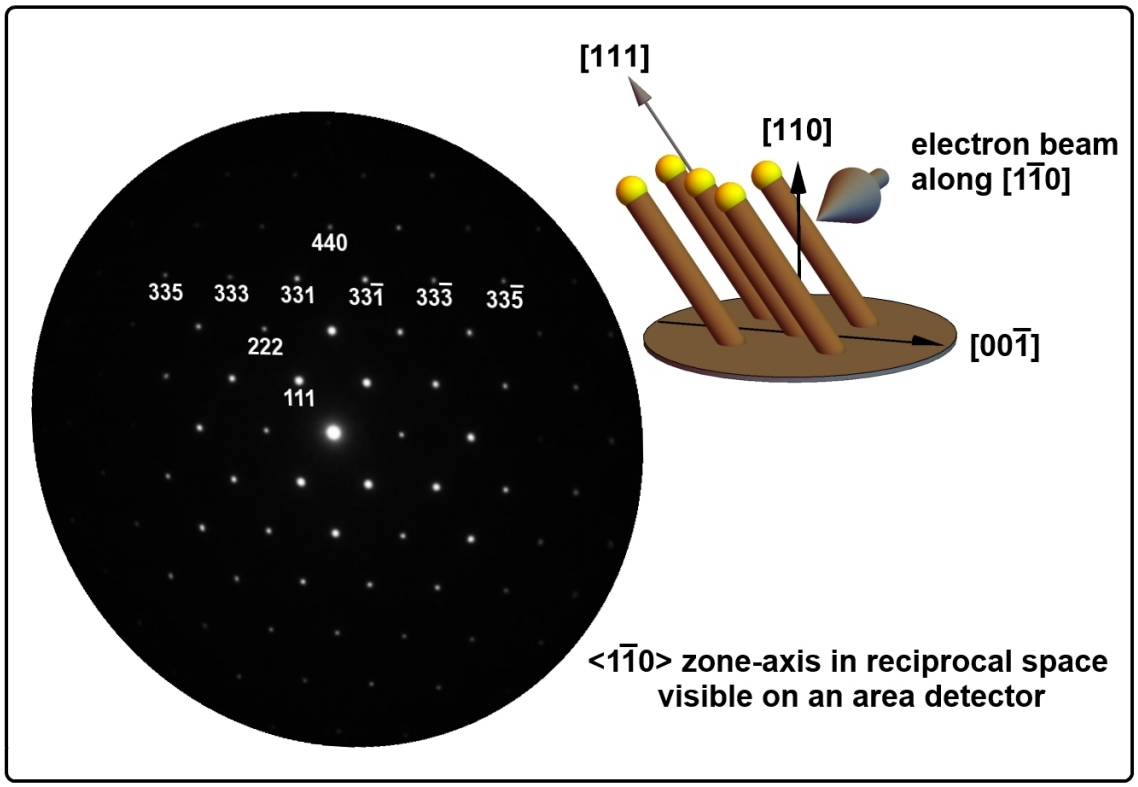

Figure 7.3: Electron diffraction inside a microscope allows to record a reciprocal space sheet of individual NWs on an area detector in one shot.

As these electrons are coherent perpendicular to their direction of propagation, only planes parallel to the beam, meaning $\vec{K}_{hkl} \perp \vec{k}_i$, are probed. Therefore, electron diffraction probes a sheet in k-space, when a crystal is placed between an electron-gun and a detector screen. The penetration depth of electrons is small. Thus, the size of the probed structures needs to be in the range of nm. Using the electron beam of a microscope, as depicted in Fig. 7.3, the reciprocal image of an individual wire can be probed.

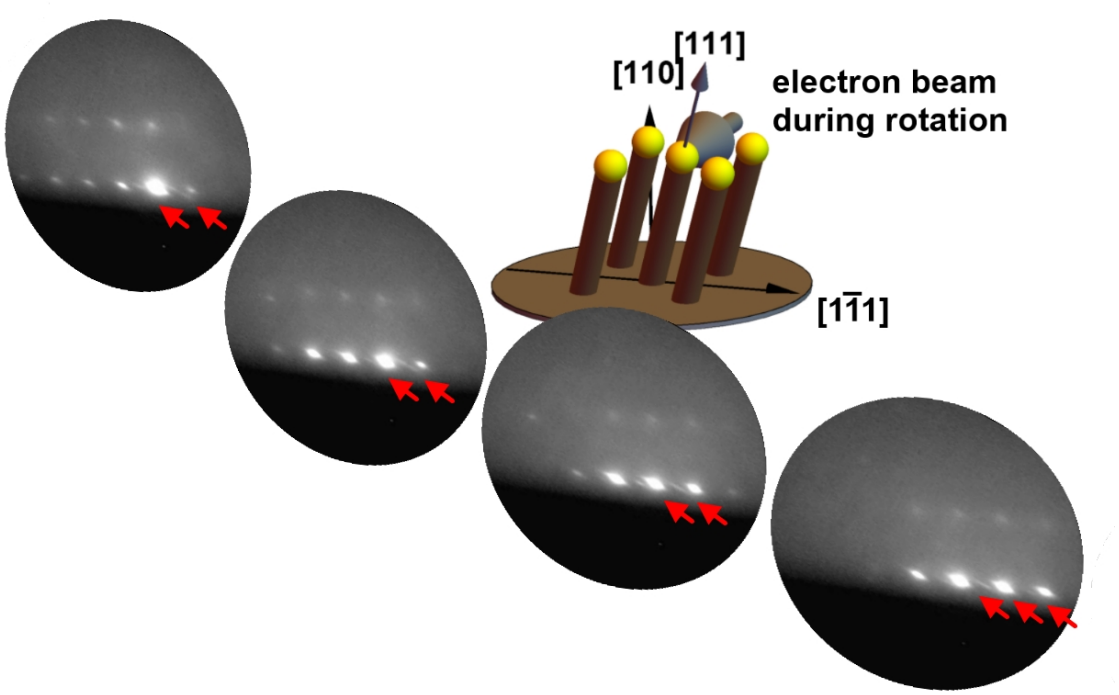

Figure 7.4: Diffraction from (1$\bar{1}$1) surface steps of many CdTe NWs growing along (111) on a (110) substrate causes the streaky features denoted by arrows.

The easy forward geometry furthermore allows to record electron diffraction during the growth process. Some parts of the screen are always shadowed by the sample holder. This method is performed in-situ. Hence, the surfaces of the growing NWs are not oxidized yet as they are for the sample investigated in the electron microscope. Stable, low indexed planes margin the NWs. The arrangement of atoms on the surface of a crystal has a certain symmetry and can also be described in k-space. If the electron beam fulfills the condition for total reflection on a certain surface, then the electrons do not penetrate the crystal. Instead they get reflected and diffracted by the periodic surface atoms at the same time. The three-dimensional

arrangement in the bulk is represented by spots in reciprocal space. A surface is two-dimensional, thereby it is represented by rods, lines or streaks in k-space pointing perpendicular to the surface. Due to surface reconstruction, the period of the surface can be different from the period in the bulk. Figure 7.4 shows examples of diffraction obtained during growth. As the NW sides probed here consist of regular steps,[60, 61] the reciprocal space of such an arrangement is explained below.

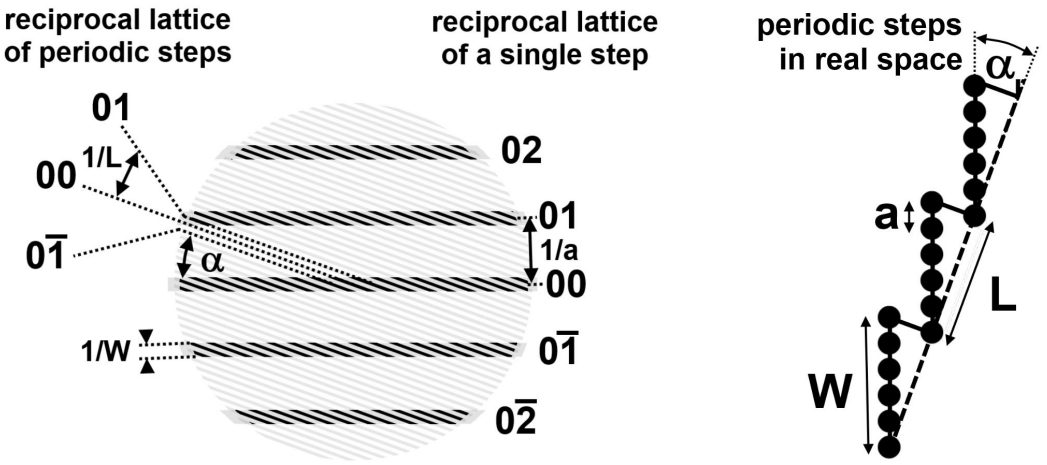

Figure 7.5: The reciprocal space of periodic steps forming the surface of a crystal contains information on the periodicity of the surface atoms.

The electron diffraction is helpful to optimize growth conditions, because the surface quality is directly affected by slightly detuned growth conditions. In the case of heteroepitaxy, the characterization of the surface overgrown subsequently is of fundamental interest, since the quality of the CdTe NW surface determines the quality of the HgTe shell. The results for the configuration of surface atoms on CdTe NWs are discussed in the next chapter.

8 Studies on CdTe nanowire facets

The narrow temperature limits required for uniform NW growth are controlled by changes in the electron diffraction recorded from time to time during the entire growth. The investigation of transmission diffraction patterns to study the catalyst's phase transition from solid to liquid and NW nucleation was reported earlier.[62] Here, not only the diffraction from transmission, but additionally streaks are observed, when the electron beam is diffracted during reflection at crystalline facets. High quality and uniformity of the NWs allow to study the atomic periodicity of the NW side-facets by RHEED.

Different low-index surface orientations are identified for CdTe NWs. During sample rotation, each surface is in the total reflection condition for a certain azimuth and one can study the periodicity of each NW side-facet only for a given azimuthal direction. Twelve CdTe NW sides are identified by comparing the symmetries of RHEED obtained during rotation of different substrate orientations. These are the surfaces orientations $\{1\bar{1}0\}$ and $\{11\bar{2}\}$ parallel to the NW growth axis [111]B. The RHEED signal is analyzed on (111)B and (110) substrates, where the [111]B wire orientation dominates.

First, we explain the RHEED pattern of NWs grown vertically on a (111)B substrate. With this geometry, one can see two alternating diffraction patterns every 30° shown in Fig. 8.1 and 8.2. The interference pattern obtained by an electron beam along $[11\bar{2}]$ as well as its schematical illustration are shown in Fig. 8.1. The distance of periodic features in the interference pattern is proportional to the inverse lattice constant. The region of the NWs, which can be penetrated by the electron beam, causes an interference with broadened spots. The period of the spots is a measure for the bulk lattice constant verified with higher precision by high-resolution X-ray diffraction (HRXRD) in the next chapter. The electron beam pointing along $[11\bar{2}]$ is reflected from $(\bar{1}10)$ facets. As a result, lines perpendicular to this surface emerge on the RHEED screen. One of these lines is denoted by an arrow in reciprocal space shown left-hand side in Fig. 8.1. Here, the lines show the same periodicity parallel to the surface as the transmission spots. Therefore, the surface atoms show the same

period of 1.12 nm along the [111] direction as in the bulk. Taking into account the atomic positions of the zinc blende unit cell, the cross-sectional view of bulk and $(\bar{1}10)$ surface atoms is shown right-hand side in Fig. 8.1.

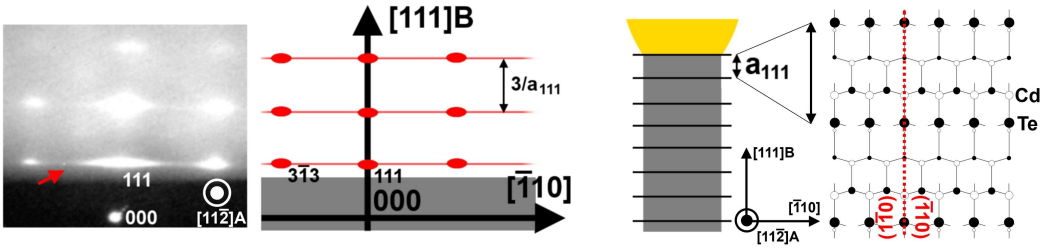

Figure 8.1: RHEED screen, reciprocal space schematic and corresponding real space cross-section looking along $[\bar{1}\bar{1}2]$ for a (111)B substrate.

The RHEED pattern obtained by an electron beam along $[1\bar{1}0]$ as well as its schematical illustration are shown in Fig. 8.2. The zinc blende single crystal has a threefold rotational symmetry with respect to the [111] axis. Therefore, the diffraction pattern of a single crystal would not be symmetric to the [111] axis for an electron beam along $[1\bar{1}0]$. The observed rotation symmetry for the [111] axis is caused by 60° (or equally 180°) rotational twinning at the bases of the NWs. The electron beam pointing along $[1\bar{1}0]$ is deflected during reflection from $(11\bar{2})$ facets. The $(11\bar{2})$ facets show a more complex pattern compared to the atomically flat $(\bar{1}10)$ facets.

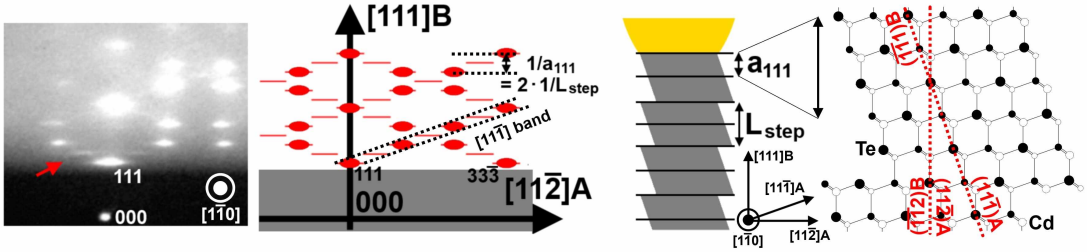

Figure 8.2: RHEED screen, reciprocal space schematic and corresponding real space cross-section looking along $[\bar{1}10]$ for a (111)B substrate.

Instead of continuous lines, small vertically staggered stripes are visible in Fig. 8.2, being perpendicular to the $(11\bar{2})$ surface. The stripes are located within bands parallel to the $[11\bar{1}]$ direction. Half of the stripes are located in the middle between two diffraction spots. One of them is pointed out by an arrow in the diffraction

pattern of Fig. 8.2. The position of every second stripe along the $[11\bar{1}]$ band is identical to the position of the transmission spots. This interference pattern originates from a regularly stepped surface consisting of $(11\bar{1})$ nanofacets.[60] The step length $L_{\mathrm{step}} = 2.24\,\mathrm{nm}$ along [111] is twice the bulk lattice constant $a_{[111]}$. The deduced cross-sectional view of the atomic positions within the NW and on its $(11\bar{2})$ surface is shown right-hand side in Fig. 8.2.

A similar diffraction pattern is obtained for NWs on (110) substrates. One of the characteristic staggered stripes is visible right-hand side in Fig. 8.3 at the center of the lowermost diffraction spots. Less twinning as on (111) substrates results in no [111]-axis symmetry in the RHEED.

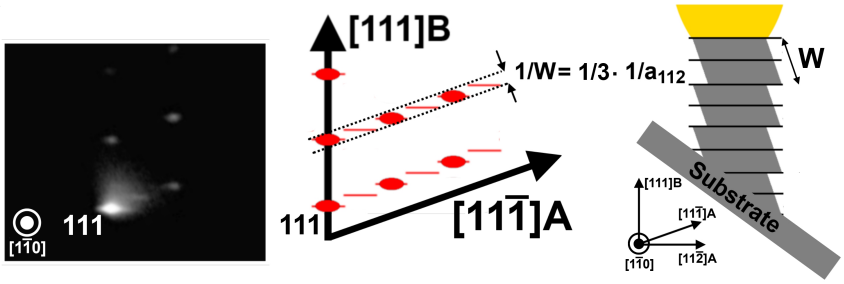

Figure 8.3: RHEED screen, reciprocal space schematic and corresponding real space cross-section looking along $[\bar{1}10]$ at growth start for a (110) substrate.

On (110) substrates, the CdTe NWs grow tilted by 35° to the substrate normal. Exposed to a higher material flux per unit area than any other NW side, radial overgrowth is enhanced on the $(11\bar{2})$A side. If the temperature is set relatively high, then axial growth slows down. A pyramidal NW morphology appears, when the axial VLS growth rate equals the very slow growth on the sides. The pyramidal shape is associated with an increased step width W, so the bands in k-space shrink.

If the step width is large compared to the electron coherence length, then RHEED does no longer probe the step periodicity. The staggered stripes finally become continuous lines. One of these lines is marked by an arrow in Fig. 8.4. This interference pattern reflects the periodicity of the surface atoms on the $(11\bar{1})$A nanofacets. The $<11\bar{1}>$ lines show half the spacing of the spots along the [112] direction. We draw the conclusion, that the nanofacets show a reconstruction with doubled period along [112]. This observation is in agreement with the (2x2) reconstruction previously described by Egan *et al.* for a CdTe $(11\bar{1})$A layer.[63]

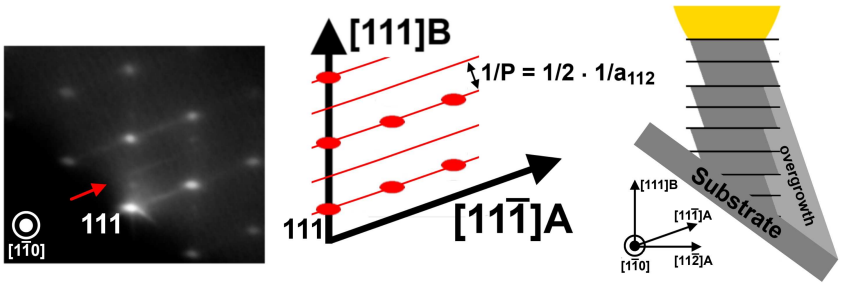

Figure 8.4: RHEED screen, reciprocal space schematic and corresponding real space cross-section looking along [$\bar{1}$10] after radial overgrowth.

By combining the observation of a doubled period for both the step length and the surface atoms on the steps with the findings of Egan *et al.* for the arrangement of (11$\bar{1}$)A surface atoms, the stepped reconstruction can be understood by a model discussed in the following. The (2x2) reconstructed (11$\bar{1}$)A surface is stabilized by Cd-vacancies, in order to fulfill the electron counting rule assuming occupied Te and unoccupied Cd bonds. Every second Cd atom is missing in every second row of lattice positions parallel to [1$\bar{1}$0].[63] In total, every fourth Cd surface atom is missing. Applying this reconstruction to the (11$\bar{1}$)A steps forming the (11$\bar{2}$)A NW surface, the step edges along [1$\bar{1}$0] distort the reconstructed vacancy structure. If not just every second, but all of the Cd edge atoms are missing, then the edge is formed by occupied bonds of Te and electron counting rule is fulfilled. The cross-sectional view of the reconstruction considered on stepped NW surfaces is shown in Fig. 8.5.

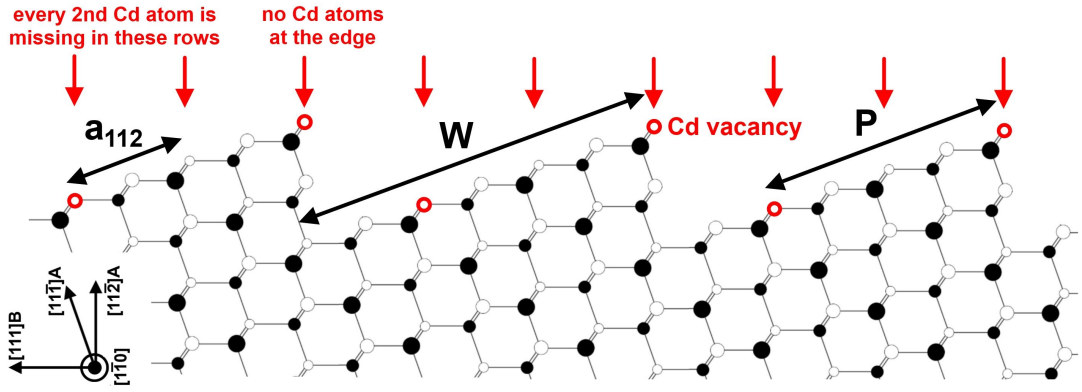

Figure 8.5: The step width W is stabilized by a Cd-vacancy surface reconstruction.

This model is convincing, because we would not expect to get Cd edge atoms connected to the crystal with only two bonds. These would be easy to break and therefore Cd edge atoms desorb at the VLS growth temperature. The step edge, consisting of occupied Te bonds, is effectively charged and additionally attracted by neighboring Cd surface atoms with unoccupied bonds. This coulomb potential increases the stability of the considered configuration. Steps with a length equal to the lattice constant $a_{[111]}$ are too small to host a (2x2) reconstruction. The observed step length, equal to twice $a_{[111]}$, leads to the smallest surface area for the $(11\overline{2})$A surface with steps formed by (2x2) reconstructed $(11\overline{1})$A nanofacets and edges with occupied Te bonds. The observed step length is therefore energetically favorable. The possibility to draw such a detailed picture of the surface atom arrangement by RHEED proves the high crystalline quality and uniformity of the NWs.

On (001) substrates, the NWs grow along two equal directions [111]B and $[\overline{11}1]$B. Furthermore, other growth directions corresponding to high-index substrate orientations are found on (001) substrates. These directions result from three-dimensional multiple-order twinning during nucleation and were described already for GaAs NWs by E. Uccelli *et al.*[64] The diffraction pattern of a NW facet for one growth direction is then superimposed with others and hard to analyze.

With optimized growth parameters, a periodic diffraction pattern on (111)B and (110) substrates allows for the detailed analysis of atomic arrangement on the surfaces and in the bulk. Our ability to do so is reflecting the high crystal quality and ensemble uniformity of our CdTe NWs. The high quality of the cores allows to grow epitaxial HgTe shells. From the electron diffraction, we draw the conclusion, that advanced methods with higher resolution can be used to further characterize the crystallites. More precise methods and the experimental outcome are discussed in the next chapters.

9 CdTe-HgTe nanowire crystal structure

Now we show real space images with atomic resolution, together with the corresponding k-space image, recorded for the same CdTe NW to underline the equivalence of both descriptions. Transmission electron microscopy (TEM) probes the crystal structure with spatial resolution. We are using a "FEI Titan 80-300 (S)TEM" operated at 300 kV. The cross-sectional TEM specimens were prepared in two steps. First, the sample was covered with PMMA and Pt to improve the handling and then thinned down to a thickness of ∼100 nm by focused ion beam milling using an "FEI Helios Nanolab Dual Beam" system. We used a 30 kV Ga^+ ion beam with currents between 0.28 nA and 28 pA. A final low-kV cleaning was performed with a 2 kV Ga^+ ion beam and an incident angle of 1°. High-angle annular dark-field scanning transmission electron microscopy (HAADF-STEM) images are recorded along $[\bar{1}10]$ zone axis with an electron energy of 300 keV.

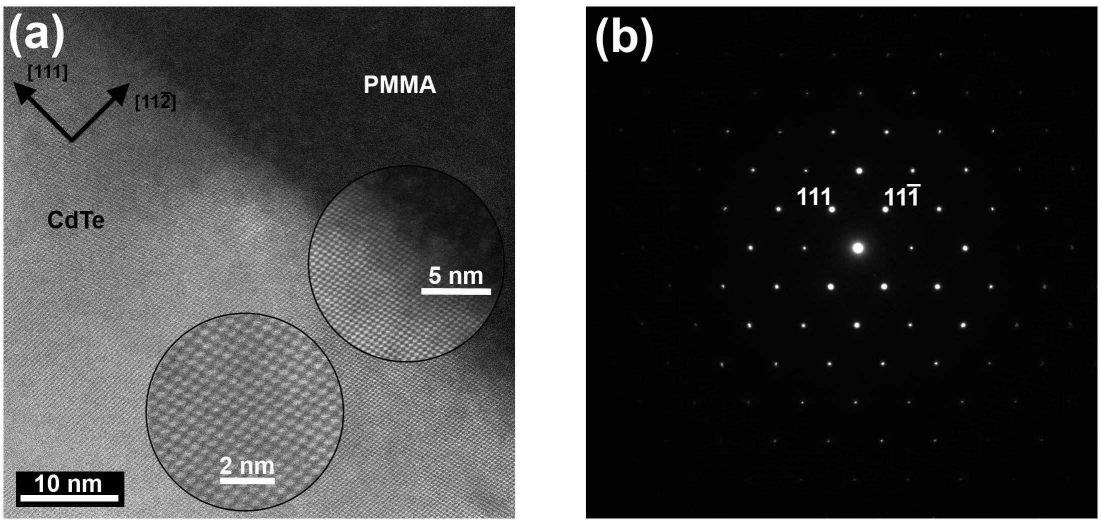

Figure 9.1: (a) is a STEM image of a CdTe NW along $[1\bar{1}0]$ zone axis and (b) the corresponding electron diffraction pattern.[65]

We analyze the STEM images for CdTe NWs growing along the [111] direction of a (110) GaAs substrate. Figure 9.1 (a) shows the $[1\bar{1}0]$ zone axis STEM images with different magnifications. The NW is single-crystalline and stacking fault free over the entire length. We therefore conclude to have found ideal growth conditions. Bright spots on STEM images correspond to the position of the Cd and Te atoms. Since the atomic numbers of these elements are very close, 48 and 52, respectively, they can not be distinguished in the images. Figure 9.1 (b) shows the corresponding electron diffraction pattern which can be indexed in a cubic lattice, space group $F\bar{4}3m$, with an unit cell parameter $a = 0.648$ nm. This symmetry and lattice constant is expected for the zinc blende CdTe we were aiming at. Thus, we can analyze the crystal structure either in real space, or by diffraction in reciprocal space.

The high quality and uniformity of the axial ZnTe-CdTe NWs on a GaAs substrate is reported for the first time. For II-VI NWs realized with a similar method by others, a high density of stacking faults is observed.[34] To analyze the CdTe crystal structure in detail, we use an integrative X-ray diffraction technique with higher resolution in k-space. The dense NWs shown in Fig. 9.2 (a) show reflections in X-ray diffraction and we are able to resolve the influence of the ZnTe growth start. The reflections discussed in the next chapter are verified to be caused by the NWs, since they gradually vanish for samples with lower NW density.

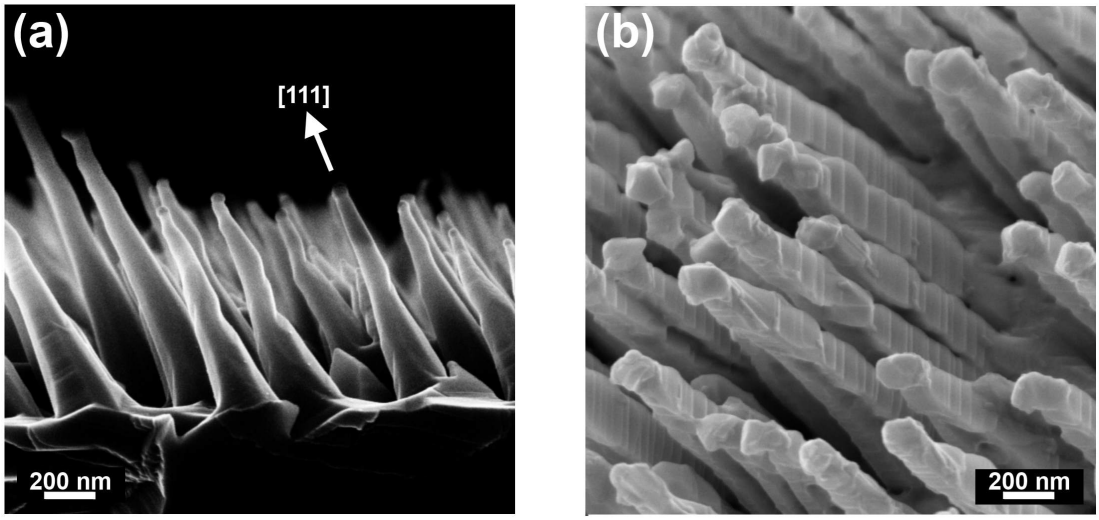

Figure 9.2: The SEM image in (a) shows bare CdTe NWs on GaAs (110) and (b) depicts a part of the same sample overgrown with HgTe.

The CdTe NW ensemble has uniform, free-standing wires, which are suitable for overgrowth. A part of the sample in Fig. 9.2 (a) is overgrown with HgTe and shown in (b). The STEM image in Fig. 9.3 (a) reveals, that HgTe overgrowth occurs pre-

dominantly on the $(11\overline{2})$A facet of the CdTe NWs. This is a result of sample-source geometry inside the growth chamber and different growth rates on facets with opposite polarity. HgTe develops a stepped surface structure visible in the STEM and SEM images. The stepped surface consists of flat $(11\overline{1})$A facets and is a consequence of a step-flow growth mode for HgTe on the stepped $(11\overline{2})$A CdTe side-facet, which was discussed in the previous chapter. The high resolution STEM image in Fig. 9.3 (b) shows the HgTe zinc blende lattice along the $[1\overline{1}0]$ zone axis. We find, that the high CdTe crystal quality allows for the growth of epitaxial HgTe of comparable quality on each NW.

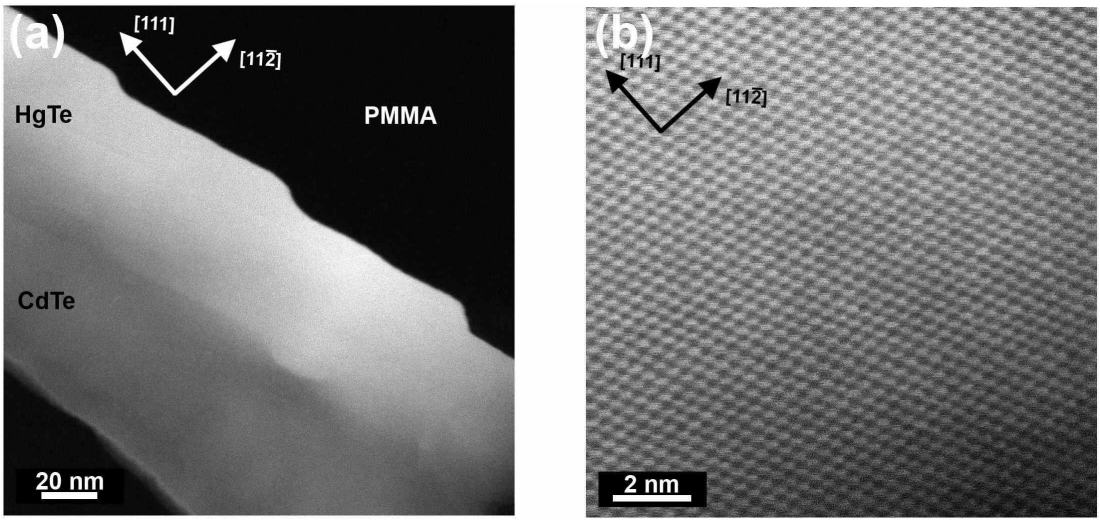

Figure 9.3: To give an overview, (a) shows the cross-section of HgTe grown on one side of a CdTe NW. The STEM image in (b) shows the crystal structure of the HgTe-shell with high resolution.[65]

Earlier attempts to grow HgTe-based NWs resulted in polycrystalline structures with inclusions of elemental Tellurium.[35, 36] There, neither a preferred growth direction was reported, nor a defined epitaxial hetero-interface to induce strain. In contrast, the advanced microscopical technique applied here, shows the desired zinc blende lattice over the entire heterostructure. The findings are a very promising base for the development of more complex multi-shell structures in the future. The CdTe-HgTe NWs achieved so far are already interesting for further experiments. The crystal structure should result in the formation of electronic bands, with distinct properties for charge transport in the bulk and at the interfaces.[37] Hence charge transport is carried by states described by the band structure, the heterostructures are characterized by charge transport experiments in the last part of this manuscript. The electronic band structure results from the HgTe lattice and can be calculated theoretically.[38]

The resolution of TEM is not good enough to reveal the effect of the mismatched lattices. The HgTe overgrown NWs depicted in Fig. 9.2 (b) show reflections in X-ray diffraction. The findings obtained by high-resolution X-ray diffraction are discussed in the next two chapters. In contrast to the integrative X-ray method, which averages over macroscopic sample areas, the microscopic method uses an focused electron beam and allows to analyze the crystal structure with spatial resolution. So, STEM images allow for analysis regarding grain boundaries in the NWs. Since overgrowth occurs on the $(11\bar{1})$A steps, rotational twinning of 60° (or equally 180°) around $[11\bar{1}]$ is a possible growth defect. This defect can be described as a local switching from cubic close packing to hexagonal close packing for one monolayer. Figure 9.4 (a) is a STEM image of a rotational twin lamella. The orientation of the crystal switches back to the original configuration after several atomic layers. The twin extends from the core to the outer surface of the HgTe shell. These twins alter the orientation of stable facets and thereby the shape of the heterostructures, denoted by a circle in Fig. 9.4 (b). The threefold rotation symmetry of the twin, being rotated by 180° compared to the usual steps, is sketched as a red triangle.

We see, that twins can be inferred from the shape of the HgTe-base NWs. Hence, we are able to choose twin-free NWs for charge transport experiments. Before we come back to devices for transport characterization, the influence of the lattice mismatch in the heterostructure NWs is analyzed in the next two chapters.

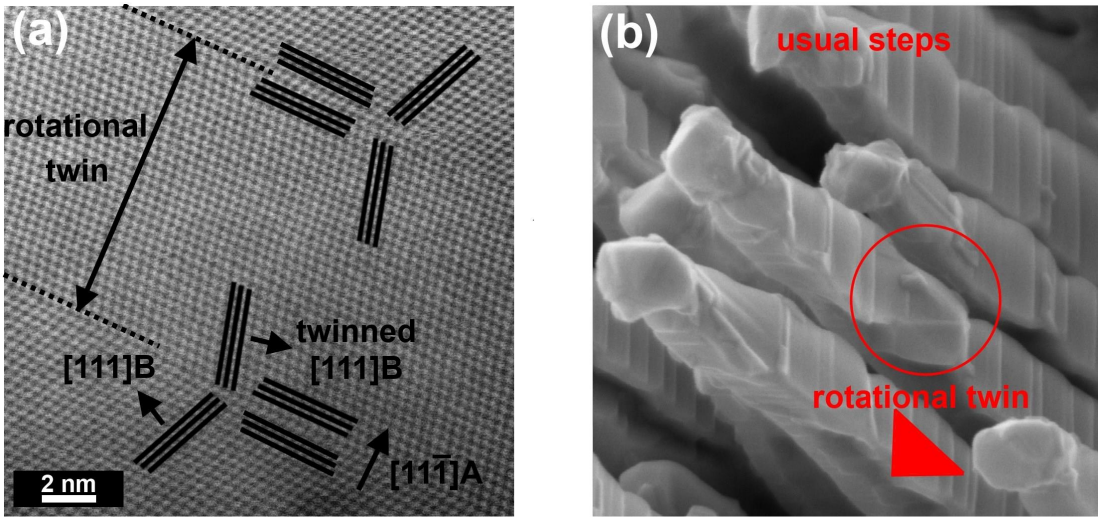

Figure 9.4: (a) STEM image of a rotational twin domain inside HgTe.[65] (b) The rotational twin alters the shape of the heterostructure locally.

10 Influence of ZnTe growth start

The investigated CdTe NWs grow on ZnTe stubs. They grow along [111]B crystallographic orientation on an (110) GaAs substrate, as we can see from electron micrographs. The influence of the ZnTe growth start on the crystal structure of the CdTe NWs was not discussed so far. The effects are small, so we need to put attention on the experimental setup to resolve the presence of Zn in the NW cores. High-resolution X-ray diffraction (HRXRD) probes the crystalline structure of an ensemble of NWs in reciprocal space. To analyze the relation between NW lattice and substrate, we align the sample inside the diffractometer. The substrate is glued to the specimen holder without additional stress by the use of a liquid In-Ga eutectic adhesion film. The diffraction from the GaAs wafer is used as a reference to verify the sample alignment. An accuracy of less than 0.01% relative error is achieved for the lattice constant derived from various reflections.

The "Bruker D8" diffractometer setup is the following: Cu-anode X-ray source (Cu kα_1), Goebel mirror, 0.6 mm slit, 2-bounce Ge022a monochromator, sample, solid-state-detector array "LynxEye". An effective aperture provides a high resolution along 2θ, the angle between X-ray beam and detector. In order to improve the signal-to-noise ratio, the effective aperture in ω-direction, the angle between X-ray beam and sample surface, is appropriately widened. A high resolution along 2θ is necessary to resolve the slightly different lattice constants of HgTe and CdTe and their relative changes as a consequence of residual strain. Due to the fact that NWs are small and free-standing structures, the reflections are broadened along ω and there is no need for a high resolution along this angle.

The effective aperture is formed by an integration technique using the detector array. During each scan, the intensity for a range of 91 different values of 2θ is recorded at the same time for each value of ω. Thereby, one scan covers an area in k-space, and not only a single line. All intensities recorded at different angles ω, but the same angle 2θ, are summed up to improve the signal-to-noise ratio. Thereby each area scan is reduced to a line scan with effectively widened aperture along ω. The resolution of the 1D detector strongly depends on the measurement geometry.

Asymmetric reflections need to be recorded in $\omega = \theta + \tau$ geometry to get a high beam compression. The compressed beam has a small width, allowing for the use of an opened detector array with no further physical aperture. In every case, the resolution is limited by the detector pixel size of 75 µm, equal to a resolution of 37 arcsec. Repeating the scan for different offsets $\Delta\omega$ between ω and 2θ covers an area in reciprocal space again. In this way, several reflections in the plane of the NWs' growth axis and substrate normal are investigated with reciprocal space maps (RSM). The lengths K_{hkl} for the recorded reflections are listed in Tab. 10.1.

hkl	angle to [111] [°]	K_{hkl} NW core [1/nm]	$\Delta\omega$ tilt towards [001] [°]	x $Cd_{1-x}Zn_xTe$ [%]
335	-14.4	10.1199 ± 0.0007	0.52 ± 0.06	0.7 ± 0.2
333	0.0	8.0194 ± 0.0009	0.56 ± 0.06	0.8 ± 0.2
331	22.0	6.7266 ± 0.0009	0.52 ± 0.06	0.6 ± 0.2
440	35.3	8.7275 ± 0.0008	0.52 ± 0.06	0.2 ± 0.2
$33\overline{1}$	48.5	6.7266 ± 0.0009	0.48 ± 0.06	0.6 ± 0.2
$33\overline{3}$	70.5	8.0186 ± 0.0009	0.50 ± 0.06	0.6 ± 0.2
$33\overline{5}$	84.9	10.1186 ± 0.0007	0.54 ± 0.06	0.5 ± 0.2

Table 10.1: Indices hkl together with the angle relative to the NW growth direction [111] are listed in the left. The table gives the length of the scattering vector K_{hkl}, the tilt $\Delta\omega$ and the calculated Zn concentration x in the $Cd_{1-x}Zn_xTe$ NW core for all K_{hkl}.

Dense CdTe NW ensembles show clear reflections in X-ray diffraction experiments. A SEM image of the sample discussed here is shown in Fig. 9.2 (a) in the previous chapter. RSM are recorded for the NW reflections $33\overline{5}$, $33\overline{3}$, $33\overline{1}$, 440, 331, 333 and 335. All of them are shifted by $\Delta\omega = 0.5°$ towards [001], compared to the lattice of the substrate. The relative tilt can be read out from the $\Delta\omega$-axis, shown for the representative RSM of the 333 reflection in Fig. 10.2 (a).

A plausible explanation for the NW lattice being tilted with respect to the substrate lattice is bending of the free-standing structures. During the growth process, the material sources switch from Zn to Cd after 2 min. After the material flux is exchanged, Zn remains solved in the catalytic droplet seeding the growth of CdZnTe as sketched in Fig. 10.1. A gradient for the relative Cd and Zn concentrations is expected within the seeds. Since the lattice constant of ternary semiconductors strongly depends on the relative concentration of elements, a gradient in the lattice constant of CdZnTe over the radial cross-section of the NW is the logical conse-

quence. The non-uniform lattice introduces forces bending the NW. The lattice constant of the NWs is calculated from the 2θ position of the reflections. Assuming Vegard's law, the values fit to a ternary $Cd_{1-x}Zn_xTe$ crystal with a Zn concentration of $x = (0.6 \pm 0.2)\%$, indicating very small amounts of Zn to be present in the whole NW. Most of the time, no Zn is supplied, hence we expect an axial gradient in the Zn-concentration along each NW as discussed in the following.

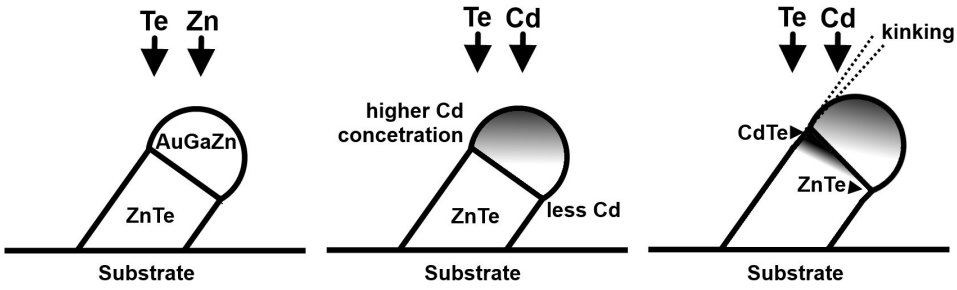

Figure 10.1: The images show a Cd gradient related to sample-source geometry.

An radially inhomogeneous distribution of Zn in the NW explains the tilt of the measured reflections. A second observation indicating an inhomogeneous Zn distribution along the wires is the asymmetric shape of the reflections as shown for 333 in Fig. 10.2 (a). While the intensity drops rapidly for smaller values of 2θ, there is significant broadening of the NW reflection to smaller lattice constant. For higher Zn concentration in the ternary compound, we expect a smaller lattice constant. After Zn is replaced by a Cd flux during growth, the Zn in the liquid seed is consumed by crystal growth. The probability for an incorporation of Zn into the growing wire decreases with a falling Zn concentration in the liquid seed. Thereby, an asymptotic decrease of the Zn concentration in the seed as well as in the latest grown part of the wire can be explained. That is in agreement with the discussed asymmetric broadening of the reflections to larger values of 2θ.

The analysis revealed single-crystalline CdTe NWs with a high ensemble uniformity. The NWs show sharp reflections in X-ray diffraction, indicating a high crystalline quality. A ZnTe growth start for CdTe NWs results in a Zn to Cd concentration gradient, which bends the NWs. A very small Zn concentration can be found in the entire NW core. The NW cores are subsequently overgrown with HgTe. The lattice mismatch of both materials introduces forces into the crystalline heterostructure. We want to use the reduction of symmetry in the unit cell to open a band gap for bulk charge carriers in our HgTe. To prove the symmetry reduction, the effects of residual strain in CdTe-HgTe NWs are discussed thoroughly in the next chapter.

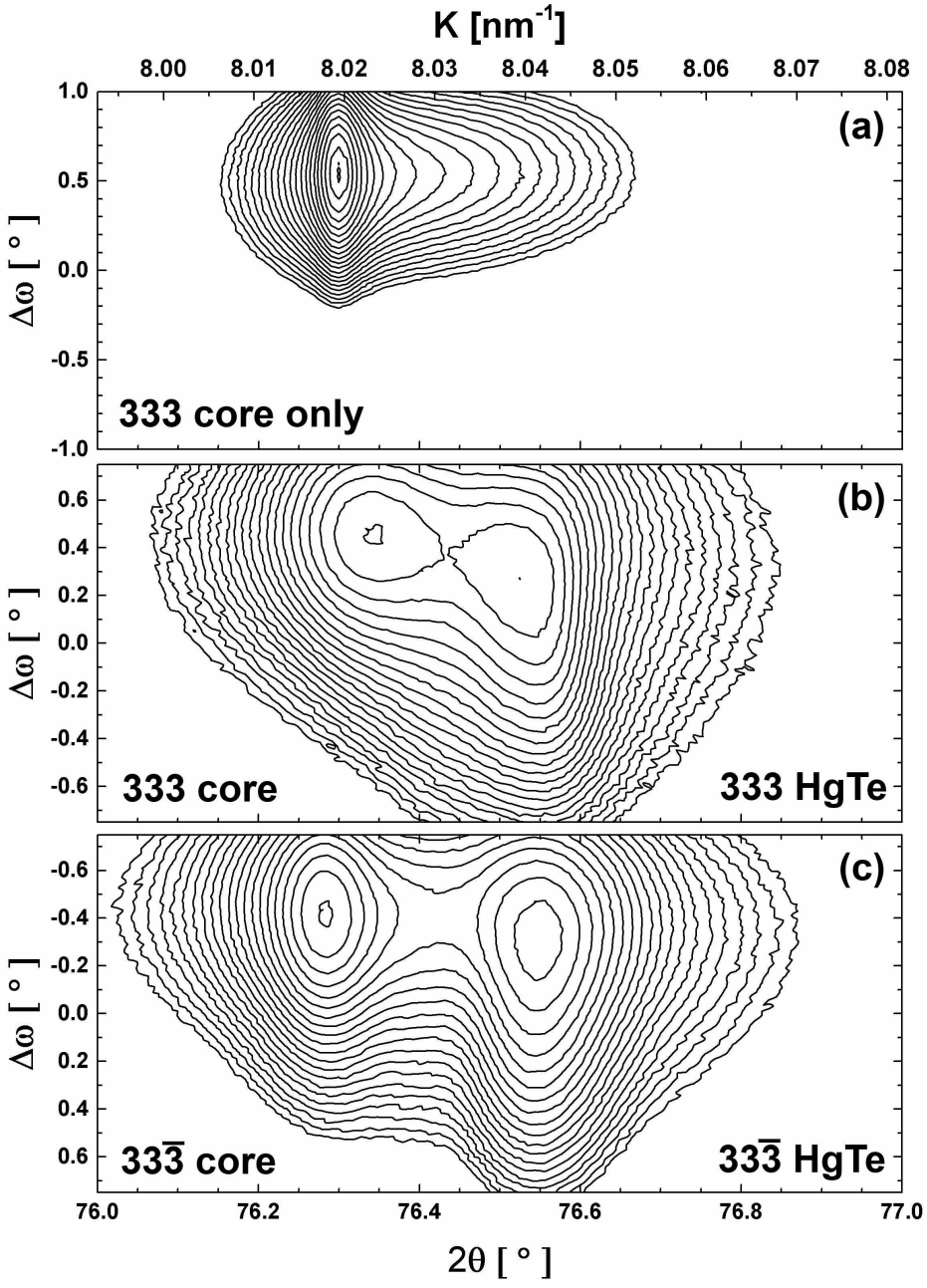

Figure 10.2: (a) 333 reflection of the bare NW cores. (b) 333 and (c) 33$\bar{3}$ reflections of the NWs overgrown with HgTe.

11 Residual strain in CdTe nanowires overgrown with HgTe

Here, heterostructures are analyzed for residual strain, where CdTe NWs are overgrown with HgTe mainly on one side facet. In this configuration, the superposition of many wires with semi-shells can be treated like the diffraction pattern of a single-crystalline substrate with an epilayer. Electron diffraction revealed, that the epitaxial interface of HgTe and CdTe NW is formed by $(11\overline{1})$A nanofacets and surface steps. Whether the mismatched hetero-interface gives rise to strain deforming the unit cell of the HgTe, is discussed in the following. To analyze the evolution of residual strain in the heterostructures, some CdTe NWs are transferred out of UHV without being overgrown with HgTe. The sample is cleaved under N_2 atmosphere. One part is subsequently overgrown with HgTe. The obtained CdTe-HgTe NWs, which are analyzed in this chapter, are shown in Chapter 9, Fig. 9.2 (b). Both parts are aligned equally inside the diffractometer, verified by reflections of the substrate.

RSMs are recorded for the same reflections as for the bare core and in each RSM two peaks are visible, corresponding to the lattice of NW core and HgTe, respectively. The intrinsic lattice constant of HgTe is smaller than the core's lattice constant, thus we find the HgTe reflection at higher values of 2θ. Two representative RSMs of 333 and $33\overline{3}$ are shown in Fig. 10.2 (b) and (c). The position of the 333 reflection of the core has changed after HgTe overgrowth, comparing Fig. 10.2 (a) and (b). This shift is the response of the lattice structure to the strain induced by mismatched heteroepitaxy. The relative change, as well as the absolute value for K_{hkl} are listed in Tab. 11.1 for all investigated core reflections. The black data points in Fig. 11.1 visualize the direction dependent relative compression $\frac{da}{a} \approx \frac{\Delta K}{-K}$ for the NW core, due to HgTe overgrowth on one side facet. The lattice of the core is compressed by $\sim$0.05% parallel to the interface. For the core, having instrinsically a larger lattice constant than HgTe, the measured compression in the plane of the interface is expected for pseudomorphic epitaxy. For the HgTe it should be vice versa. The finding of a changing lattice period for the overgrown core with respect to the bare one shows already, that strain is present in the CdTe-HgTe heterostructures.

hkl	angle $_{\text{to [111]}}$ [°]	$K_{hkl\ \text{NW core}}$ [1/nm]	$\frac{\Delta K}{K}_{\text{core}}$ [10^{-4}]	$K_{hkl\ \text{HgTe}}$ [1/nm]	$\frac{\Delta K}{K}_{\text{HgTe}}$ [10^{-4}]
335	-14.4	10.1280 ± 0.0007	8.0 ± 1.0	10.1464 ± 0.0007	-2.1 ± 1.2
333	0.0	8.0238 ± 0.0009	5.4 ± 1.6	8.0394 ± 0.0009	-2.8 ± 1.5
331	22.0	6.7288 ± 0.0010	3.3 ± 2.0	6.7429 ± 0.0009	-4.6 ± 1.7
440	35.3	8.7305 ± 0.0009	3.4 ± 1.4	8.7496 ± 0.0008	-5.8 ± 1.4
$33\overline{1}$	48.5	7.7268 ± 0.0010	0.3 ± 2.0	6.7439 ± 0.0009	-3.1 ± 1.7
$33\overline{3}$	70.5	8.0182 ± 0.0009	-0.4 ± 1.4	8.0413 ± 0.0009	-0.5 ± 1.5
$33\overline{5}$	84.9	10.1177 ± 0.0007	-0.8 ± 1.0	10.1478 ± 0.0007	-0.6 ± 1.2

Table 11.1: hkl for measured reflections and the angle relative to the NW axis [111] are listed in the left. For each reflection the length of the scattering vector K_{hkl} is displayed for the NW core after overgrowth of HgTe and for the HgTe itself. To show strain induced shifts, the relative change of the scattering vector length $\frac{\Delta K}{K}$ for the core, due to HgTe overgrowth, as well as $\frac{\Delta K}{K}$ for HgTe, compared to the reference value of a relaxed HgTe crystal, are listed.

In an undistorted zinc blende crystal, several reflections show the same scattering vector length K_{hkl}. For example 333 and $33\overline{3}$ are at the same 2θ position in the case of a relaxed zinc blende lattice. Comparing Fig. 10.2 (b) and (c), the absolute values for 2θ and the relative positions of the maxima are not identical for the two reflections. This finally proves, that residual lattice strain is present in the CdTe-HgTe NWs. To analyze the distortion of the lattice, we use a HgTe reference with $a_{\text{HgTe}} = (0.64615 \pm 0.00005)\,\text{nm}$. Within its error, this value covers common literature data, as well as the values obtained by our group fitting HRXRD measurements of HgTe layers on CdTe wafers. The measured value for K_{hkl}, as well as the relative shift $\frac{\Delta K}{K}$ with respect to the reference, are listed right-hand side of Tab. 11.1. The red data points in Fig. 11.1 visualize the direction dependent relative shifts $\frac{da}{a} \approx \frac{\Delta K}{-K}$ for HgTe grown on one side of CdTe NWs. For the stepped hetero-interface in our samples, the lattice is strained the most along [110], a direction 35° tilted to the interface, which is stretched by ∼0.06%. The observed deformation of the unit cell is a consequence of shear strain induced by mismatched heteroepitaxy. As sketched in Fig. 11.2, the stepped interface strains the HgTe along two directions at once, resulting in a shear component. Additionally to the in-plane stretch and the out-of-plane compressive response, a monoclinic distortion is stated. Shear strain leads to a further stretching of the lattice for directions close to [110], meaning around 35° to the interface.

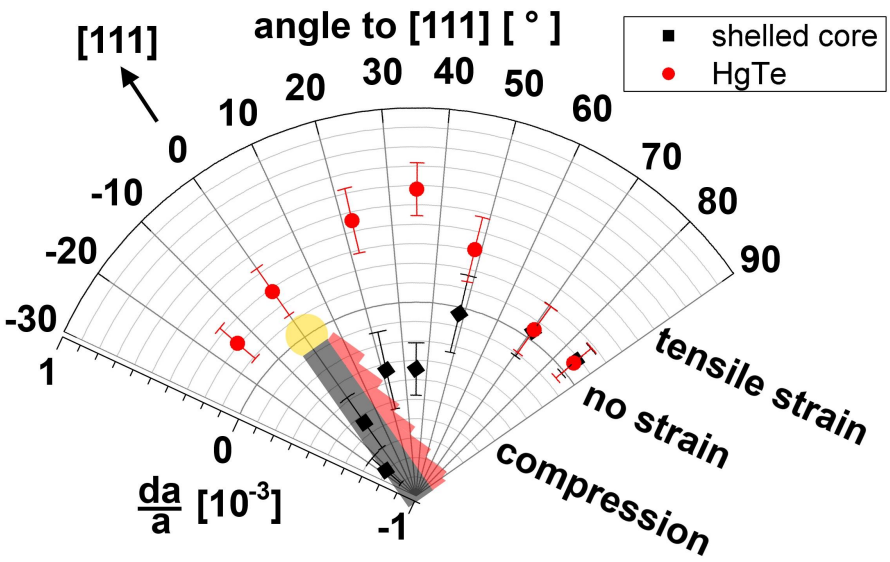

Figure 11.1: Direction dependent relative change of the plane spacing $\frac{da}{a} \approx \frac{\Delta K}{-K}$ by residual strain in CdTe (black) NWs overgrown with HgTe (red).

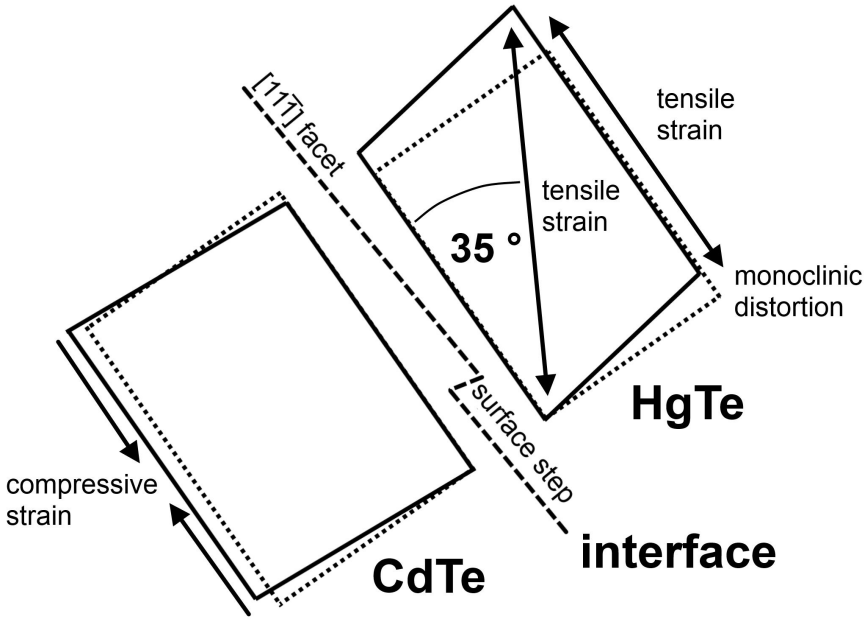

Figure 11.2: Sketch of the expected lattice distortion for mismatched epitaxy on a stepped interface. The relaxed unit cell in the $[1\bar{1}0]$ zone axis is depicted by the dotted boxes for comparison.

The overall changes by strain are smaller than the lattice mismatch of 0.3%. Some part of the strain may relax elastically at the edges and cornes of the small and free-standing NWs. Surface and edge effects always play an important role for nanostructures. We furthermore observe, that the lattice planes of HgTe are tilted by $\sim$0.1° with respect to the core lattice. Relaxation of tilted epilayers grown on lattice mismatched and stepped substrates were analyzed previously.[67] The origin of the tilt can be the Nagai's tilt[68] or the dislocations tilt.[69] The Nagai's tilt is caused by the elastic strain exerted by the substrate surface steps. Misfit dislocations are a possible plastic relaxation mechanism and 60° dislocations at the interface would furthermore tilt the local crystal structure.[71, 70]

Li *et al.* analyzed shear strained layers in the (Hg,Cd,Zn)Te material system,[66] to give an example for further reading. To the knowledge of the author, this is the first time, that shear strain in NWs was successfully characterized by an integrative method probing many NWs. The lattice mismatch of core and shell causes residual lattice strain. We measure about 0.05% compression for CdTe and about 0.03% stretching for HgTe parallel to their interface. The largest relative stretch of the HgTe lattice is 0.06% measured along [110], 35° tilted to the interface. This monoclinic distortion is caused by shear strain related to a stepped interface. The observation is in agreement with the stepped surface structure of CdTe NWs discussed in a previous chapter.

For the strained HgTe, the degeneracy of bulk bands if lifted.[72] According to that, strain turns the bulk to an insulating state, but the surface states should remain conductive. In order to prove this statement, the integration of the NWs into electronic circuits and charge transport investigations in the fabricated devices are subjects of the next parts.

Part III

Integration of nanowires into electronic circuits

12 Nanowire manipulation by dielectrophoresis

A fundamental requirement for follow-up transport experiments is to reliably integrate the NW heterostructures into electronic circuits. Nano-lithography on this material system proves to be challenging because of inherent temperature limitations, its high reactivity with various metals and its properties as a topological insulator. Previous work gives an insight, why established semiconductor lithography processes cannot be easily transferred to HgTe layers and furthermore provides alternatives.[73, 74] The prior work covers a general description of electron-beam lithography, which is also used in this work. Here, the focus lies on the special requirements arising from the NW geometry. The first challenge is to manipulate individual NWs on a lithography substrate, in order to be able to localize and contact them.

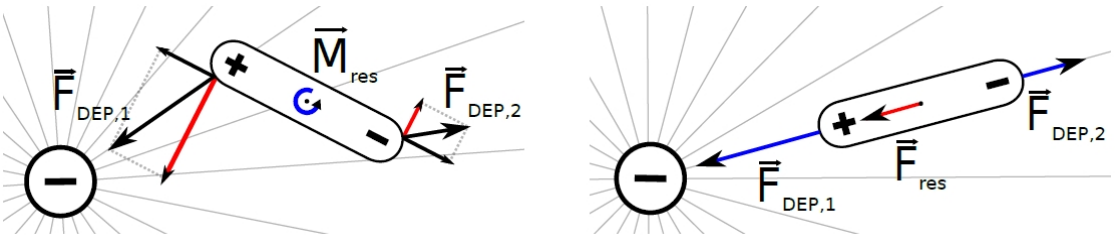

Figure 12.1: The images show a polarized particle in an inhomogeneous electric field. The forces $\vec{F}_{DEP}$ on the dipole result in a torque $\vec{M}_{res}$, aligning the particle parallel to the electric field lines. The imbalance of forces leads to a non-vanishing total force $\vec{F}_{res}$ acting on the particle. The images are taken from [77].

Dielectrophoresis (DEP) is a very effective method for the contact-free manipulation of nano-sized objects. To give a brief introduction, DEP is the motion of a polarized particle in an inhomogeneous electric field $\vec{E}$.[75] The NWs are suspended

in a liquid medium. By applying a voltage to an electrode, which is submerged with suspension, the NWs in the liquid get polarized. The effective forces on both ends result in an orientation of the NW along the field lines and furthermore attract them towards the electrode. The situation is sketched in Fig. 12.1.

The DEP force depends on geometry, particle material and medium. In the following, we use the effective dipole moment model to qualitatively describe the frequency dependence of DEP. We get the total force [76]

$$\vec{F}_{\mathrm{DEP}} = \frac{\pi a^2 b}{6}\, \varepsilon_m\, \mathrm{Re}[f_{CM}]\, \nabla E^2, \tag{12.1}$$

for a spheroid with length b and radius a. For attractive force, the Clausius-Mossotti factor f_{CM} is positive. The factor depends on the orientation of the NW in the electric field $\vec{E}$. For the field along the long axis we get

$$f_{CM}^{\mathrm{long}} = \frac{\varepsilon_{\mathrm{NW}}^* - \varepsilon_m^*}{\varepsilon_m^*} \tag{12.2}$$

and for the field along the short axis

$$f_{CM}^{\mathrm{short}} = \frac{\varepsilon_{\mathrm{NW}}^* - \varepsilon_m^*}{\varepsilon_{\mathrm{NW}}^* + \varepsilon_m^*}. \tag{12.3}$$

The index m refers to the suspension medium. We use the complex dielectric function $\varepsilon^* = \varepsilon - i\frac{\sigma}{\omega}$, where ε is the dielectric constant and ω the frequency.[78, 79] We expect an alignment along the field lines as long as $f_{CM}^{\mathrm{long}} > f_{CM}^{\mathrm{short}}$.

For isopropanol (IPA) as a medium ($\varepsilon_m = 18.6$, $\sigma_m \to 0$) and HgTe-based NWs ($\varepsilon_{\mathrm{NW}} \approx 20$, $\sigma_{\mathrm{NW}} > 0$) we expect an attractive DEP force with alignment for DC and AC frequencies up to the GHz range.

To get the NWs off from the growth substrate and suspended into the IPA, we use ultrasonic cavitation at 37 kHz. Figure 12.2 gives an overview of the NW ensemble after harvest by ultrasound. The inset in (a) shows the sample before harvesting for comparison. The vertical wires are ripped off (red arrowheads), while most of the wires growing with an angle of 19° stay on the growth substrate (dashed blue lines). Figure 12.2 (b) is a top view image with the in-lens detector of the SEM nicely showing the topography and (c) is the corresponding image taken with the detector for elastically backscattered electrons, showing material contrast of core and shell. The NWs are successfully transferred into the suspension. Most of the suspended wires are vertically grown ones and have a closed HgTe shell. Typically, 1-3 ml IPA and about 4 mm^2 as-grown substrate are used for each harvesting process. The suspension is very handy to control the density of the wires. It can be diluted with

IPA, or one can leave the vial containing the suspension open for a while, then the evaporation of IPA at room temperature effectively increases the NW density over time. When a suspension is stored for some days, ultrasound must be applied again, since the wires seem to attach to the walls of the vial.

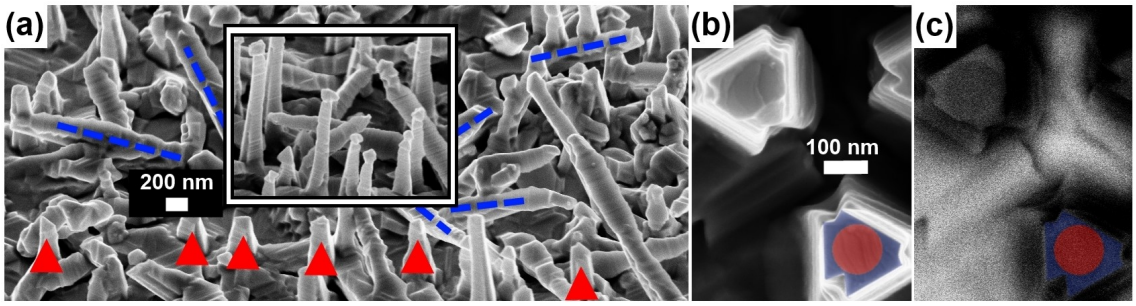

Figure 12.2: The images show a harvested piece of substrate. The inset in (a) shows the as-grown sample for comparison. The top view images in (b) and (c) show the typical shape at the wire bases and core-shell material contrast, highlighted with false colors.

In order to perform DEP, we furthermore need an electrode to attract and align the NWs. The electrodes, consisting of 5 nm Ti and 20 nm Au, are defined together with alignment markers by electron beam lithography. Later, the markers are used to define leads ending on the attracted wires. The process to realize the alignment structures is not very critical. One can use the same parameters as for the definition of the contact leads, which are listed in the Appendix. The use of a highly doped Si substrate covered with 100 nm thermally oxidized SiO_2 for the follow-up lithography allows to apply a back-gate voltage to the NWs, which is intended to influence the charge carrier density of the wires.

Micro-manipulators and an optical microscope are used to apply a voltage to the DEP electrodes. In this work, the method is tested for DC and AC up to 10 MHz with peak voltages in the range of ± 10 V. The voltage is applied first, then a droplet of suspension is added. After one to ten minutes, depending on the NW density in the suspension, the liquid is blown off the substrate with an airflow. If the IPA would evaporate completely, before the process is finished, one can simply add another droplet of suspension. For frequencies in the MHz range, the NWs are attracted to the edges of the electrode and many of them are oriented perpendicular to the edge. Figure 12.3 shows electron micrographs of NWs aligned like this.

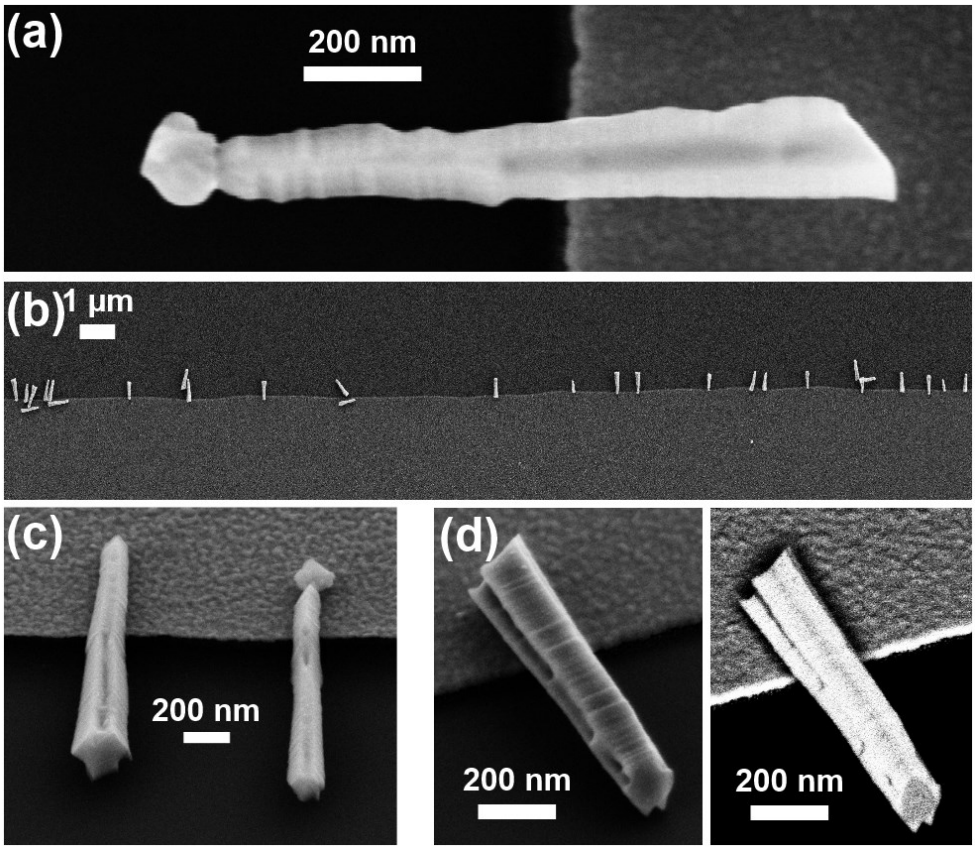

Figure 12.3: All images are electron mircographs of NWs manipulated by DEP. The lowermost images show that the wires can break and some of them loose the catalytic droplet seeding the growth. The right image in (d) is taken with elastically backscattered electrons and shows core-shell material contrast.

The desired effect is observed for frequencies above ∼500 kHz. For lower frequencies as well as for a DC voltage, no attraction occurs. This is not explained by the frequency dependence of the Clausius-Mossotti factor. Assuming mobile ions to be present in our suspension, the suppression of DEP can be understood. Hermann von Helmholtz was the first who realized, that a conductor in contact with a liquid ionic conductor exhibit layers of opposite polarity at the interface.[80] This electrical double layer shields the electrode. The potential drop occurs directly at the interface and $\vec{F}_{\mathrm{DEP}}$ acts only on a very short range. For high frequencies, the ions with inertial mass can not form the double layer fast enough and DEP occurs on the required range to attract the suspended NWs. For now, we neither know, which kind of ions cause the effect, nor where they come from.

In this work, a DEP frequency of 1-2 MHz is used to attract and align NWs for the follow-up experiments. The electrode is located in a coordinate system with alignment markers in the corners. These structures are used to define the contact leads ending at the NWs' coordinates, as described in the next chapter. After DEP is finished, the sample is covered with PMMA in the spin-coater. The resist is used for subsequent lithography and fixes the position of the wires, that might change a bit during spinning. Figure 12.4 (a) shows an image of wires, electrode, coordinate system and alignment markers, recorded with the optical microscope. The wires are clearly visible with the SEM, as shown in the inset. We use the optical microscope at this stage to avoid damage of the wires and exposure of the resist by electrons. Then, contact leads are defined, ending at the NWs as shown in the false-color image in Fig. 12.4 (b).

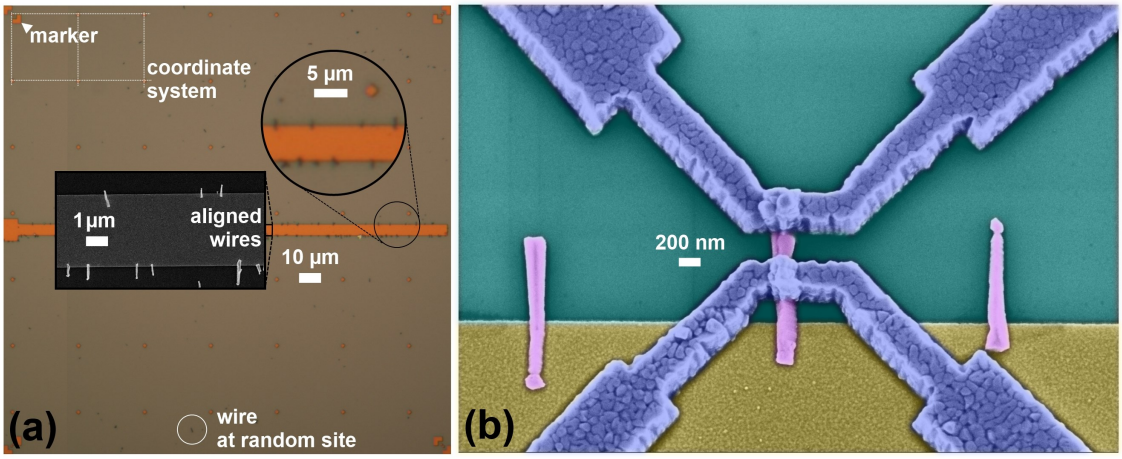

Figure 12.4: The NWs are attracted to an electrode, and can be localized in the coordinate system in (a). The alignment markers are used to define metallic contacts (blue) on the NWs (red) in the false-color image (b). The back-gate insulator (green) is partially covered with the electrode (yellow).

Summarizing this chapter, our NWs can be manipulated successfully by DEP. The alignment, where most of the wires are parallel oriented, is a great advantage for the measurements presented in Chapter 15, with a magnetic field parallel to the NW. With this method, several NWs can be investigated in a parallel field on one chip-carrier. The development of reliably working metallic contacts for charge transport characterization is discussed in the next chapter.

13 Metallic contacts

The last chapter explained how to localize and align NWs for subsequent lithography of leads intended to contact the NWs. The parameters to do so can be found in the Appendix. This chapter discusses the special requirements arising from the NW geometry and describes the development of a reliable process. The aligned NWs have a height of 100-200 nm and the leads need to overcome the height difference between substrate and NW. The used double-layer resist must be sufficiently thick and undercut after development, to be able to evaporate and lift-off enough metal. A minimum of 300 nm is needed, in order to close the gap, which can form due to the height difference. Such gaps are denoted with red arrowheads for samples, which have an ambitious geometry with finger-like contacts, shown in Fig 13.1 (a) to (c).

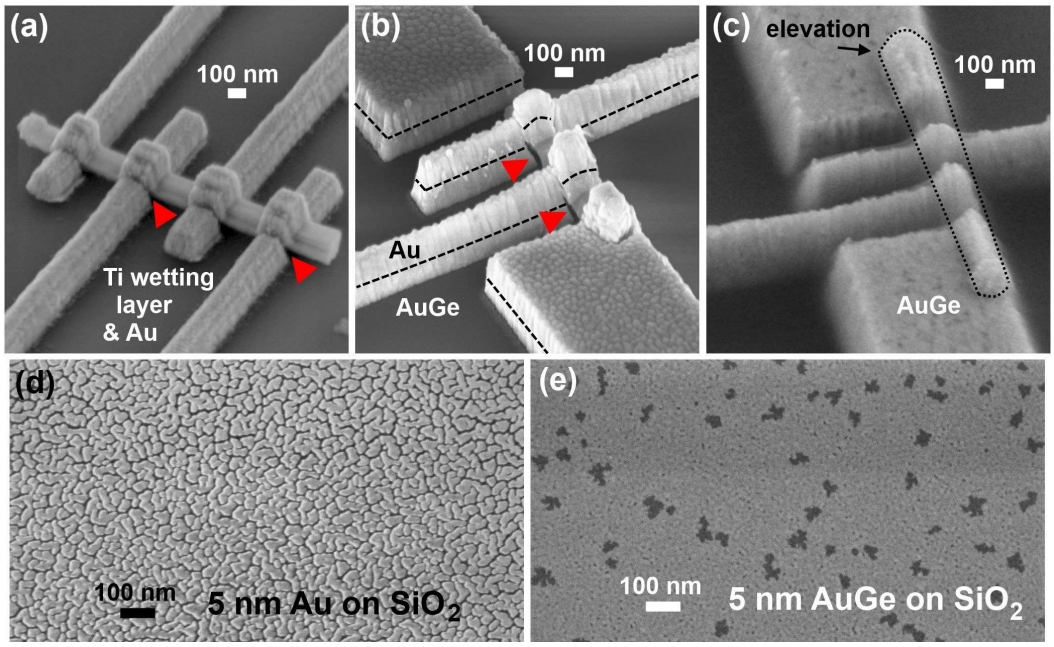

Figure 13.1: The images in the upper row show a 4-terminal sample geometry. The insufficient wetting behavior of Au in (d) compared to AuGe in (e) leads to the gaps, denoted by arrowheads in (a) and (b).

Figure 13.1 (a) is an example with four thin, Au-based and finger-like leads having only small overlap with the NW. This structure shows the gaps mentioned before. At this stage of development only bigger leads allowed for charge transport experiments, since they cover much larger areas. But also in the geometry with larger overlap, only very few of the applied contact pairs were working. Measurements on such devices can be found in [81]. From the first characterization we already know, that our HgTe is conductive, but the measured resistances were not stable over time and showed huge fluctuations from sample to sample. In order to improve the process, we change the contact material from Au to AuGe. The images in Fig. 13.1 (d) and (e) show the wetting of thin Au- and AuGe-layers on SiO_2. For Au we see the clusters, which are the precursors for columnar growth. For AuGe, the substrate is homogeneously covered in large areas (bright), but we see some voids (dark), which close over time when more material is deposited. The columnar growth of Au increases the issue of gap-formation directly at the NW compared to AuGe contacts. By the use of thick AuGe-Au contacts in Fig. 13.1 (b), the gaps can be observed and also the devices were not working reliably.

The cleaning step, which is explained later, together with thick AuGe contacts increases the yield of working contact pairs to the order of 10%. Despite many devices were fabricated like this, we were not able to reproduce the device in Fig. 13.1 (c). All four contacts were working for this sample and we got functional finger-contacts in the middle of the wire for the first time. The contacts at the ends have larger overlap and were working for a small fraction of devices before we started to clean the contact area by etching. We draw the conclusion, that the removal of oxide and resist residuals and also the wetting of the metal are crucial to get ohmic contacts in the case of very small contact areas. Unfortunately, the working sample in Fig. 13.1 (c) was destroyed during a pre-characterization measurement by electric discharge, before being fully characterized. In the image of the 4-terminal device, we can still see the elevation in the metal, caused by the NW underneath, while the parts between the contacts are gone. The measurements on this device can be found in [82]. Since we were not able to reproduce such a 4-terminal sample so far, the results are not included in this thesis. Here, the focus lies on a more reliable process, which has been developed in order to characterize and compare many NW-devices fabricated by the same method.

As one can see in the examples shown previously, the NWs are not in the center of the contact structure. Sometimes the leads even miss the NW. This is caused by unintended sample movement inside the electron microscope used for exposure. If the sample is clamped on the holder several hours before starting the exposure, then the position stabilizes over time and the outcome is very accurate.

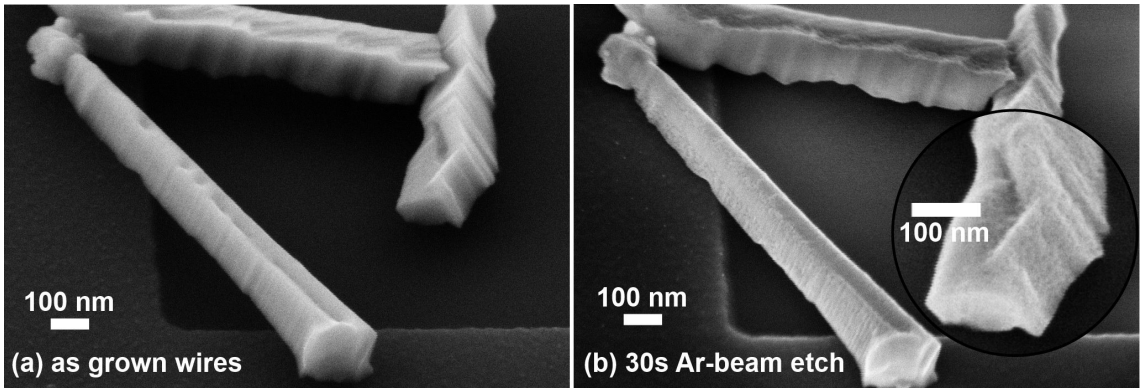

Figure 13.2: The images show NWs before and after etching. The typical faceted surface is visible in (a). The Ar-beam creates a rough surface in (b), visible in the magnified inset.

For contact cleaning, we use an Ar-beam inside the in-situ cluster, also used for subsequent metalization. The images in Fig. 13.2 show NWs before and after etching, with roughening of the facets exposed to the Ar-beam. Thus, etching occurs not very homogeneous. As a consequence, we expect many crystal defects. Since etching is needed to get working contacts, we are not able to leave out this step, but we keep the etching time short and 6-8 s are found to be close to ideal.

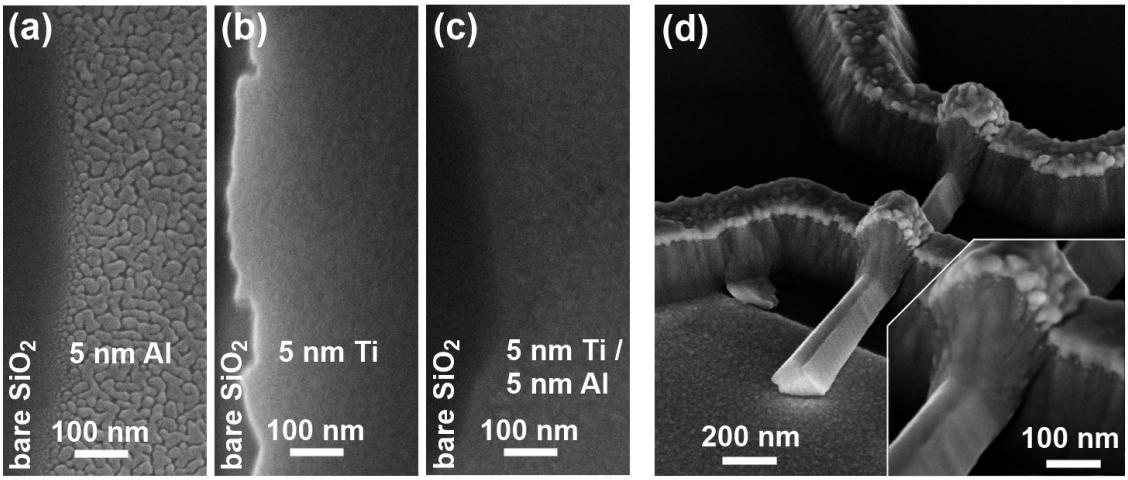

Figure 13.3: Wetting of (a) Al, (b) Ti and (c) Ti-Al layers. For Ti contacts in (d), the height difference is overcome continuously by the metal (see inset).

To further increase the yield of working samples, we tried a different contact geometry and also other contact materials. The choice of Al as a contact material is mainly motivated by the fact, that Al is a superconductor. For temperatures above 1.2 K, we expect ohmic transport, below 1 K the interesting interface between our NWs and a superconductor is formed in the case of Al-based contacts. Leads consisting of Al and nothing else show the gaps directly at the NWs and do not work properly. The electron micrographs in Fig. 13.3 (a) to (c) show the wetting for thin layers of Al, Ti and a combination of a Ti wetting layer covered with thin Al. For comparison, all of them show a boundary to a bare region of the substrate, where no metal was deposited due to a shadow mask. We see the insufficient wetting for Al, which is not present for Ti, where we get a very homogeneous layer. If we use thin layers of Ti, then the subsequent metalization with Al is also much smoother. For pure Ti contacts, we do not observe a gap at all. An example with continuous contacts approaching the NW is shown in Fig. 13.3 (d). Instead of the very thin finger-leads we now use four independent leads, merging pairwise at the NW. In this pseudo 4-terminal geometry, the NW/contact interface resistance comes into account. The resistance of the leads is not measured in this case, because different leads are used as current path and voltage probe. This geometry has the advantage, that each contact can have a effectively larger overlap with the NW, compared to the finger-like leads. The increased overlap, together with the evaporation of pure Ti-, or Al-contacts with a thin Ti wetting layer, resulted in a yield of working contact pairs in the order of 90%. Problems arising from the NW geometry are thereby overcome successfully.

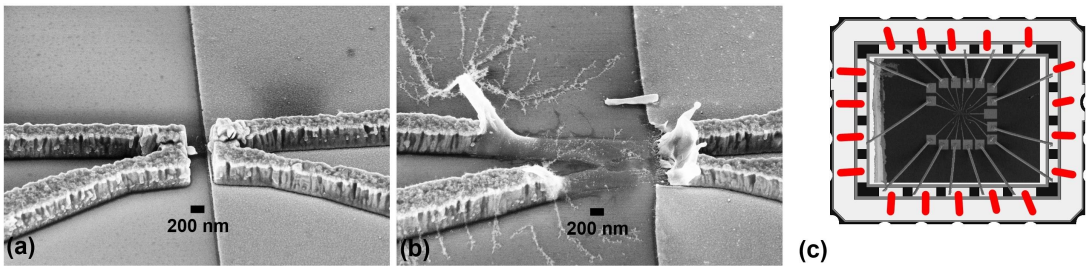

Figure 13.4: The images (a) and (b) are examples for samples destroyed by the bonder. To avoid electric discharge, the red bonds in (c) must be connected, before bonding from the sample to the chip-carrier. (Sample and chip-carrier are not scaled correctly.)

Mesoscopic structures like our NWs are very sensitive to discharge. During handling, the operator needs to be properly grounded. Also all machines used, for example the bonder to connect the leads to a chip-carrier, need to be at equal potential. Each

grounded setup is suffering from environmental high-frequency pick-up. We found the amplitude to be critical in our cleanroom, where the bonder is located. Many NWs, mainly those having the mentioned contact gaps, exploded during bonding. The contact gap can be understood as a nano-capacitor storing the energy of the pick-up pulse. The size of the contact gap is very small and an electric breakthrough can vaporize the whole structure. Sometimes, only the wire melts and is solidifying as a sphere. Examples are shown in Fig. 13.4 (a) and (b). No discharge is observed, when the needle of the bonder and the chuck holding the chip-carrier are shorted and furthermore all chip-carrier pads are connected by the red bonds in Fig. 13.4 (c) before bonding from the sample to the chip. The red bonds ensure, that both sides of the NWs are on the same potential during bonding. Of course, they need to be removed, before cooling down the sample. The removal of the protection bonds is not critical, as long as the operator is properly grounded and uses a metallic tweezer to rip off the bonds.

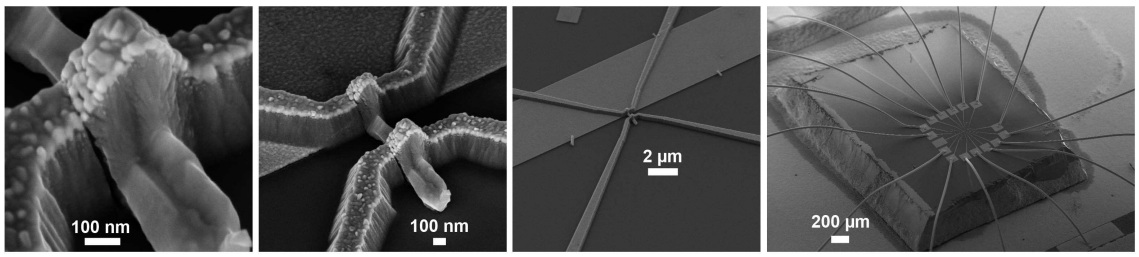

Figure 13.5: The images show the successful integration of a NW into an electronic circuit.

The images in Fig. 13.5 show, we integrate NWs into electronic circuits successfully. The example shown here has Al-based contacts on a thin Ti wetting layer and shows the gap of the contacts only at the very thick end of the NW. This device works. With all the developments, we are able to contact the different sizes of NWs reliably. The gaps, still occurring for Al-based contacts, are overcome by the Ti-wetting layer in combination with contacts evaporated long enough, giving a lead thickness larger than the height of the NW.

The sample in Fig. 13.6 (a) shows, that sometimes we contact NWs, which are overgrown with HgTe on one side. For this special case here, the HgTe is facing the substrate, a situation discussed in Chapter 16. The sample shown here is insulating, since the HgTe vaporized between the contact leads. Interestingly, the CdTe-core is still present. The sample in Fig. 13.6 (b) was successfully characterized at low temperature, but in the end it was destroyed by a breakthrough of the back-gate to one of the leads. The investigations on charge transport follow in the next part.

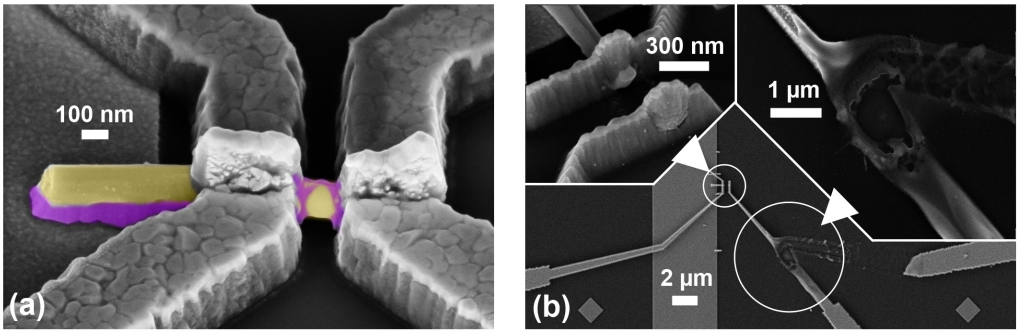

Figure 13.6: In (a), the CdTe core (yellow) is overgrown on one side with HgTe (purple). The HgTe vaporized between the leads, but the core is still present. The wire in (b) was destroyed by a gate breakthrough.

A typical sample used for charge transport is shown for different view directions in Fig. 13.7. The sample was mounted on different sample holders for the upper and lower row of images, respectively. In the upper row, the NW is clearly visible. During re-mounting to record the lower row, the operator was not grounded and used a plastic tweezer. A discharge event vaporized the NW between the contacts. The splash-like residuals are pointed out with red arrowheads. We see, proper grounding of the operator is very important during sample handling.

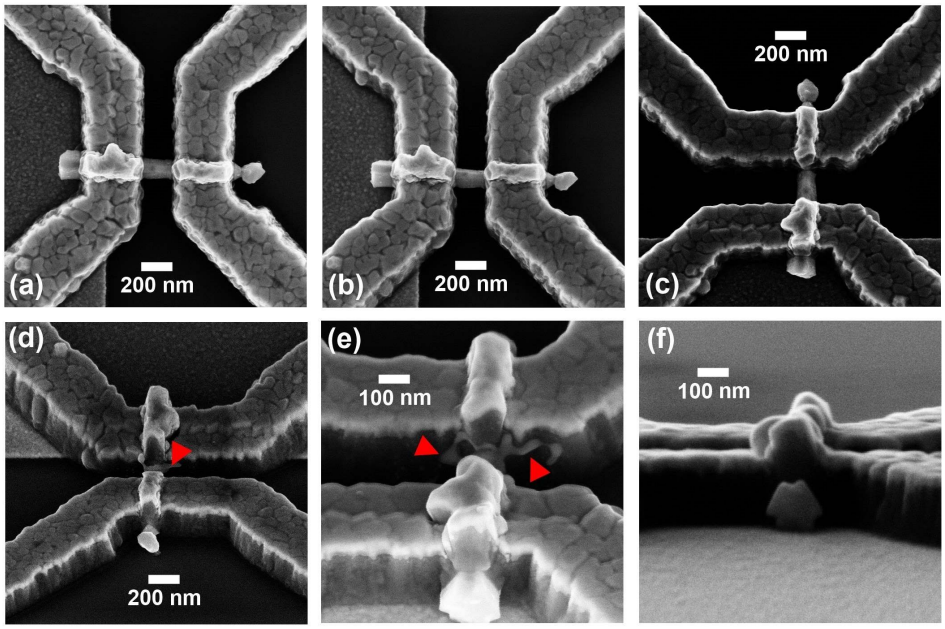

Figure 13.7: The images show a typical transport sample in different view directions. The NW is destroyed between the contacts in the lower row, the residuals of the discharge event are pointed out with red arrowheads.

Part IV

Charge transport in HgTe nanowires

14 The gate effect and magnetoresistance

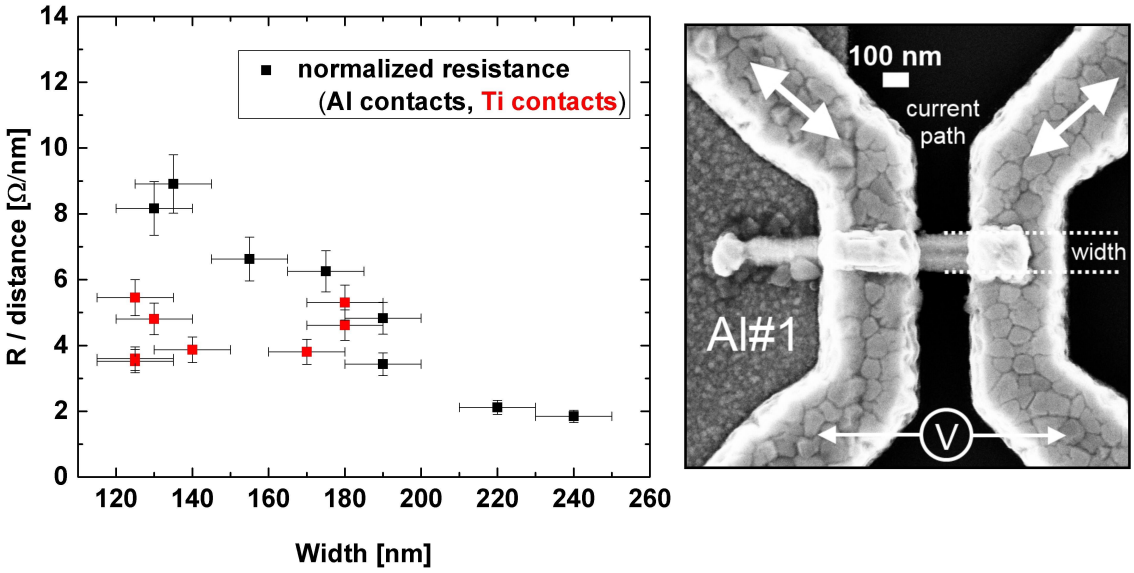

Figure 14.1: Resistance normalized to the contact distance for different wire widths and contact materials together with an exemplary SEM image of a sample.

Previous work on HgTe layers shows clear signatures of surface transport.[83] Here, the transport properties of CdTe-HgTe core-shell NWs (HgTe-NWs) are characterized for the first time. Charge transport is carried by states described by the energy dispersion.[55] Excitation, gate and magnetic field dependent resistance measurements can give insight on the electronic structure of low-dimensional samples.[84, 85] To measure phase coherent charge transport phenomena, the samples are characterized inside a ^{3}He/^{4}He dilution refrigerator at a base temperature below 100 mK.[86] The signal is filtered by lossy coaxial cables at base temperature and π-filters at room temperature to reduce noise. Furthermore, the signal is actively amplified by 60 dB after leaving the cryostat. Nano-voltmeters allow precise DC measurements. AC signals are measured with lock-in amplifiers at 113 Hz frequency. The resistance

is calculated from the voltage drop across a known serial reference and the voltage drop across the NW in a quasi 4-terminal geometry. In this configuration, independent leads are used as current path and voltage probe, but they meet directly at the NW. In the following, charge transport measurements are discussed for HgTe-NWs with Aluminum contacts having a thin Titanium wetting layer and with pure Titanium contacts. These contact materials show reproducible and stable contact resistances and a high yield of working contact pairs. The samples have different contact distances and NW widths. An overview, including SEM images and a table with basic parameters for an easy comparison of different samples discussed in the following, is attached in the Appendix of this work. Figure 14.1 shows the resistance normalized to the contact distance as a function of NW width, in order to reveal the influence of the geometry on the resistance. For NWs contacted with Al, a trend of increasing resistivity with decreasing NW width appears in the dataset. NWs contacted with Ti have a rather constant resistivity for different widths. The sample pool is too small to draw any concrete conclusions from this observation and the trends observed can also be explained by a statistical variation in device quality.

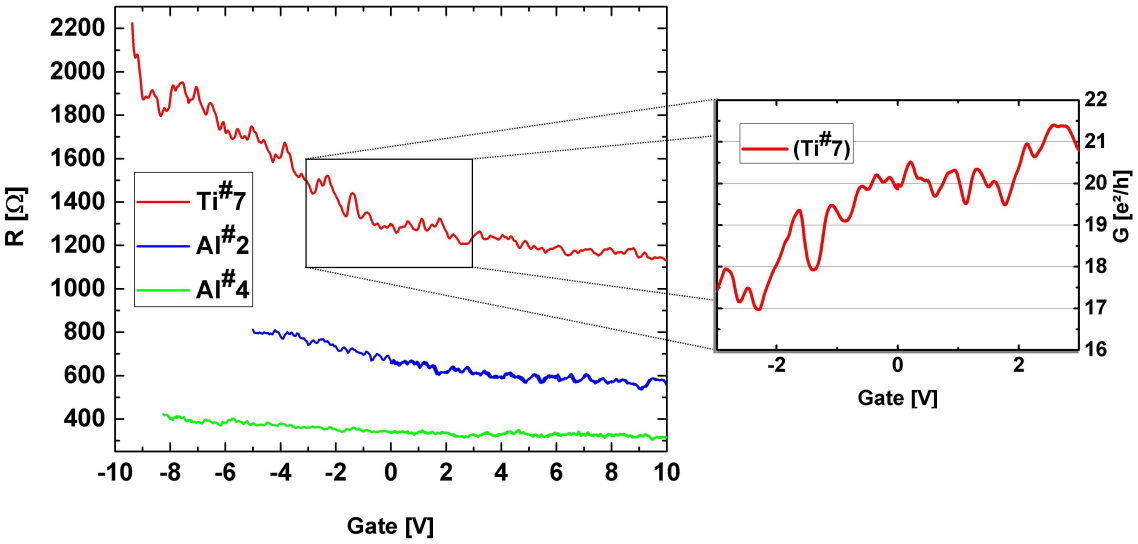

Figure 14.2: The resistance of different samples, when a voltage is applied to the back-gate. The inset shows the conductance fluctuations of one of the samples.

Fig. 14.2 shows the variation of NW resistances with applied gate voltage. The traces are measured twice for positive gate voltages to show reproducibility. The overall trend of an increasing resistance with decreasing gate voltage is explained by a manipulation of the charge carrier density. The electrostatic gate potential changes the position of the Fermi-level with respect to the electronic structure of

the HgTe-NWs, either populating (positive gate voltage) or depopulating (negative gate voltage) electronic states. Additionally, we observe aperiodic fluctuations in resistance. If plotted as gate dependent conductance, then the random fluctuations have similar height $< \frac{2e^2}{h}$. This is pointing in the direction of universal conductance fluctuations (UCFs) discussed in detail after having a look on the magnetoresistance.

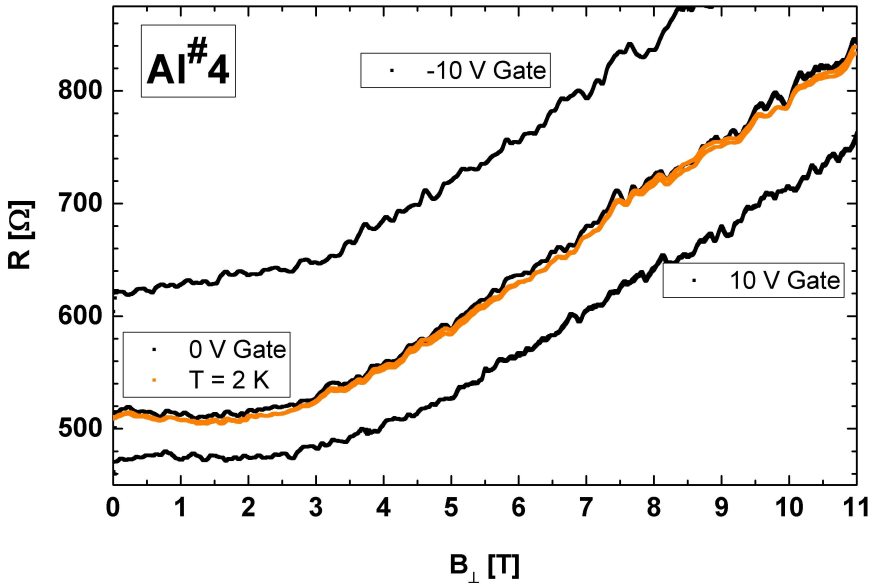

Figure 14.3: Magnetoresistance due to a magnetic field perpendicular to the wire axis for different gate voltages and temperatures. All black curves are measured at 100 mK.

For a magnetic field perpendicular to the NW axis, Fig. 14.3 shows a rather constant value for small fields up to about three Tesla and then a positive magnetoresistance of 8-9% per Tesla, which is non-saturating in the measurement range. The overall characteristic does not change by variations in gate voltage and temperature. For different gate voltages, the magnetoresistance curve is shifted. As typical for UCFs, we observe fluctuations for changing magnetic field, which are analyzed later in this chapter.

Fig. 14.4 compares the magnetoresistance for samples contacted with Al and measured in a magnetic field perpendicular to the NW axis. The sharp feature at small fields for measurements at 100 mK is caused by superconductivity, which is a topic of Chapter 17. The overall curve can either be described by a parabolic or in sections by linear fits. The magnetoresistance is symmetric for reversed field direction. To give examples for comparison, the plot includes both a parabolic and a linear fit for the magnetoresistance of two samples. Literature addresses different reasons for a linear

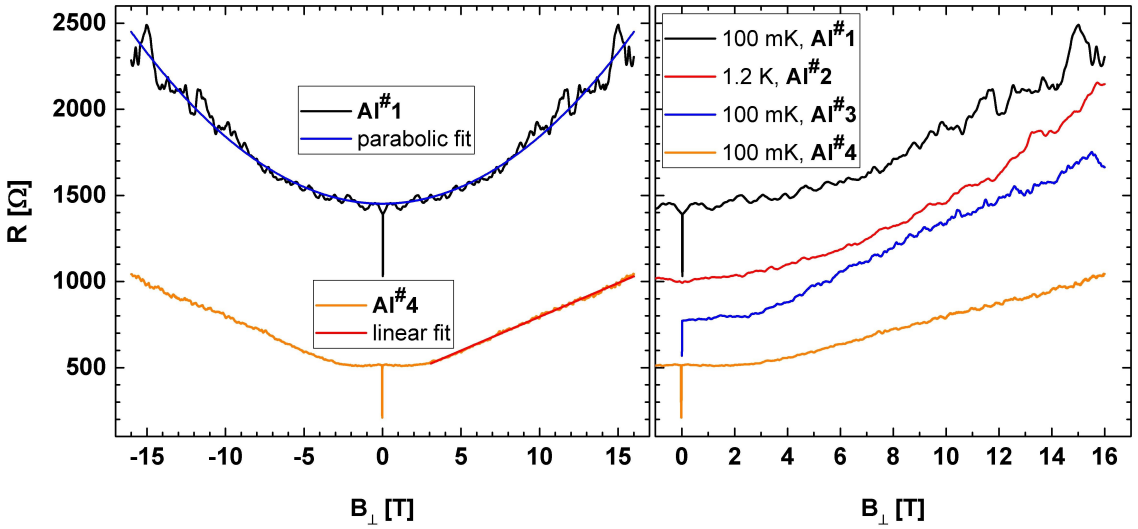

Figure 14.4: Magnetoresistance of different samples with Al contacts.

magnetoresistance.[87] One classical model assumes a three-dimensional inhomogeneity in the charge carrier mobility and/or density leading to a zigzag, rather than an one-directional current-flow. As a consequence, a linear magnetoresistance can be derived by the model.[88, 89] A quantum mechanical model on the other hand links a Dirac-like dispersion relation to the observation of a linear magnetoresistance.[90, 91] Ambipolar charge transport with different relative mobilities for electrons and holes can lead to very different dependencies of the resistance on magnetic field. For metals with an equal conductivity of electrons and holes a quadratic magnetoresistance is expected.[92] The number of samples is too small to draw any concrete conclusions. The observations can be attributed to charge transport in metallic surface states, transport by a occupied bulk conduction band or a combination of both.

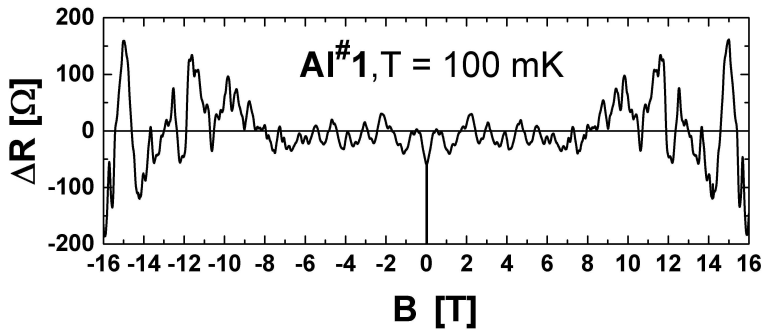

Figure 14.5: The graph shows aperiodic fluctuations, which are symmetric for reversed field.

The parabolic or linear background is subtracted from the data to analyze the fluctuations. Figure 14.5 shows, that they are aperiodic and symmetric for reversed field direction, which is typical for UCFs. UCFs are manifestations of quantum interference in mesoscopic systems. An external magnetic field influences the phase shift of electron trajectories.[93] For low temperature the interference of many random paths results in characteristic conductance fluctuations in the order of $\frac{e^2}{h}$.

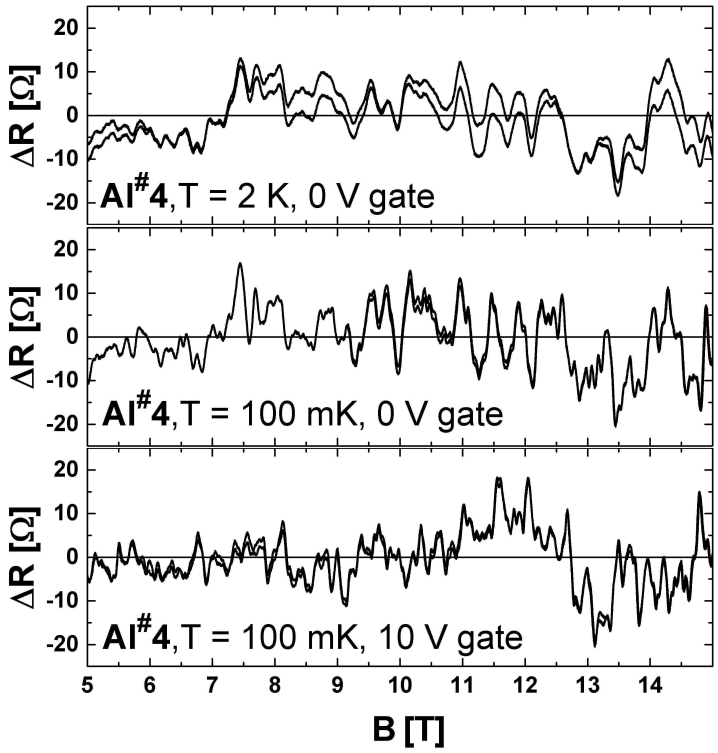

Figure 14.6: The graphs show the resistance fluctuations of one sample at different temperature and gate voltage.

Fig. 14.6 shows fluctuations in resistance at different temperatures and gate voltages. They smear out at higher temperatures, because they are an interference effect and phase coherence is best at low temperature. For varied gate, the features appear randomly. In low-dimensional samples with disorder, the trajectories are defined by the sample geometry and an inhomogeneous distribution of scattering sites. The transport of electrons through the disordered system is considered as a scattering problem where electrons can be reflected by a random potential.[94] Hence the scattering sites are unintended and distributed randomly, the measured conductance fluctuations vary from sample to sample. They appear to be random, but the fluctuations represent the static properties of each sample and are reproduced repeating the same measurement. Assuming that sufficient large changes in the

Fermi-level are equivalent to a change of the set of possible trajectories, the random fluctuations for magnetic field and gate dependent measurements are explained.

Additionally, some samples with Ti contacts are characterized in a perpendicular magnetic field to verify the results above. Figure 14.7 shows the magnetoresistance for different samples with Ti contacts. The curves are symmetric, show fluctuations reproducible for small changes of excitation and can be fitted by either parabolic or in sections by linear approximations. At higher fields the curves behave similar to the measurements with Al contacts compared to the statistical variation from sample to sample contacted with the same metal. Regarding the whole sample pool, the magnetoresistance is in the range of 5-15% per Tesla. The interesting difference is the feature for magnetic fields below 0.3 T. We have a special contact configuration for the samples with Ti contacts, visible in the overview in the Appendix, where one of the contacts possibly lies on the metallic droplet seeding the growth. The resistance minimum at small fields is caused by superconductivity in the metallic droplet, thoroughly discussed in Chapter 16.

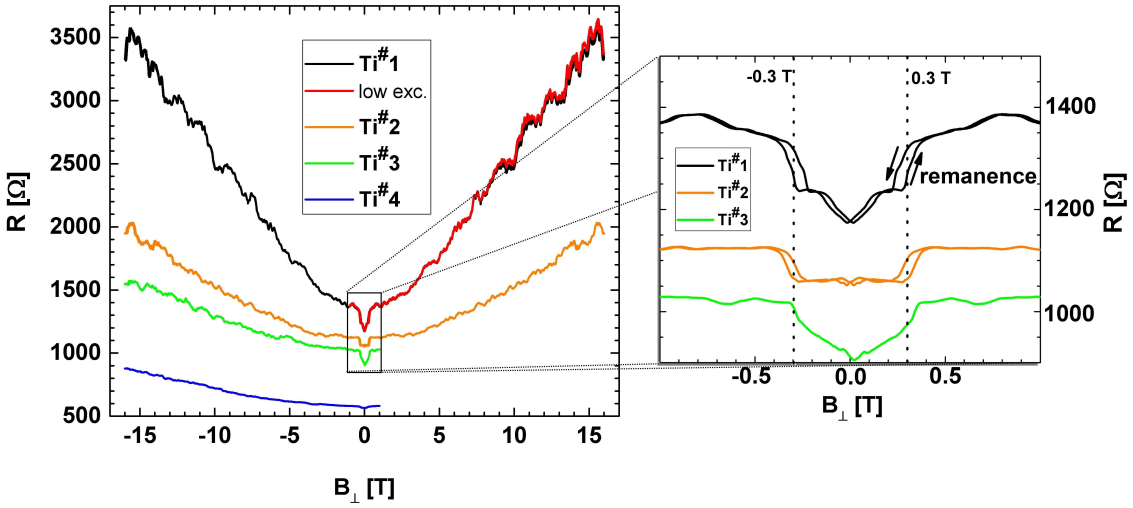

Figure 14.7: Magnetoresistance of samples with Ti contacts at 100 mK. The shift, observed for reversed sweep direction, is caused by the remanence field.

The findings point to a mesoscopic, rather localized transport regime in the HgTe-NWs. The samples are neither ballistic, nor diffusive. The number of inelastic scattering events is low, allowing for the observation of phase coherent transport effects. We draw the conclusion, that the mean free path in our HgTe-NWs is smaller, but the phase coherence length is larger than the sample length of several hundred nanometers.

15 Phase sensitive charge transport

If the mean free path allows for coherent motion of charge carriers along the short perimeter, then NWs with conductive shells host angular momentum states. These states give rise to magnetic flux periodic conductance oscillations.[95, 96] Resistance of the NWs as a function of a magnetic field parallel to the NW is measured similar to the curves shown before. The results are compared for samples with the two different contact materials. A model for charge transport in the surface states of a topological insulator NW with periodic boundary conditions along the short perimeter and diffusive transport along the long axis follows. The resistivity obtained from simulation is compared to the experimental findings at the end of this chapter.

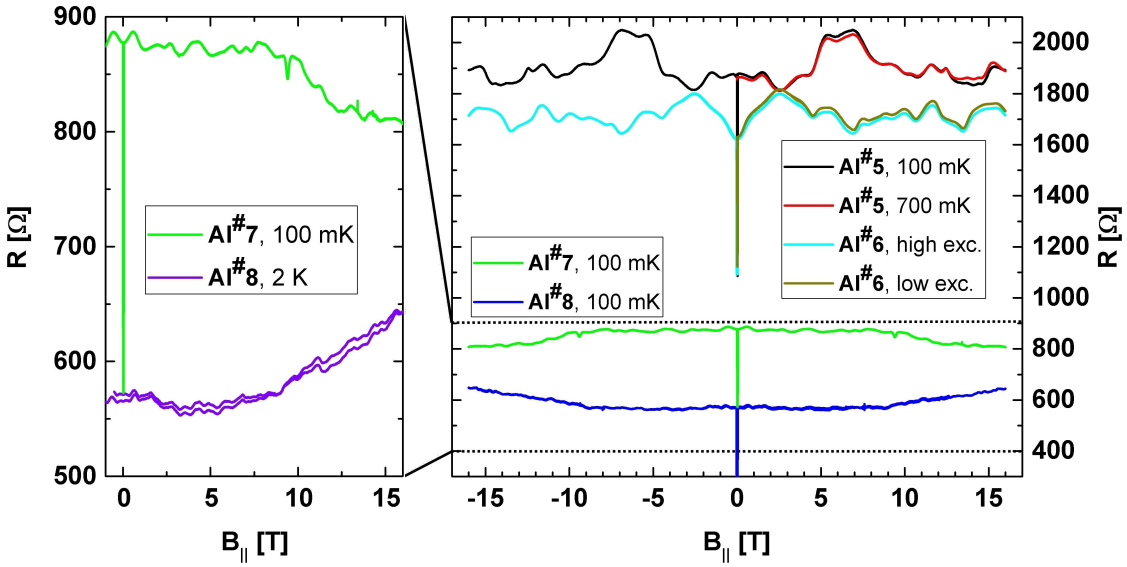

Figure 15.1: Resistance as a function of a magnetic field parallel to the wire axis comparing different samples with Al contacts.

Figure 15.1 shows the resistance as a function of a magnetic field along the wire axis for samples with Al contacts. Compared to the positive magnetoresistance for transverse magnetic fields, the resistance is rather constant for a longitudinal mag-

netic field. Similar to the transverse sweeps, a sharp feature is observed at small fields and very low temperatures. The resistance drop at zero field is attributed to superconductivity in the Al contacts. Reproducible fluctuations being symmetric for reversed field direction are recorded as well.

In Fig. 15.2, samples with Ti contacts give similar curves in a longitudinal magnetic field. Solely for all samples with Ti contacts, one contact is at the top end of the NW, possibly contacting the growth seed. The feature at small fields below 0.3 T is attributed to superconductivity in the metallic droplet and the Ti contacts. The fluctuations observed for higher fields are symmetric and look more regular from the first sight compared to the fluctuations in samples with Al contacts. At the end of this chapter, the periodicity of the fluctuations is compared to the outcome of a transport model which is explained below.

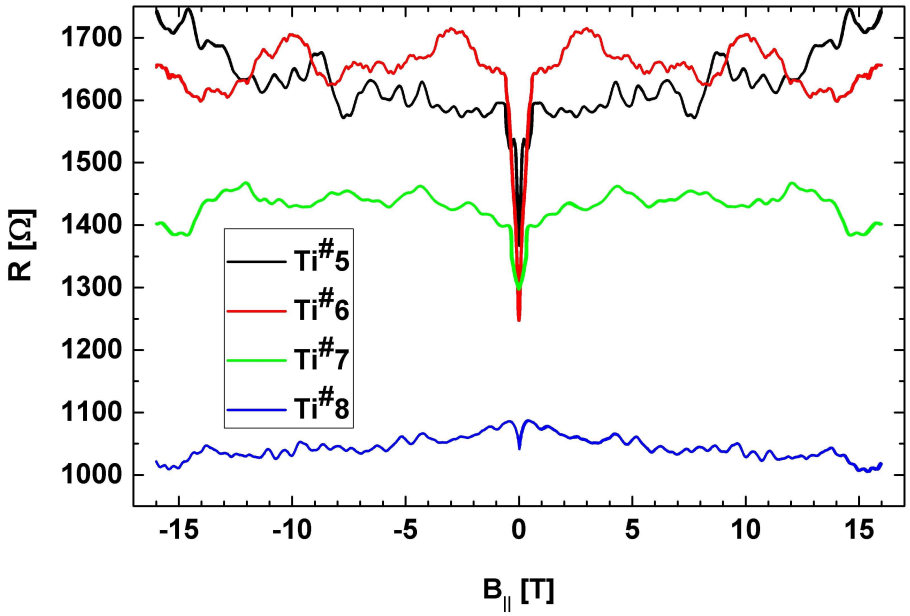

Figure 15.2: Resistance for a magnetic field parallel to the wire axis comparing different samples with Ti contacts measured at about 100 mK.

To model the coherent transport in topological insulator (TI) NWs, we consider a three-dimensional TI in the half-space of a Cartesian coordinate system (x, y, z). The TI is facing a trivial insulator at $z = 0$. The band order inversion for the topological phase is reversed close to the interface of the trivial insulator, creating gapless surface states.[97, 3, 11] Assuming the Fermi-level is inside a sufficiently large energy gap for bulk charge carriers, meaning for an ideal TI at low temperatures, charge transport is carried by the topological surface states only and any bulk con-

tribution can be neglected. The dispersion relation of the states, allowing a charge flow, is linear and has the same dimensionality as the two-dimensional surface of the three-dimensional TI.

$$E(\vec{k}) \propto \sqrt{{k_x}^2 + {k_y}^2}\ ,\ k_z = 0. \tag{15.1}$$

The electrons can be described by the Dirac-equation and are the massless Fermion analogue in condensed matter physics. If periodic boundary conditions are introduced into this system by folding the y-axis of the two-dimensional surface state in z-direction to a closed loop with a perimeter length L smaller than the phase-coherence length, then the wave function must fulfill the condition:

$$\Psi(x, y) = \Psi(x, y + L) \cdot e^{i\phi}, \tag{15.2}$$

where y is now a periodic coordinate. This description holds for example for three-dimensional TI NWs of appropriate size.[9, 98] The phase gain ϕ for a full rotation around the closed loop can have different reasons. To keep the model simple, only two components are considered in the beginning. First is the Berry-phase π,[99] related to the fact that topological surface states show high spin-momentum coupling. For systems with spin-momentum locking, the rotation of 2π, equal to a closed loop trajectory, creates an effective phase shift of π because a spin $\frac{1}{2}$ needs to be rotated by 4π to get back to the initial state.[100] The second one is the Aharonov-Bohm phase. A wave function with a closed loop trajectory enclosing an area $\vec{A}$ penetrated by a homogeneous magnetic flux density $\vec{B}$ gains a phase [101, 102]

$$\phi_{AB} = 2\pi\frac{\Phi}{\Phi_0} \text{ with } \Phi_0 = \frac{h}{e} \text{ and } \Phi = \vec{B} \cdot \vec{A}. \tag{15.3}$$

With $\Psi(x, y) = A(x)e^{ik_y y}$, we get discrete values for k_y.

$$k_y = \left(n + \frac{1}{2} - \frac{\Phi}{\Phi_0}\right)\frac{2\pi}{L} \text{ with } n \in \mathbb{Z}. \tag{15.4}$$

Similar to a spatial constriction, the periodic boundary condition reduces the continuous two-dimensional dispersion relation to hyperbolic quasi-one-dimensional subbands in k_x-direction. Figure 15.3 shows both, the two-dimensional dispersion relations with the boundary condition visualized as planes cutting the conical function, and the effectively one-dimensional hyperbolic dispersion relations. Without magnetic flux, the Berry-phase opens a gap at the charge neutrality point. An increasing magnetic flux lifts the degeneracy of counter propagating states. For $\Phi = \Phi_0/2$, the gap is closed by a purely linear mode. The same conditions as without flux are established periodically for a magnetic flux equal to a multiple of Φ_0.

Our model assumes one tubular surface state so far. For the case of a hollow three-dimensional TI shell, conductive states are predicted at the two interfaces. The inner one faces the CdTe core and the outer one the outside.

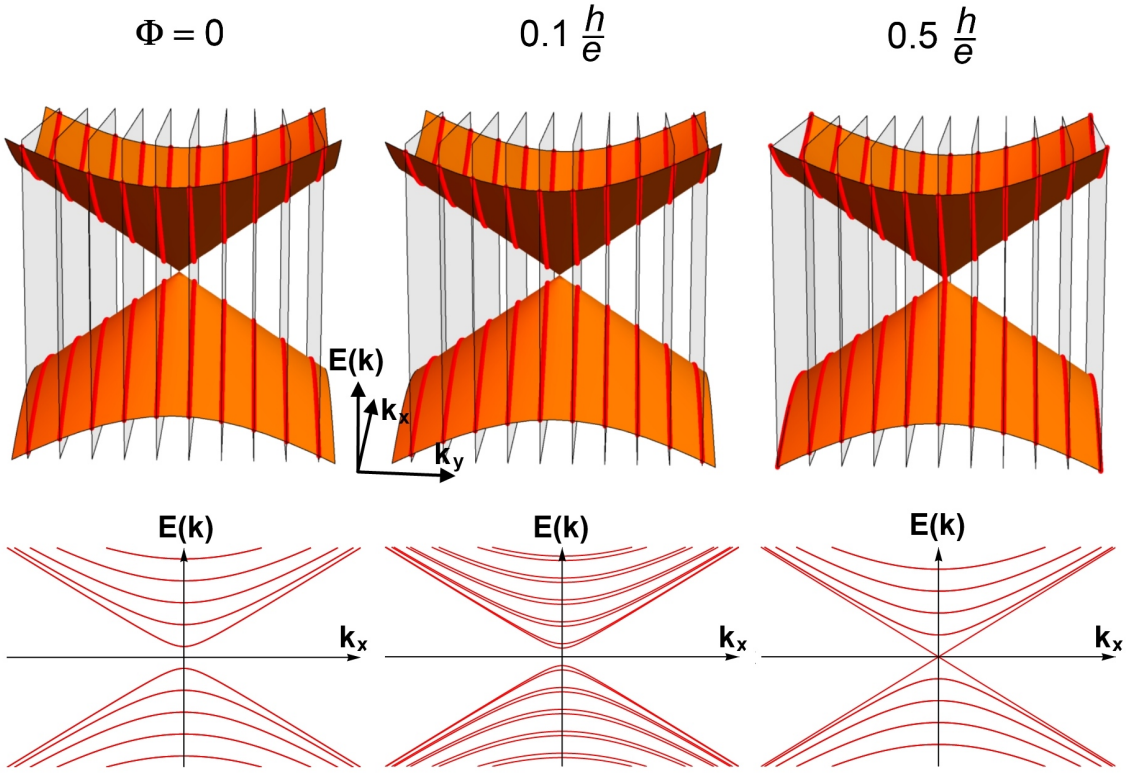

Figure 15.3: Two-dimensional Dirac-dispersion with periodic boundary conditions visualized as planes cutting the cone at different positions can effectively be described as the hyperbolic one-dimensional modes (bottom panel).

The density of states DOS can be expressed as

$$\mathrm{DOS} \propto \left(\frac{dE}{dk}\right)^{-1} \tag{15.5}$$

and is plotted in Fig. 15.4 as a function of energy for the case of quasi-one-dimensional sub-bands with dispersion relations described by hyperbolic cone-sections and linear or quadratic functions. For simplicity, the evolution of the DOS for a magnetic flux enclosed in the cross-section of the conductive tube is calculated for parabolic sub-bands only. This model already captures prominent effects for hyperbolic or linear dispersion relations.

The model describes coherent angular momentum states along the short perimeter. In the following, a diffusive transport regime is assumed to model the charge transport when an electric field is applied along the long axis of the NW. The resistivity in the diffusive transport regime is dependent on the charge carrier density n.

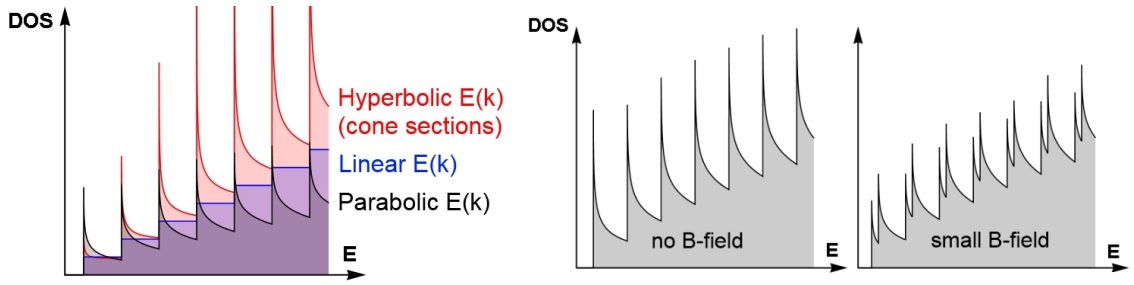

Figure 15.4: DOS for different dispersion relations in one-dimensional systems and splitting of DOS for counter-propagating carriers, when a magnetic field is applied parallel to the tubular NW.

For very low temperatures one can write

$$n \approx \int_0^{E_F} \mathrm{DOS}(E)\, dE. \tag{15.6}$$

Assuming the charge carrier mobility to be independent of the Fermi-level E_F, the resistivity can be expressed as $\rho \propto n^{-1}$ and is plotted in Fig. 15.5.

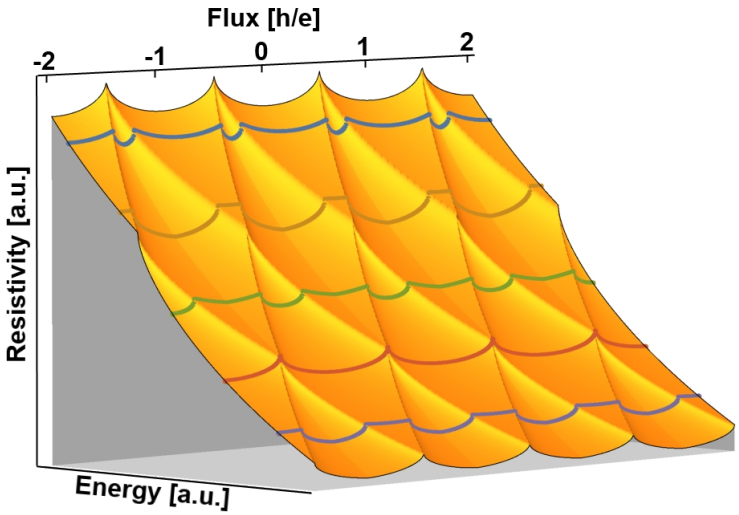

Figure 15.5: Periodic oscillations in resistivity as a function of magnetic flux.

For different positions of the Fermi-level, or experimentally for different gate voltages, an oscillating resistivity is obtained for changing magnetic flux. The oscillations are highlighted by the differently colored curves in the modeled resistivity in Fig. 15.5. Comparing the oscillations of the model to measurements, which are plotted for one sample in Fig. 15.6, we find a mostly random fluctuation of resistance. For some small intervals in gate voltage a rather flux periodic signal can be

found. The overall variation seems chaotic and points to UCFs. The low resistance feature observed at small magnetic fields, which is caused by superconductivity in the growth seed, is independent of gate voltage. Its dependence on magnetic field is discussed in the next chapter.

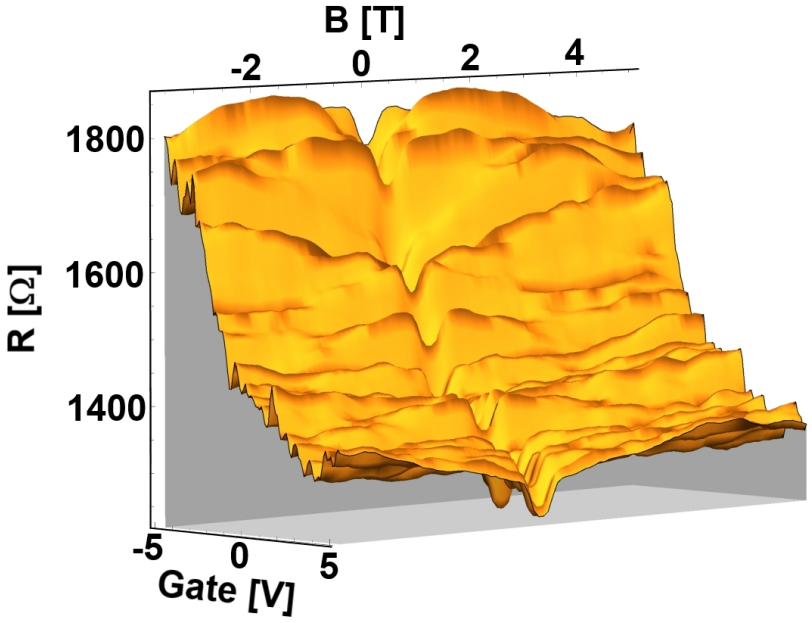

Figure 15.6: Gate voltage dependent resistance of Ti$^{\#}$7 changing the magnetic field along the wire axis shows random fluctuations.

The mean distance ΔB of resistance minima in magnetic field sweeps at zero gate voltage is analyzed in the following. If the interference of trajectories probes the sample geometry and not a random distribution of scattering sites, then the mean period of the fluctuation is linked to the sample size. Figure 15.7 compares transport results with the sample width. The mean period is obtained by a linear fit of the resistance minima positions (in magnetic field sweeps) versus an increasing integer number. Assuming either a circular or a triangular cross-section for the NWs, an effective width is calculated from the mean period. For three of the samples shown here, transport gives a much smaller width compared to the SEM image, but for one sample (Ti$^{\#}$6) it is vice versa. Therefore, we find no direct correlation of sample size and transport measurement. It is also not possible to explain the periodicity by two tubular states, as expected for a bulk-like HgTe shell. The findings suggest that the contribution of scattering sites to the phase sensitive charge transport can not be neglected. The model derived does not include many of the effects, that may occur additionally. A Zeeman-term possibly contributes to the energy of the sub-

bands when an external magnetic field is applied.[103] Another possible effect is the Aharonov-Casher phase gain for fermions with a magnetic moment traveling in an electrostatic field, which would lead to gate dependent conductance fluctuations.[104] So far, we are not able to explain the fluctuations in all samples with the same simple model.

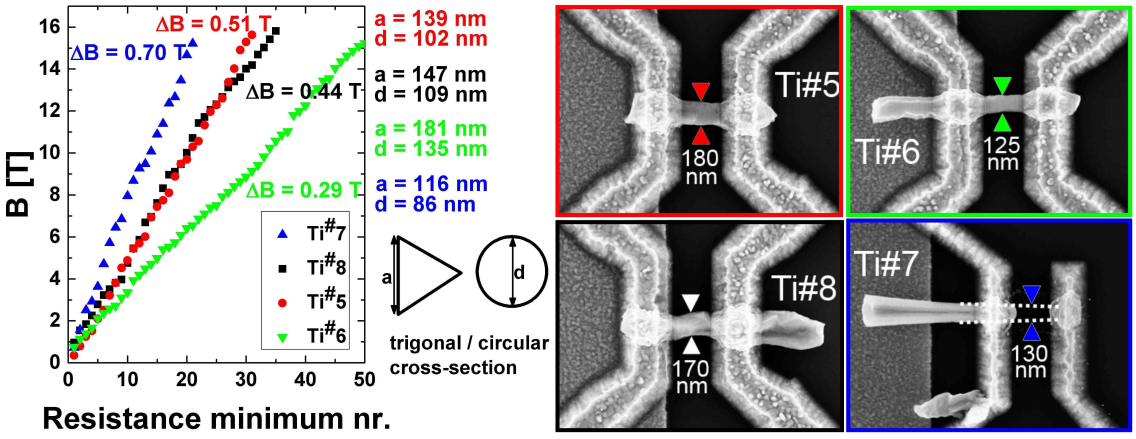

Figure 15.7: Comparing the mean period for the random oscillations with the size of different samples shows no clear correlation.

The comparison of experiment and model shows, that electron trajectories in the HgTe-NWs are defined not only by the geometry of the sample, but a random distribution of scattering sites. Thus, elastic backscattering suppresses the formation of coherent angular momentum states in our samples. Crystal defects and surface decoration with polar residuals can act as scattering sites. The idea is to protect the surface state of HgTe with an in-situ cap. A further optimization of the HgTe shell growth, for example by the use of CdTe NW arrays with equal spacing, should decrease the defect density and thereby increase the mean free path of charges. Some samples are contacted in a geometry with four independent AuGe leads touching the NW, but they are not reproducibly working so far. One of these showed the most regular oscillation in a longitudinal magnetic field during a pre-characterization. The NW was destroyed by electric discharge before being fully characterized. For further investigation of phase coherent transport in HgTe-NWs, the true 4-terminal geometry, but with Ti or Al contacts is expected to show better results. The pseudo 4-terminal geometry used primarily in this work is sensitive to defects introduced by the contact area cleaning, namely the physical etching of the NW before in-situ metalization.

16 The metallic growth seed as a superconducting contact

In the previous two chapters, we have observed a lower resistance for magnetic fields below 0.3 T for the samples contacted with Ti. This is only observed, if one contact lies on the top end of the NW. Usually, the droplet seeding the growth is still present at the NW's tip, when the samples are cooled for transport measurements. The droplet is possibly an alloy of all the materials supplied during growth (Au, Ga, Zn, Cd, Hg and Te). Most of these are elemental superconductors.[105, 106] Pure Au shows no superconductivity, but alloys formed between Au and the other elements are superconductors.[107, 108] Assuming the alloy present at the NW tips to be superconducting, the observation of lower resistance up to a critical field can be explained. Superconductivity is a low temperature effect of vanishing resistance, characterized by a breakdown at a critical magnetic field. Therefore, the measurements are performed at base temperature below 100 mK. Since the droplet might rip off during NW manipulation, it is not surprising, that we do not observe this effect for all the samples with a contact at the top end of the NW.

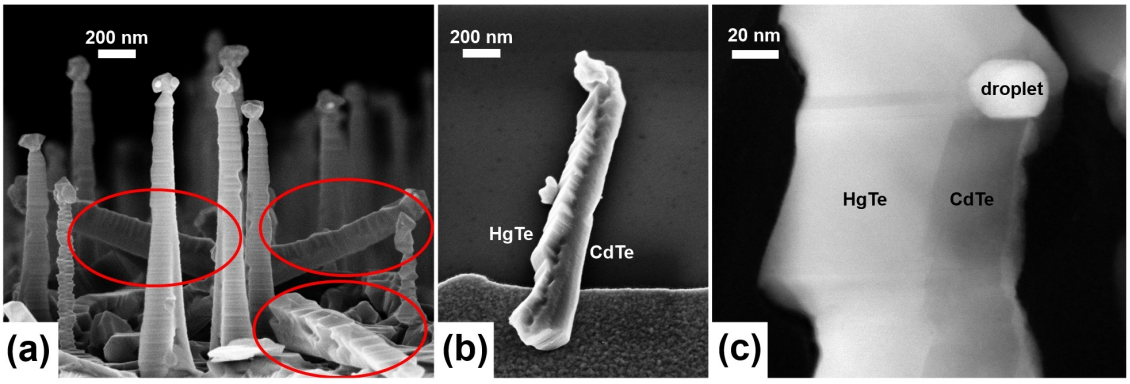

Figure 16.1: NWs grown tilted by 19° to the substrate are depicted in (a). These NWs are overgrown with HgTe mainly on one side as in (b) and (c). The STEM image in (c) shows the cross-section of such a hybrid structure.

To further analyze the properties of the superconducting (SC) island by charge transport, a special sample geometry is helpful. For NWs grown tilted by 19° to the substrate, HgTe overgrowth occurs mainly on one side of the NW. With the geometry shown in Fig. 16.1, the droplet is partially covered by HgTe. If furthermore the side overgrown with HgTe is facing the substrate before applying the contacts, we get the special situation depicted in Fig. 16.2. The bare droplet is contacted by the Ti lead. At least a part of the current flows through the SC island into the HgTe, which is contacted at the other end.

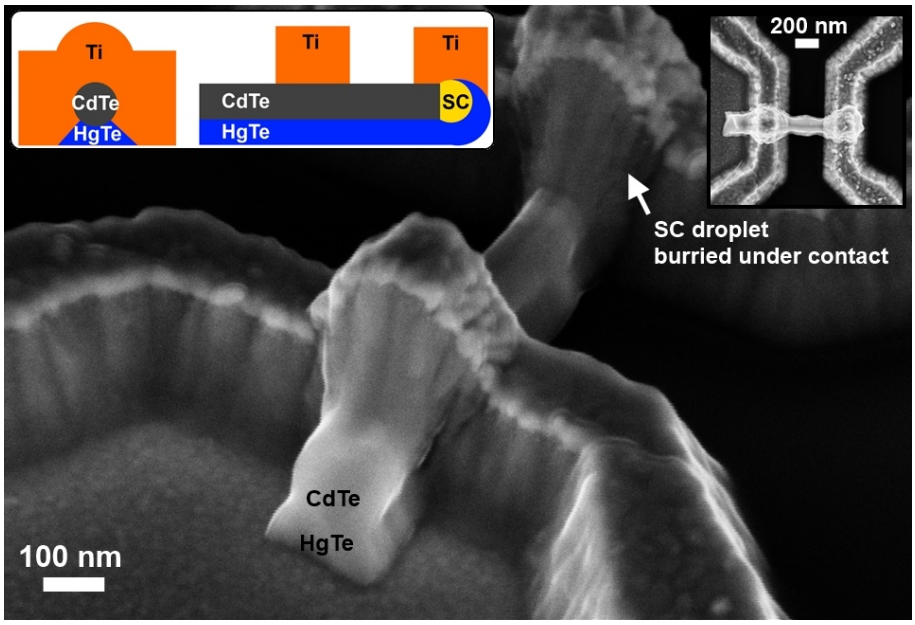

Figure 16.2: For Ti#1 the side overgrown with HgTe is facing the substrate. One metallic contact is expected to lie on the bare droplet, schematically depicted in the left inset. The right inset shows the top view of the sample.

We measure the differential resistance of the junction as a function of DC current as shown in Fig. 16.3 (a). For zero magnetic field, we observe two plateaus of the differential resistance, separated by sharp peaks. The low resistive state is referred to as the superconducting state, while the saturating differential resistance at higher currents is called the normal state.

Superconductivity breaks down at a critical current density as well as at a critical magnetic field. For increasing magnetic field the energy scale of the SC state shrinks and furthermore the overall resistance is increasing, while the sharp peaks are smeared out and then vanish. Intuitively one can draw the conclusion, that the

sharp peaks mark the critical current in the SC island. Assuming a cross-section area of $50\times50\,\mathrm{nm}^2$, a critical current of 267 nA equals $\sim 10^4\,\mathrm{A/cm}^2$. Comparing this value to previous results,[109, 110] we find it at the lower boundary of critical current densities observed in small structures. Most likely the critical current in the metallic droplet is larger up to a factor of 10 to 100. That the peaks have a different reason, is supported by the following observation. At fixed, high sample current, e.g. 500 nA, we observe an increase in resistance for an increasing magnetic field in Fig. 16.3 (b). This increase is not continuously, but rather instantly at the critical field of 0.3 T, what is not expected, when the high current would suppress the superconductivity in the droplet. At about 0.4 T we measure the saturated resistance, where the SC island is definitely a normal metal. Since a breakdown of superconductivity in the SC island can be observed for low and high current, it explains the magnetic field dependent resistance, but not the excitation dependent features at zero field.

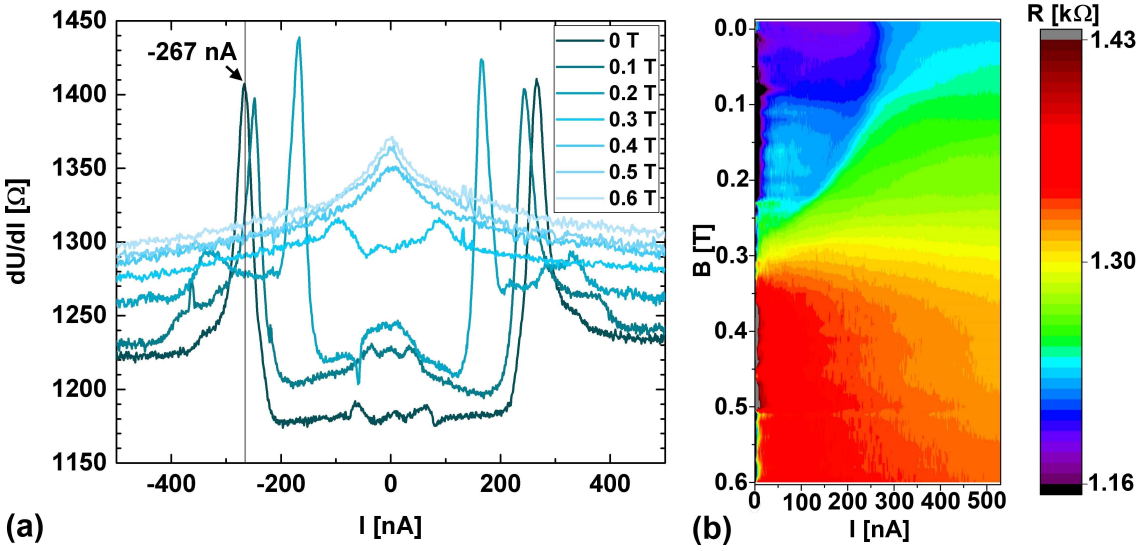

Figure 16.3: The plots show (a) the differential resistance and (b) the resistance of Ti$^{\#}$1 as a function of DC sample current for various magnetic fields.

To understand the features at low field, we start the treatise with a brief review on superconductivity. The Bardeen-Cooper-Schrieffer (BCS) theory explains superconductivity in metals.[111, 112] In a superconductor, electrons are paired to Cooper-pairs. An attractive electron-electron interaction is achieved via phonons. The pairs are strongly correlated, and can be viewed as one macroscopic quantum state. For conventional s-wave superconductors, paired electrons have opposite momentum and spin. As the spin of the pairs is 0 and not $\pm\frac{1}{2}$, Cooper-pairs can be described as a Bose-Einstein-condensate. Opposite to the Fermi-Dirac statistics, where the Pauli-principle forbids multiply occupied quantum states, Bosons can be in the same

ground state. The energy of the BCS ground state is given by the Fermi-level. The pairing potential is small and superconductivity can be observed only at low temperature. Most of the electrons remain unpaired and only those with an energy close to the Fermi-level condensate to the bosonic quasi-particles. The density of states (DOS) of the unpaired states is altered as well. The interaction by phonons opens a small energy gap for unpaired electrons. The states, which are present at these energies in the normal state, are pushed to the edges of the energy gap, leading to pronounced maxima in DOS. The presence of a superconducting energy gap, where only paired electrons are allowed and the formation of maxima in DOS at the gap edges can give rise to features in excitation dependent differential resistance, which is explained in the following.

The theory developed by Blonder, Tinkham and Klapwijk (BTK) allows to model normal-metal/superconductor (N/S) junctions.[113] In this model, the probability for an incident electron to be reflected at the interface is $\frac{Z^2}{1+Z^2}$. The dimensionless barrier strength Z allows to investigate contacts with transparencies ranging from metallic to tunneling regime. The interface barrier strength is modeled as a Dirac delta potential. In the limit of low transparency, the differential conductance probes the DOS of unpaired states in the superconductor. In this case, the dips in differential resistance occur at the edge of the superconducting energy gap, as shown in Fig. 16.4 (b).

An additional contribution to transmission and reflection of electrons comes into account for transparent contacts. Unpaired electrons, approaching the interface from the normal side with an energy inside the superconducting gap, are not allowed to enter the superconductor. The BTK theory formulates the conversion of a quasi-particle current into a supercurrent. In terms of the quasi-particle states defined by the Bogoliubov-de Gennes (BdG) equations, the incident electron is reflected as a hole, a phenomenon called Andreev reflection.[114] This process transmits twice the charge of an electron, a Cooper-pair, into the superconductor.

The BTK formalism allows to explain the plateau of low differential resistance for small excitation in Fig. 16.4 (a) by Andreev reflection. If the voltage drop across the junction is in the order of the superconducting gap, a saturation of differential resistance at a higher level is expected, as the probability for Andreev reflection decays very fast outside the superconducting gap. Additionally, we measure sharp peaks in the differential resistance, when switching from one plateau level to the other. This unusual feature is not expected by BTK and we try to understand our measurements by a model based on the same formalism, but with additional degrees of freedom.

(a) BTK with transparent interface.

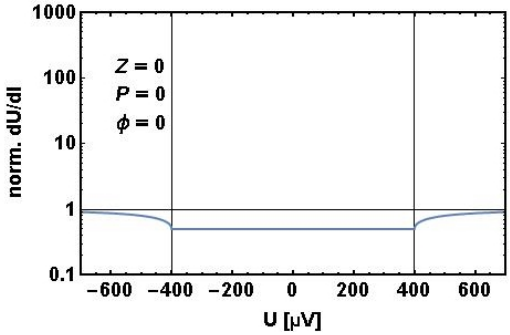

(b) BTK with finite barrier strength Z.

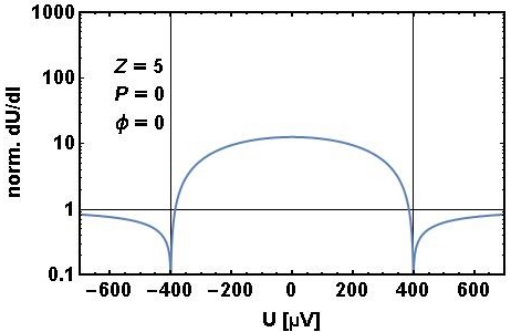

(c) Weakly superconducting interface.

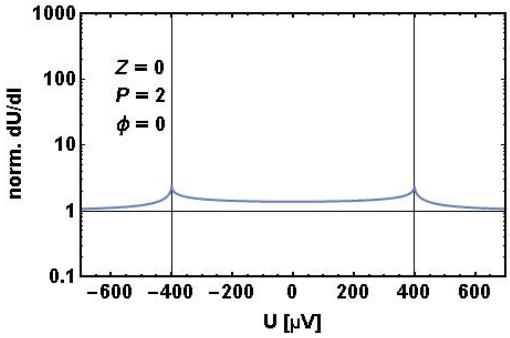

(d) Same as (c), but with finite barrier.

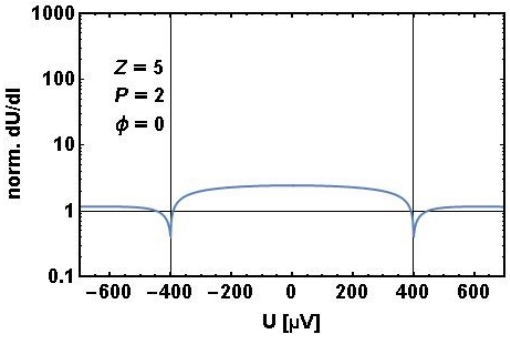

(e) Interface with nodal order parameter.

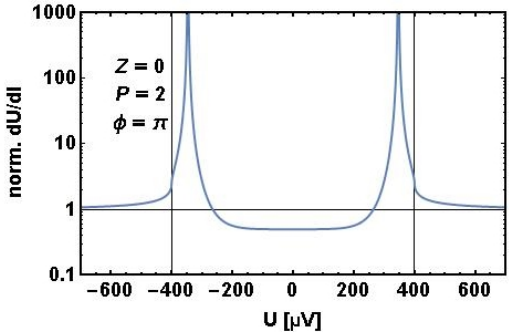

(f) Same as (e), but with finite barrier.

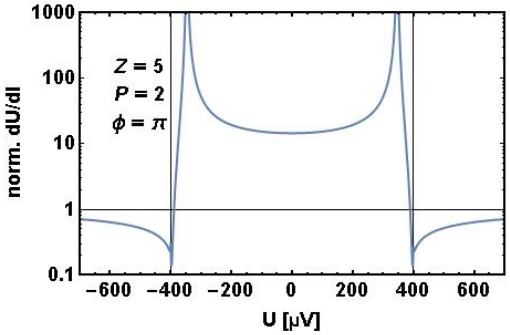

Figure 16.4: Normalized differential resistance curves calculated for T=0 K and Δ=400 µV. The horizontal lines give the normal state resistance of the junction. The superconducting gap Δ assumed for simulation is depicted by vertical lines in the plots.[115]

To derive a model, we follow the considerations of Catapano *et al.* [115] for a one-dimensional N/S junction described by the BdG equations

$$[\mathcal{H} + V(x)]\Psi(x) = E\Psi(x), \tag{16.1}$$

where $\Psi(x) = (e_\uparrow(x), e_\downarrow(x), h_\uparrow(x), h_\downarrow(x))^T$ is the quasi-particle state having excitation energy E above the Fermi-level E_F. The Hamiltonian

$$\mathcal{H} = \begin{pmatrix} \hat{H}_0 & \Delta(x)i\hat{\sigma}_y \\ -\Delta^*(x)i\hat{\sigma}_y & -\hat{H}_0^* \end{pmatrix}, \text{ with } \hat{H}_0 = \left[-\frac{\hbar^2\partial_x^2}{2m} - E_F\right]\hat{\mathbb{I}} \tag{16.2}$$

is used to describe the bulk properties of the hybrid structure. $\hat{\mathbb{I}}$ represents the identity operator in the spin space and $\hat{\sigma}_y$ is the Pauli matrix. The effective mass m and E_F are assumed to be constant over the junction. The superconducting order parameter $\Delta(x)$ is described by a step function. To model unconventional effects, the potential barrier $V(x)$ at the interface includes a pairing term.

$$V(x) = \begin{pmatrix} U_0\hat{\mathbb{I}} & U_1 i\hat{\sigma}_y e^{i\phi} \\ -U_1^* i\hat{\sigma}_y e^{-i\phi} & -U_0\hat{\mathbb{I}} \end{pmatrix}\delta(x), \tag{16.3}$$

where U_0 is the standard BTK barrier strength, while U_1 describes the pairing at the interface, similar to a superconducting order parameter Δ. This can be used to describe induced superconductivity. The variable ϕ allows to tune the phase difference between the interface and bulk order parameter. The free energy of the system is minimized, when the Josephson current $I_J(\phi) \propto \sin(\phi)$ vanishes, i.e. for $\phi = 0$, or π. For $\phi = \pi$, the superconducting order changes sign close to the interface, which is an unconventional situation we call nodal order parameter.

Catapano *et al.* chose the simplest particle-hole mixing boundary conditions allowed by the BdG formulation. $Z \propto U_0$ is the usual BTK barrier parameter. The pairing at the interface has the strength $P \propto U_1$. In their contribution, the authors give expressions for the scattering coefficients in such N/S junctions and furthermore for the differential conductance.[115] The differential resistance is plotted for different values of Z, P and ϕ in Fig. 16.4. The curves in (a) and (b) reproduce the BTK picture, without superconducting interface. The curves in (d) and (f) are not very reliable, as they assume a potential barrier to be present, but a strong coupling at the interface. The curves in (c) and (e) represent N/S junctions without barrier, where the coupling of both materials manifests as a weakly superconducting interface. Only the case depicted in (e) shows the low resistive plateau, then sharp peaks before reaching normal state resistance. In this case the superconducting order is modeled to have a node close to the interface. The outcome of this model looks similar to the measurement in Figs. 16.3 and 16.5.

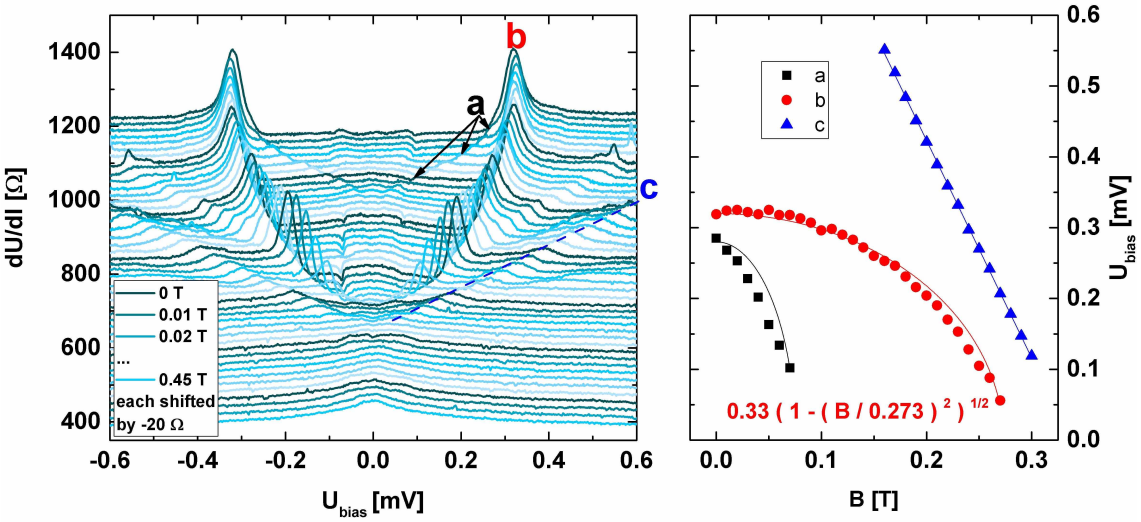

Figure 16.5: In the left the differential resistance of Ti#1 as a function of DC bias is plotted for various magnetic fields. Right hand, the position of prominent features is shown in dependence of the magnetic field together with fit functions described in the text.

We have seen, that DC bias dependent differential resistance measurements can probe the spectral Andreev probability or the DOS. The measurements in Fig. 16.5 show several features. Three prominent features are labeled with a, b and c. The peak b can be explained by the nodal order parameter model. The features a and c are not explained so far. As they show some dependence on magnetic field, characterized by a breakdown at a critical field, they are most likely associated with superconductivity as well. For unknown reason, the feature c shows a linear dependence on magnetic field (blue line). For the peak b, the formula for the magnetic field dependence of the gap [116]

$$\frac{\Delta(B)}{\Delta(0)} = \left(1 - \left(\frac{B}{B_{critical}}\right)^2\right)^{1/2} \tag{16.4}$$

fits well to the data (red line). The feature a shows a different magnetic field dependence, well described neither by a linear fit (not shown), nor by Eq. 16.4 (black line).

In this work, the focus is on the peak b, possibly related to the gap edge. For now, we assume the nodal order parameter model to be valid, which is discussed again later. We simulate the sample by adding serial and parallel resistors. This gives rise to the fact, that only some part of the current flows through the SC island into the HgTe. This allows to extract rough estimations for the interface

transparency and the size of the superconducting gap. Best fits are obtained for an interface transmission probability between 0.9 and 1.0, and 0.3-0.4 meV for the energy gap of the SC island. The observation of a hybrid HgTe-superconductor sample with high interface transparency is already a great success. As the hybrid structure was grown fully in situ, the highly transparent interface is not surprising. The energy gap of the SC island is twice larger than the value for Al, a superconducting contact material primarily used in this work. The observation of superconductivity up to a critical field of 0.3 T is a characteristic of the SC island at the tip of each wire. Since the critical magnetic field of the SC island is much larger compared to the one of the superconducting leads based on Ti or Al, we can exclude, that superconductivity in the contact-leads is the origin of the effects discussed in this chapter.

The possibility to fit the behavior with a nodal order parameter gives insight to the unconventional proximity effect in our HgTe-NW/superconductor junctions. Together with the discovery of a self-organized SC island at the top of each wire, the observation of an unconventional peak in the differential resistance might either be caused by unconventional superconductivity in the droplet itself, or by the proximitized HgTe. Before we interpret the nodal order parameter model, the results are compared to superconductor/HgTe-NW/superconductor junctions with Al-based contacts in the next chapter.

17 Charge transport with two superconducting contacts

To exclude unconventional features – as seen in the previous chapter – arising from the contact material, we use Al, a well known (type-I and s-wave) superconductor.[117] The I-V curves and basic properties of such junctions are discussed in the beginning of this chapter. Then we come back to the topic of differential resistance peaks.

In order to characterize superconductivity in the Al contacts, temperature and magnetic field dependent measurements of several samples are analyzed. The average critical temperature is $T_c = (0.95 \pm 0.10)\,\mathrm{K}$. By the BCS relation $\Delta = 1.764 \cdot k_B \cdot T_c$,[119] a value of $2\Delta = (0.29 \pm 0.02)\,\mathrm{meV}$ can be calculated, which is about 78% of the one of single-crystal bulk material. Most likely, the reduced gap energy is caused by lithographic processing. The critical magnetic field is found to be orientation dependent, being 21 mT for a magnetic field parallel to the wire and 13 mT for an out-of-plane magnetic field.

The whole junction shows very low resistance for low excitation. The I-V curves in Fig. 17.1 are non-linear, with a low resistive region up to a critical current. The differential resistance of the junctions at zero bias and no magnetic field is about one order of magnitude lower, than the normal state resistance. This can be seen as a noise limited Josephson supercurrent, where high-frequency noise gives rise to a small voltage drop.[118] Figure 17.1 shows I-V curves with reversed sweep direction. As no significant hysteresis can be observed, we consider the junction to be overdamped.[119] Thus, the critical current observed is limited by noise in the experimental setup. A critical current of about 50 nA, which is read out at the position of maximum slope of the I-V curve, can be reported for the best device. To characterize our junctions, the critical current I_c, the normal state resistance R_n and the $I_c \cdot R_n$ product are listed in Tab. 17.1. The critical current is altered by applying a voltage to the back-gate. A gate-tunable supercurrent through semiconductor NWs was reported previously.[120]

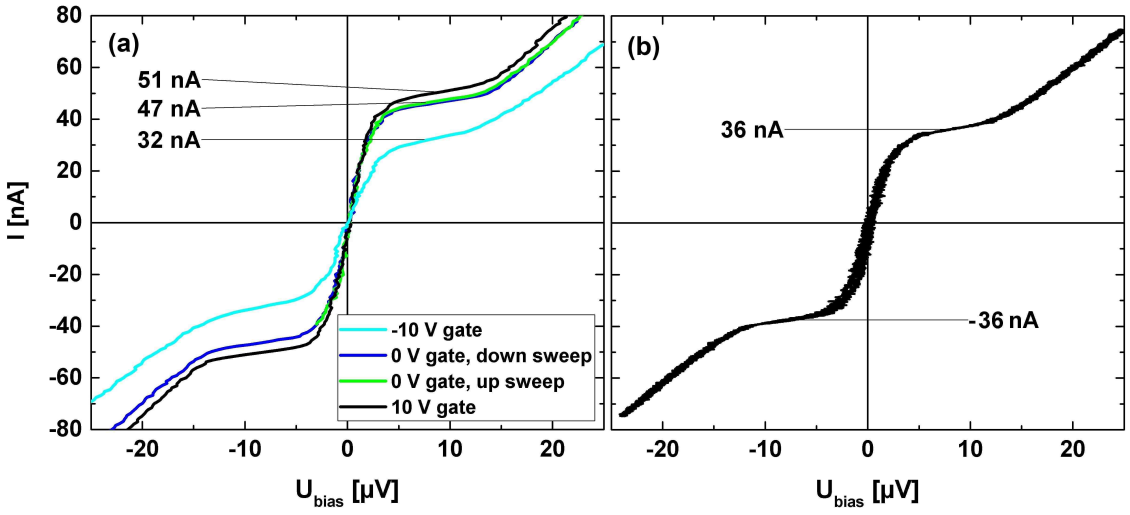

Figure 17.1: The I-V curves show a noise limited supercurrent of (a) Al$^{\#}$4 for different gate voltage and sweep direction and (b) Al$^{\#}$8 with many bidirectional repetitions of the measurement.

Dubos *et al.* carried out an extensive experimental and theoretical study of the critical Josephson current in S/N/S junctions.[121] Supercurrents in S/N/S structures are due to Andreev bound states. The pairing interaction which leads to an energy gap of Δ around the Fermi-level E_F in the superconductor is absent in the normal material and the normal electrons enter the superconductors via Andreev reflection. In a disordered system, the time-reversed states involved are coherent over some distance dependent on phase coherence length and diffusion constant. Another way to express induced superconductivity is that Cooper-pairs diffuse into the normal region. In this picture, the critical induced supercurrent in the normal region is estimated to be

$$I_c = \frac{10.82\ E_{Th}}{e\ R_n} \tag{17.1}$$

for a junction with length larger than the superconducting coherence length, where E_{Th} is the Thouless energy.[122] The distinction between long and short junction can be made by comparing E_{Th} to Δ. The $I_c \cdot R_n$ products are in the range of 9-24 µV, much smaller than the value determined from the gap $\Delta/e = 145\,\mu\text{V}$. Thus, all samples are in the long junction limit.

Figure 17.2 shows the breakdown of induced superconductivity with applied magnetic field. For a magnetic field parallel to the NW, a critical value of 15 mT is measured. For out-of-plane orientation, the critical field is 12 mT. The dependence of critical current on magnetic field can be fitted by Eq. 16.4, thus $I_c(B) \propto \Delta(B)$. For the first time, a noise limited supercurrent through quasi-one-dimensional HgTe

Sample	Al#1	Al#2	Al#3	Al#4	Al#5	Al#6	Al#7	Al#8
I_c [nA]	7	14	18	47	8	8	18	37
R_n [kΩ]	1.39	0.99	0.77	0.51	1.80	1.62	0.88	0.57
$I_c \cdot R_n$ [μV]	9	14	14	24	15	13	16	21
I_{exc} [μA]	0.07	0.11	0.11	0.28	0.06	0.06	0.11	0.24

Table 17.1: Critical current I_c, normal state resistance R_n, their product $I_c \cdot R_n$ and a quantity called excess current I_{exc} are listed for all the samples discussed in this chapter.

is reported. This proves the high transparency of the contact interfaces and is a huge technological step in the realization of hybrid HgTe-NW/superconductor devices. For bulk-like samples based on the TI HgTe, a proximity induced supercurrent was reported earlier.[123, 124]

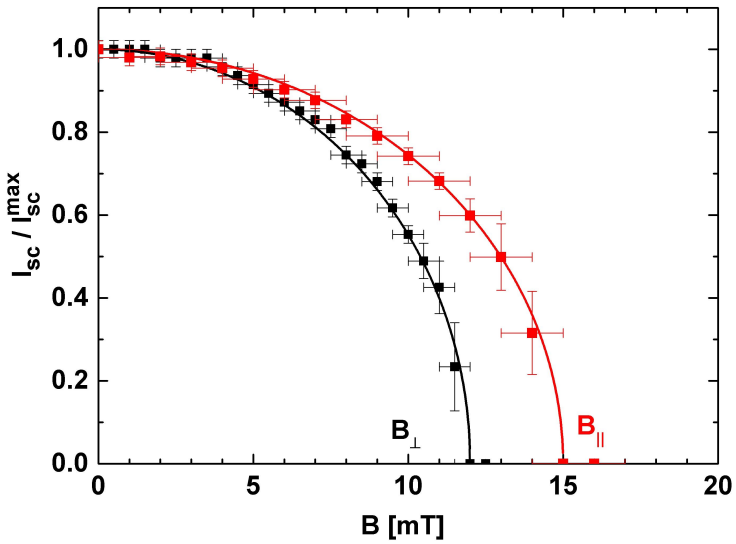

Figure 17.2: The dependence of critical current on magnetic field applied parallel (red symbols) and perpendicular (black symbols) to the NW. The lines show fits of Eq. 16.4.

Additional to induced superconductivity, the appearance of multiple Andreev reflection (MAR) leads to a further non-linearity in the I-V characteristic. A carrier, Andreev-reflected at one N/S interface, has the possibility to get reflected again by the other N/S interface, if it transverses the normal region coherently. The full-range I-V curves of the two samples with highest (noise limited) supercurrent are shown in Fig. 17.3. At zero magnetic field (red line), an excess current can be extracted

from the measurement by a linear fit for bias higher than $\frac{2\Delta}{e}$ and followed by extrapolation to zero bias (dashed blue line). The ohmic characteristic for a magnetic field larger than the critical field is shown for comparison (black line). The excess current I_{exc} is a consequence of the enhanced charge transport by MAR. The values of I_{exc} obtained for each junction are listed in Tab. 17.1.

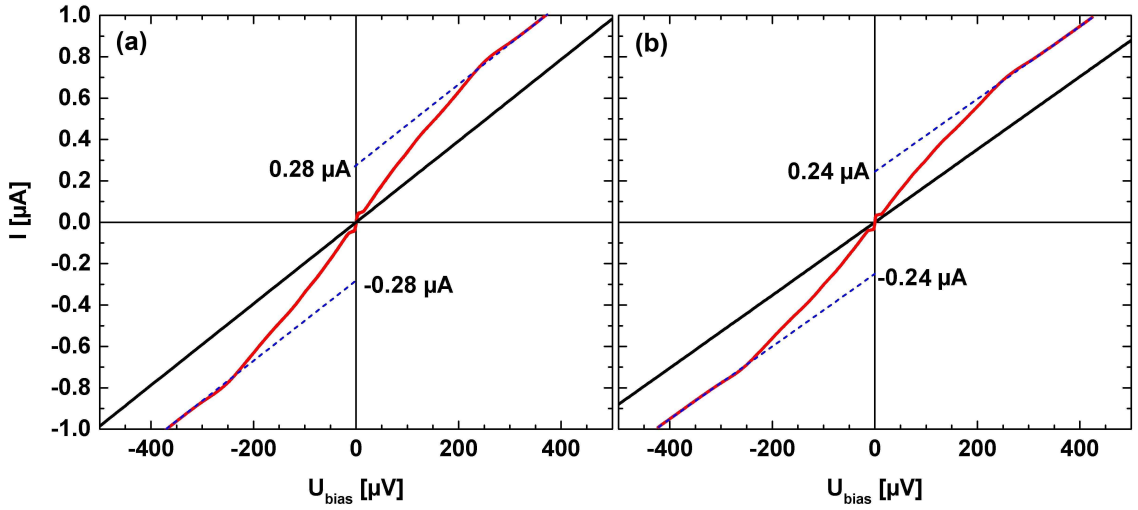

Figure 17.3: The full-range I-V curves of (a) Al$^{\#}$4 and (b) Al$^{\#}$8 show a distinct nonlinearity at zero magnetic field (red line) but an ohmic characteristic at a small magnetic field (black line). We can extract an excess current by linear fits to the I-V curve for $U_{\text{bias}} > 2\Delta$ (dashed blue line).

Directly related to the superconducting gap, the excess current is expected to follow the same magnetic field and temperature dependence.[125] The measured excess current for increasing magnetic field and temperature is shown in Fig. 17.4. For a magnetic field along the NW, some deviation from the model is observed. The reason for this is not known so far. As we are able to achieve excess currents up to 0.28 µA for the best device, we can state that MAR processes are present in our samples. In the previous chapter the probability of Andreev reflection was already linked to highly transparent N/S interfaces. It is therefore not surprising, that samples with high critical current show also high values for the excess current. Flensberg *et al.* calculated the I-V curves and excess currents on S/N/S junctions where the BTK barrier strength Z is varied numerically.[126] An analytical expression for the excess current in the framework of MAR was found by Niebler *et al.*[127] For the device with the highest excess current (Al$^{\#}$4) we get a value of $T = \frac{1}{1+Z^2} = 0.73$ for the transmission probability of each contact, assuming both contact transparencies to be equal.

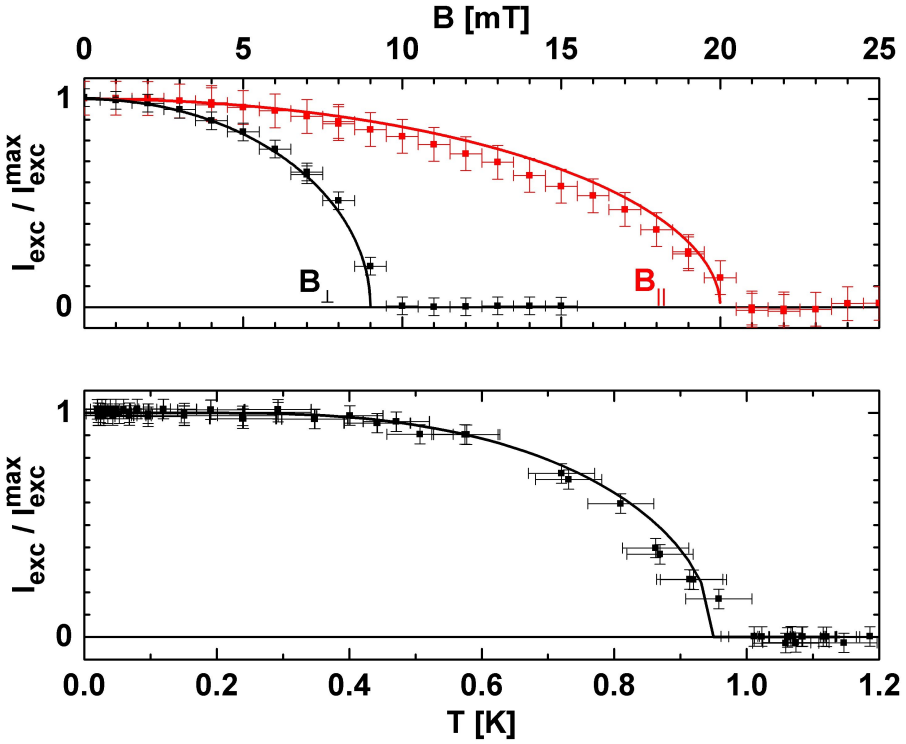

Figure 17.4: The measured excess current for increasing magnetic field and temperature is shown together with fits of the theoretical dependence of the energy gap of a conventional superconductor (Eq. 16.4).

In order to study the structure in the non-linearity of the I-V curves, the bias dependent differential resistance is measured as well. The sample with highest contact transparency shows the most pronounced features, as shown in Fig. 17.5. These occur as steps in resistance and peaks in differential resistance. A series of peaks at sub-multiples of the gap voltage $\frac{2\Delta}{n\,e}$, with $n = 2, 3, 4, ...$, and no peak but rather a dip at $\frac{2\Delta}{e}$ is expected from theory.[126, 128] We observe two deviations from this theory. First are the unconventional outermost peaks ($\frac{2\Delta}{e}$) instead of dips, fitting well to the position of the gap $2\Delta = 0.29\,\text{meV}$ derived from the average critical temperature. Second is the deviating separation of multiple orders. The peak at 2Δ is exactly at twice the voltage of Δ, but higher order peaks occur shifted with respect to the expected value. Despite these deviations, the observed features can be explained by the successive onset of MAR. Applying a magnetic field, the MAR features in Fig. 17.6 scale with the superconducting gap and are smeared out to a flat line at the critical magnetic field.

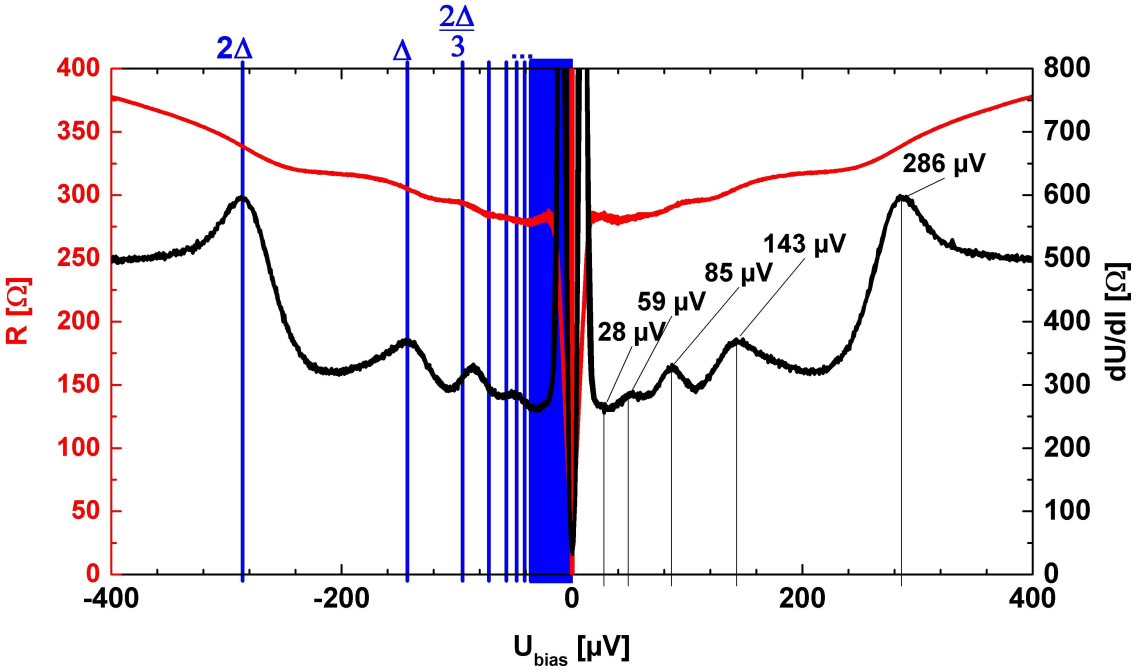

Figure 17.5: Resistance (red) and differential resistance (black) of Al#4 show a subgap structure. Assuming the outermost peak to be at $\frac{2\Delta}{e}$, the theoretical position for MAR is depicted for negative bias by the blue lines.

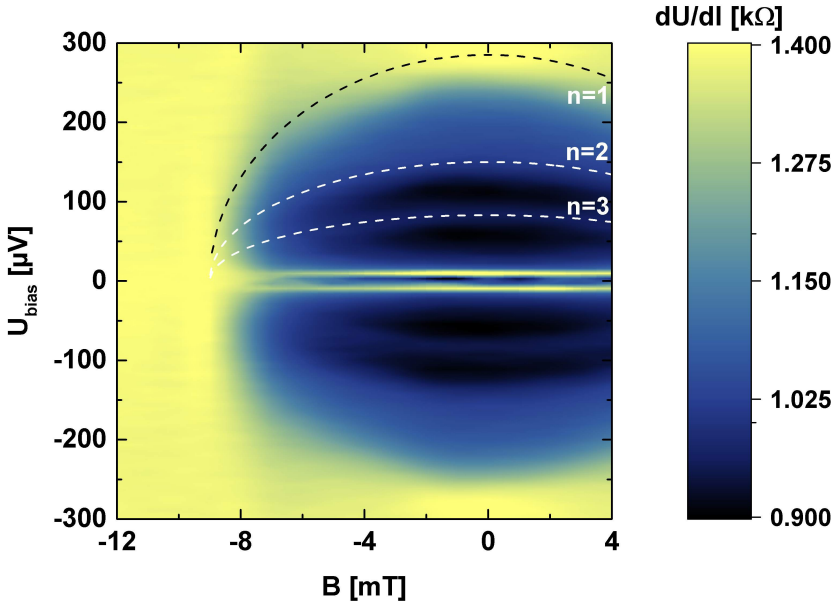

Figure 17.6: The plot shows the differential resistance of Al#1 with an out-of-plane magnetic field. The dashed lines trace the MAR peaks by Eq. 16.4.

The MAR peaks are reproduced for other samples, as can be seen from Fig. 17.7. For samples with high contact transparency, the peak at $\sim \frac{2\Delta}{e}$ can be observed. For lower transparency, the MAR features smear out and the outermost peaks in differential resistance are not observed. The peak at $\frac{2\Delta}{e}$ occurs at the bias voltage, when the opposite gap edges of the two superconducting leads are aligned. This observation can be explained by a blockade of Andreev reflection close to the gap edges. Such a blockade was already modeled for a single N/S interface in the previous chapter. In that model, a sign change of the superconducting order parameter leads to reduced Andreev reflection probability, if the Fermi-level of the normal side is aligned with the gap edge of the superconductor. The peaks at $\frac{2\Delta}{e}$ for Al/HgTe-NW/Al and $\frac{\Delta}{e}$ for HgTe-NW/SC island junctions have most likely the same origin.

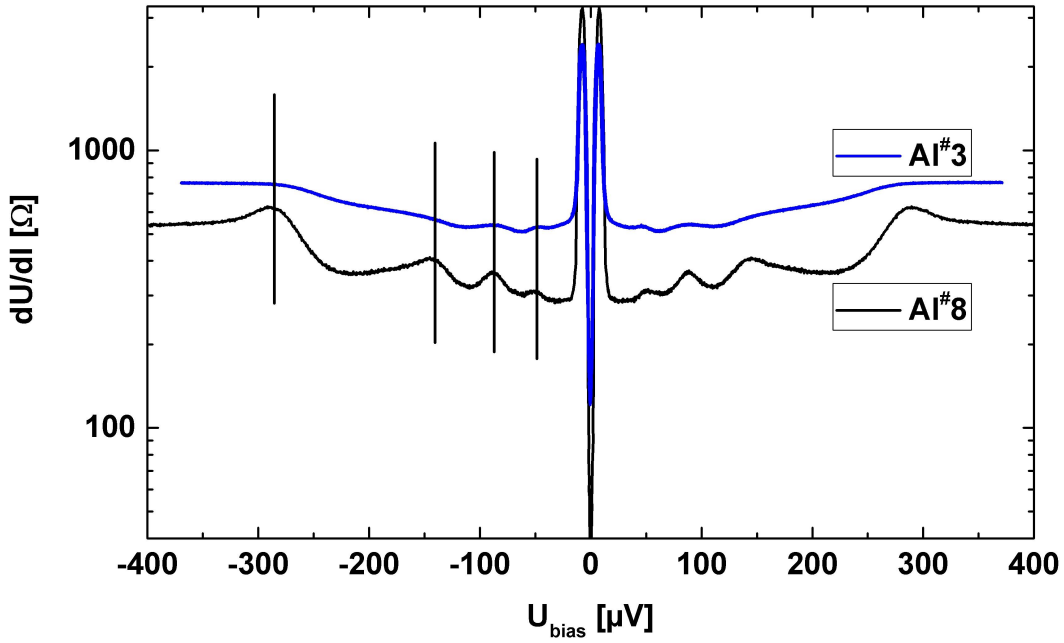

Figure 17.7: The bias dependent differential resistance of other samples with rather transparent contact interfaces, as for example Al$^{\#}$8 (black), reproduce the sub-gap structure of the first sample discussed. For samples with less transparency, as for example Al$^{\#}$3 (blue), the MAR features smear out, but remain visible, while the outermost peak can not be observed.

The model assumes the junctions to be in equilibrium, which is not the case when bias is applied. Non-equilibrium effects can alter the results. While we interpret the nodal order parameter model, we need to keep in mind, that it is only one possibility to explain the outermost peaks in differential resistance. Other explanations are not available at this point, but we can not exclude a different mechanism for our

observation. Furthermore, the model is purely one-dimensional. As the NWs are quasi-one-dimensional, with electrons moving around the core while travelling along the wire, the superconducting order parameter in our samples might be dependent on the angle under which the charges approach the interface to the superconductor. Keeping this in mind, it is clear, that a sign change in the order parameter at the interface does not necessarily mean, that the order parameter undergoes this sign change for all wave vectors $\vec{k}$.

Before we draw a conclusion, what might be the reason of the reduced Andreev reflection probability close to the gap edge, we have a look on experiments performed by other groups with different materials. For S/N/S junctions with an InAs 2DEG or NW as a link between the superconducting leads, very similar behavior has been observed.[129, 130, 131] Supercurrent, excess current and MAR features with peaks in differential resistance at $\frac{2\Delta}{n\,e}$, with $n = 1, 2, 3, ...$ are reported. The origin of the unconventional peak at $\frac{2\Delta}{e}$ is not explained. For the case of the 2DEG, highly transparent interfaces between superconducting and normal region have been achieved and this peak is clearly pronounced. We also observe it only for highly transparent contact interfaces.

In the model of Catapano *et al.* we use off-diagonal terms in the potential barrier to model unconventional effects at the interface. The case of a sign change of the superconducting order parameter is for example realized by localized magnetic moments at the interface. This explanation is rather unlikely for our case. These peaks in differential resistance were observed in other material systems as well. And neither in this work, nor in the InAs samples we find a logical explanation, of how a localized magnetic moment could arise at the interfaces. Both materials, HgTe and InAs, have a high spin-orbit coupling (SOC), but the effect is not the same as for a Zeeman term. Since we have no alternative explanation so far, we suggest a theory based on the SOC. It has been shown, that the induced pairing at the interface of SOC material and a superconductor can result in spin singlet and triplet states.[132, 133] To generalize the model of Catapano *et al.* for triplet pairing, we do not need to change much. For a perfectly transparent interface with pairing potential $V(x)$, the channels for spin-up and spin-down electrons and their hole-like partner of opposite spin can be treated independently.[115] We therefore can choose two different $\phi_{1,2}$, and still get the right solution for each channel in the end.

$$V(x) = \begin{pmatrix} 0 & 0 & 0 & U_1 e^{i\phi_1} \\ 0 & 0 & -U_1 e^{i\phi_2} & 0 \\ 0 & -U_1^* e^{-i\phi_2} & 0 & 0 \\ U_1^* e^{-i\phi_1} & 0 & 0 & 0 \end{pmatrix} \delta(x). \tag{17.2}$$

For $\phi_1 = \phi_2$ we get equal solutions for both channels recovering the results depicted in Fig. 16.4 (c) and (e). With $\phi_1 = 0$ and $\phi_2 = \pi$ we get

$$V(x) = \begin{pmatrix} 0 & 0 & 0 & U_1 \\ 0 & 0 & U_1 & 0 \\ 0 & U_1^* & 0 & 0 \\ U_1^* & 0 & 0 & 0 \end{pmatrix} \delta(x). \tag{17.3}$$

In this case, the off-diagonal terms have the form of a superconductor with triplet pairing.[134] We conclude, that a superposition of the solutions for the two spin-channels with $\phi_1 = 0$ and $\phi_2 = \pi$ gives the same result, as if we assume an interface with triplet pairing, but singlet pairing in the bulk superconductor. In both cases, we assume opposite-spin pairing, corresponding to a unitary state in the triplet case.

We achieve transparent interfaces in our Al/HgTe-NW/Al devices. The low resistive regime at small bias voltage and zero magnetic field can be interpreted as a proximity induced, noise limited supercurrent. A positive excess current and multiple Andreev reflections are also observed, and both are a characteristic for highly transparent Josephson junctions. According to the suggested model, the observation of differential resistance peaks at $\frac{\Delta}{e}$ for NW/superconductor and $\frac{2\Delta}{e}$ for superconductor/NW/superconductor junctions in the absence of a Zeeman term can be explained by proximity induced triplet pairing at the N/S interfaces. This is a great success, meaning we do not only observe induced superconductivity, but additionally we report on the signature of the foreseen unconventional pairing at the interface between TI and superconductor.[135, 136, 137, 138] The theory in the end of this chapter is a first try to understand the unconventional signature in our HgTe-NWs in proximity to a superconductor and needs to be verified with the devices and methods introduced in the outlook.

Summary and outlook

Summary

A novel growth method has been developed, allowing for the growth of strained HgTe shells on CdTe nanowires (NWs). The growth of CdTe-HgTe core-shell NWs required high attention in controlling basic parameters like substrate temperature and the intensity of supplied material fluxes. The difficulties in finding optimized growth conditions have been successfully overcome in this work.

We found the lateral redistribution of liquid growth seeds with a ZnTe growth start to be crucial to trigger vertical CdTe NW growth. Single crystalline zinc blende CdTe NWs grew, oriented along [111]B. The substrate temperature was the most critical parameter to achieve straight and long wires. In order to adjust it, the growth was monitored by reflection high-energy electron diffraction, which was used for fine tuning of the temperature over time in each growth run individually. For optimized growth conditions, a periodic diffraction pattern allowed for the detailed analysis of atomic arrangement on the surfaces and in the bulk. The ability to do so reflected the high crystal quality and ensemble uniformity of our CdTe NWs. The NW sides were formed by twelve stable, low-index crystalline facets. We observed two types stepped and polar sides, separated by in total six flat and non-polar facets.

The high crystalline quality of the cores allowed to grow epitaxial HgTe shells around. We reported on two different heterostructure geometries. In the first one, the CdTe NWs exhibit a closed HgTe shell, while for the second one, the CdTe NWs are overgrown mainly on one side. Scanning electron microscopy and scanning transmission electron microscopy confirmed, that many of the core-shell NWs are single crystalline zinc blende and have a high uniformity. The symmetry of the zinc blende unit cell was reduced by residual lattice strain. We used high-resolution X-ray diffraction to reveal the strain level caused by the small lattice mismatch in the heterostructures. Shear strain has been induced by the stepped hetero-interface, thereby stretching the lattice of the HgTe shell by 0.06% along a direction oriented with an angle of 35° to the interface.

The different heterostructures obtained, were the base for further investigation of quasi-one-dimensional crystallites of HgTe. We therefore developed methods to reliably manipulate, align, localize and contact individual NWs, in order to characterize the charge transport in our samples. Bare CdTe cores were insulating, while the HgTe shells were conducting. At low temperature we found the mean free path of charge carriers to be smaller, but the phase coherence length to be larger than the sample size of several hundred nanometers. We observed universal conductance fluctuations and therefore drew the conclusion, that the trajectories of charge carriers are defined by elastic backscattering at randomly distributed scattering sites. When contacted with superconducting leads, we saw induced superconductivity, multiple Andreev reflections and the associated excess current. Thus, we achieved HgTe/superconductor interfaces with high interfacial transparency.

In addition, we reported on the appearance of peaks in differential resistance at $\frac{\Delta}{e}$ for HgTe-NW/superconductor and $\frac{2\Delta}{e}$ for superconductor/HgTe-NW/superconductor junctions, which is possibly related to unconventional pairing at the HgTe/superconductor interface. We noticed that the great advantage of our self-organized growth is the possibility to employ the metallic droplet, formerly seeding the NW growth, as a superconducting contact. The insulating wire cores with a metallic droplet at the tip have been overgrown with HgTe in a fully in-situ process. A very high interface quality was achieved in this case.

Outlook

All together, the performed experiments are a promising base for further research on HgTe-based NWs. In the ballistic transport regime, the band structure can be tuned with an Aharonov-Bohm phase in one device. Also phenomena related to helically spin-polarized electronic surface states can be explored in such samples. Furthermore, a ballistic quasi-one-dimensional topological insulator in proximity to a superconductor is a predicted platform for Majorana bound states. This chapter discusses a few ideas on growth optimization in order to increase the mean free path in the samples, the development of devices for superconducting charge transport in combination with higher magnetic fields, and an experiment to possibly reveal Majorana bound states.

The optimal growth parameters depended on the NW density. For a self-organized process, the density changes locally, which limits the uniformity of growth. We already started to grow NWs from equally spaced droplets. In the growth process discussed in this thesis, the droplets form, when a thin layer of Au absorbs Ga from the substrate. Currently, the eutectic droplets can also be formed, if we pattern the substrate with an array of regularly spaced, nm-sized Au disks and supply a small amount of Ga inside the molecular beam epitaxy chamber. The patterning is done with a standard electron beam lithography process. When we use a GaAs substrate for the pre-patterned process, as we did for the self-organized growth, then one NW grows per pre-defined droplet. So far, mostly no vertical wire growth occurs, since the three-dimensional growth on the lattice mismatched substrate triggers lateral NW growth. Without lattice mismatch, vertical growth is expected. A next step would be the use of a thick ZnTe buffer layer, which is pre-patterned with regularly spaced Au-Ga droplets. Then, ZnTe and subsequently CdTe NWs should grow vertically.

Future experiments should use superconducting contacts with higher critical magnetic field. Niobium, for example, shows a critical field of several Tesla. Deposited by sputtering, the use of Nb gives rise to new lithographical problems like side-walls. For reliable use of such contacts, the process needs further improvement. For now,

the first Nb-contacted device has been tested successfully. It showed differential resistance peaks, possibly related to multiple Andreev reflections, but no supercurrent so far. An idea would be to test thin wetting layers of Ti and Al underneath the Nb, in order to combine the high interface transparency of the materials primarily used in this work with the high critical field of Nb.

The topological surface states are predicted to give rise to exotic superconductivity when coupled to the conventional pairing potential of an s-type superconductor. The unconventional induced superconductivity is predicted to show a 4π-periodic Josephson effect, related to zero energy Andreev bound states (Majorana states).[140] The periodicity can be probed by the dynamics of the junction. To reveal the periodicity of the Josephson supercurrent in experiments, a radio-frequency excitation is added to the DC bias to induce so-called Shapiro steps in the I-V curve.[139] The height of the Shapiro steps is doubled, when the supercurrent is carried by charge-e quasiparticles and not by charge-$2e$ Cooper pairs. Missing odd Shapiro steps, indicating the presence of Majorana end states, were already reported for InSb NWs [141] and bulk-like, strained HgTe [28]. The investigation of this effect is suggested in HgTe-based NWs achieved in this thesis.

Zusammenfassung

Topologische Isolatoren (TI) sind ein faszinierendes Forschungsfeld der Festkörperphysik. Im Inneren sind diese Materialien isolierend, am Rand zeigen sich jedoch topologisch geschützte, leitfähige Oberflächen-Zustände. Ihre lineare Energiedispersion und die Kopplung des Elektronenspins an die Bewegungsrichtung ermöglichen die Untersuchung von Teilchen, die sich als Dirac-Fermionen beschreiben lassen.

Für Nanodrähte, als Vertreter mesoskopischer Strukturen, spielen die Eigenschaften der Oberfläche eine größere Rolle, als für Strukturen mit makroskopischem Volumen. Ihr geringer Umfang beschränkt durch zusätzliche periodische Randbedingungen die erlaubten elektronischen Zustände. Durch ein externes Magnetfeld lassen sich TI-Nanodrähte vom trivialen in den helikalen Zustand überführen. Bringt man einen solchen Draht in direkten Kontakt mit einem Supraleiter, so werden Quasiteilchen vorhergesagt, die sich wie Majorana-Fermionen verhalten sollen.

Zur Untersuchung dieser Phänomene sind zunächst entscheidende technologische Hürden zu überwinden. Verschiedene TI sind derzeit bekannt. HgTe ist einer von ihnen und zeichnet sich bei tiefen Temperaturen durch eine hohe Beweglichkeit der Oberflächen-Elektronen und gleichzeitig einer geringen Leitfähigkeit im Volumen aus. Die bisherigen Untersuchungen in diesem Materialsystem beschränken sich auf zwei- und dreidimensionale Strukturen.

In dieser Arbeit wurde ein Verfahren zur Herstellung von quasi eindimensionalen TI-Nanodrähten entwickelt. Mittels *vapor-liquid-solid* Methode gewachsene CdTe Nanokristallite werden epitaktisch mit HgTe umwachsen. Die hergestellten Heterostrukturen werden mit Beugungsexperimenten charakterisiert, um den Einfluss der Wachstumsparameter wie Temperatur und Teilchenstrom auf die Qualität der Proben zu bestimmen und diese zu verbessern. In dieser Arbeit wird zum ersten mal eine Rekonstruktion der Oberflächenatome von Nanodrähten beschrieben. Für den Rückschluss auf die atomare Konfiguration mittels Elektronenbeugung müssen die einzelnen Kristallite eine hohe Selbstähnlichkeit aufweisen. Wie Bilder in atomarer Auflösung und hochaufgelöste Röntgenbeugung zeigen, werden einkristalline und

verspannte CdTe-HgTe Strukturen erzeugt. Diese sollten die typischen TI Eigenschaften haben. Zur weiteren Untersuchung wurden Verfahren für die Manipulation und exakte Ausrichtung der Nanodrähte, sowie für die Kontaktierung mit verschiedenen Metallen entwickelt. Die blanken CdTe Nanodraht-Kerne selbst sind wie erwartet isolierend, mit HgTe umwachsene Proben jedoch leiten einen elektrischen Strom.

Die aktuelle Forschung beschäftigt sich nun intensiv mit dem Transport von Ladungsträgern durch diese Nanodrähte. Dazu wird die Leitfähigkeit der Proben unter anderem bei tiefen Temperaturen und in Abhängigkeit äußerer elektrostatischer und magnetischer Felder bestimmt. Es werden verschiedene Effekte beobachtet. Universelle Fluktuationen des gemessenen Widerstandes, als ein Beispiel, resultieren aus einer Veränderung der geometrischen Phase der Ladungsträger. Dieser Effekt deutet auf elastische Rückstreuung der Ladungsträger in den HgTe Nanodrähten hin. Die Beobachtung kohärenter Transportphänomene erlaubt den Rückschluss, dass inelastische Streuprozesse bei tiefen Temperaturen kaum eine Rolle spielen.

Für Drähte mit supraleitenden Kontakten können induzierte Supraleitung und multiple Andreev-Reflektionen beobachtet werden. Zusammen mit dem beschriebenen *excess current* ist dies ein klares Zeichen für einen guten elektrischen Kontakt zwischen TI und Supraleiter. Zusätzlich beobachten wir eine Signatur nahe der Kante der Energielücke des Supraleiters, die eventuell durch *pairing* an der Grenzfläche zu erklären ist. Für die Verbindung von Spin-Bahn-Kopplung des TI und der Cooper-Paare des konventionellen Supraleiters wird die Entstehung eines unkonventionellen Supraleiters vorhergesagt. Dies ist ein weiteres interessantes Feld der modernen Festkörperphysik und Gegenstand aktueller Forschung.

Besonders bemerkenswert ist in diesem Zusammenhang, dass der metallische Tropfen, welcher ursprünglich das Nanodraht-Wachstum katalysiert hat, bei tiefen Temperaturen supraleitend wird. Der in dieser Arbeit vorgestellte selbst-organisierte Wachstumsprozess resultiert in einer sauberen Grenzfläche zwischen TI und Supraleiter. Zur Untersuchung der Effekte an dieser Grenzfläche muss nicht zwingend in einem separaten Schritt ein supraleitender Kontakt aufgebracht werden. Die in dieser Arbeit vorgestellten Methoden und Erkenntnisse sind die Grundlage für die Realisierung von Experimenten, die geeignet wären, die erwarteten Majorana-Zustände in TI-Nanodrähten nachzuweisen.

Appendix

Parameters for defining metallic contacts

Step	Parameters
Substrate	n^{++}-doped Si (001), covered with 100 nm thermally oxidized SiO_2, SSP, 1 cm^2.
DEP structure	Standard EBL, or one can use the same parameters as listed for the leads. 4-9 electrodes per substrate, metallized with 5 nm Ti and 20-25 nm Au
Suspension	4 mm^2 as-grown substrate, add 1-3 ml IPA, then 2 min ultrasonic cavitation at 37 kHz.
DEP	$\pm$10 V at 1-2 MHz for 1-10 min, till about 3 promising wires are attracted to each electrode.
E-beam resist	PMMA 600K 6%, 40 s spin-coating at 6 krpm, 10 min hotplate at 80 °C (420 nm height) PMMA 950K 3%, 40 s spin-coating at 6 krpm, 10 min hotplate at 70 °C (120 nm height)
EBL leads	30 kV, 20 µm aperture, 500 µC/cm^2, 204.8x204.8 µm^2 writefield, 390x magn., 4 pix. = 12.5 nm
EBL pads	30 kV, 60 µm aperture, 380 µC/cm^2, 819.2x819.2 µm^2 writefield, 87x magn., 4 pix. = 50 nm
Development	1:20 min AR600-56:IPA 1:1 (3 s ultrasound), 1:10 min IPA (3s US), DI-water, blow dry with N_2.
In-situ Cluster	6-45 s Ar-beam etch (1.62 sccm Ar, 1 kV plasma, -1 kV extraction, 8 mA beam current), followed by metalization (for material stack see table of transport samples)
Lift-off	Acetone (50 °C hotplate for 60 min), rinse in IPA, blow dry with N_2-gun.
Cleave	PMMA for protection (600K 6% with 3 krpm), cleave the sample, scratch the backside to contact the backgate, clean in Acetone and IPA, blow dry.
Glue	Use silver-filled epoxy paste (EPO-TEK E4110) to glue the samples into the chip-carrier, then cure 3 days at room temperature.
Bonding	Use protective bonds, that connect all pads of the chip carrier, before bonding to the sample. Only use glue bonding on the bond pads to not break the backgate insulator underneath.

The table lists subsequent steps to successfully integrate NWs into electrical circuits. The transport samples fabricated like that are listed in the following.

Samples for charge transport: Aluminum contacts

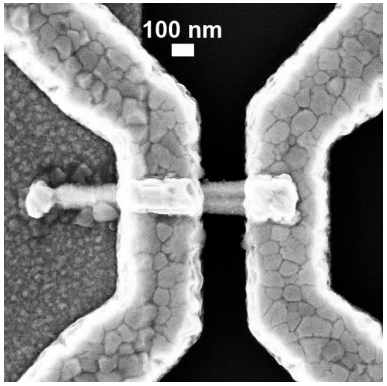

$Al^{\#}1$

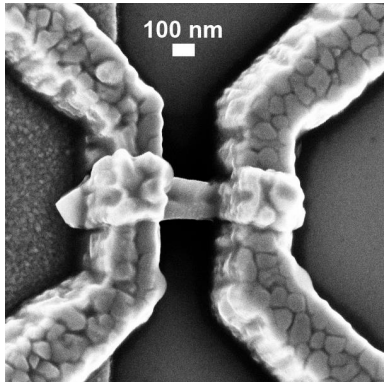

$Al^{\#}2$

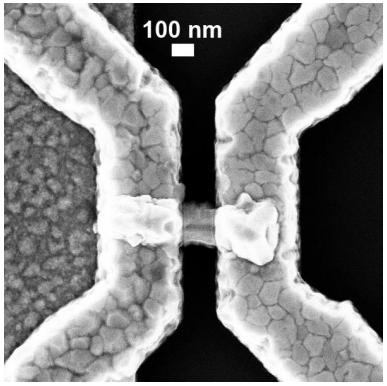

$Al^{\#}3$

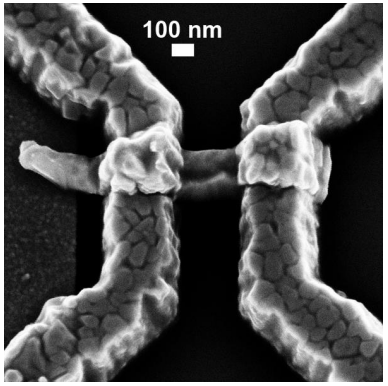

$Al^{\#}4$

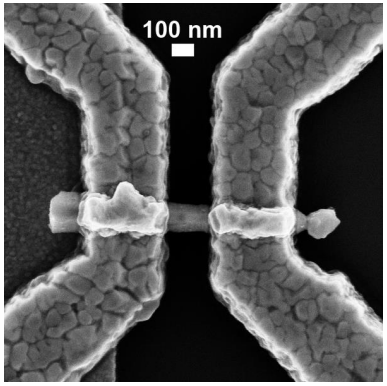

$Al^{\#}5$

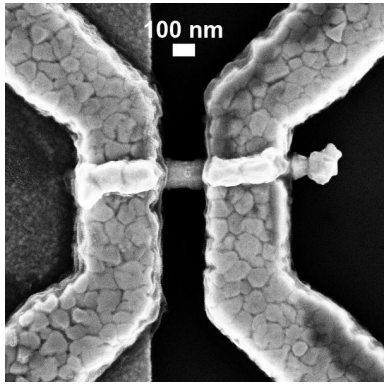

$Al^{\#}6$

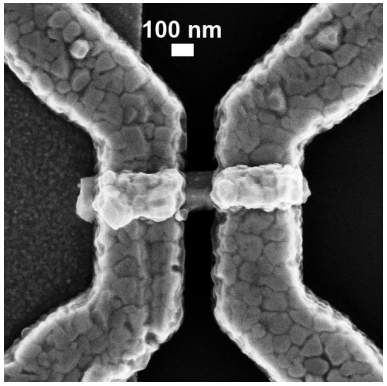

$Al^{\#}7$

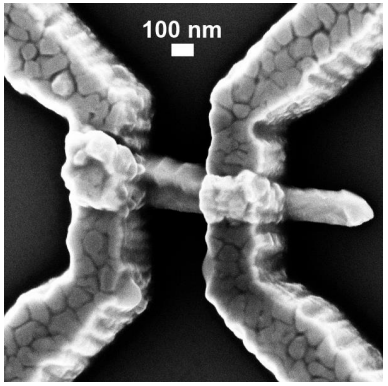

$Al^{\#}8$

Samples for charge transport: Titanium contacts

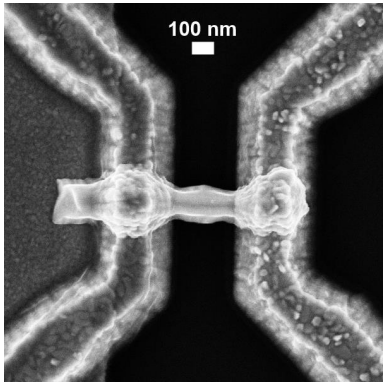

Ti$^{\#}$1

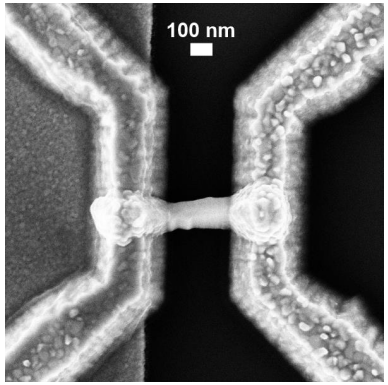

Ti$^{\#}$2

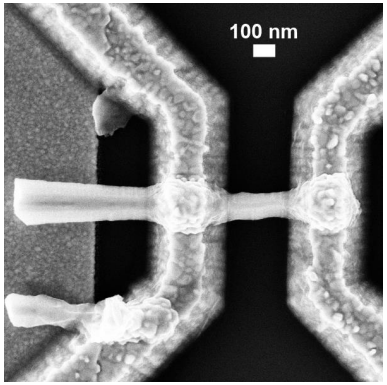

Ti$^{\#}$3

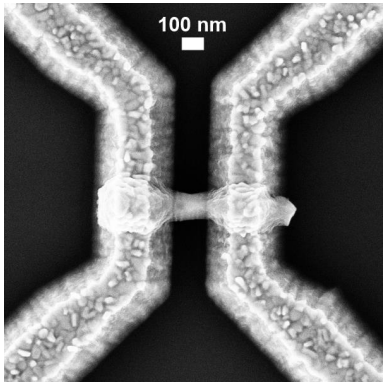

Ti$^{\#}$4

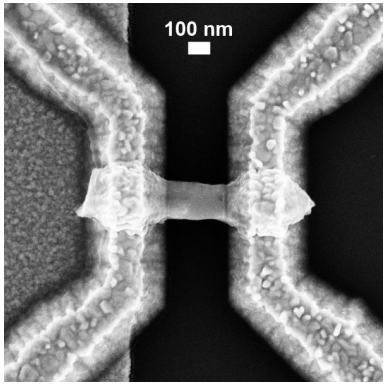

Ti$^{\#}$5

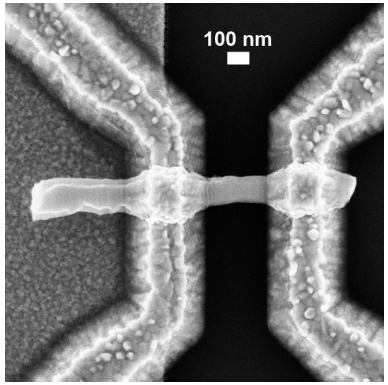

Ti$^{\#}$6

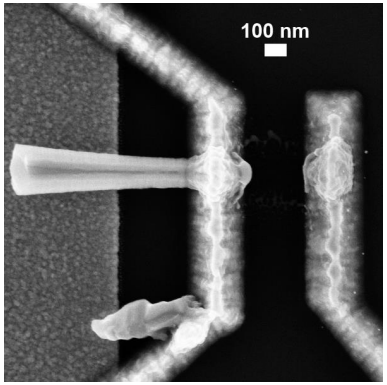

Ti$^{\#}$7

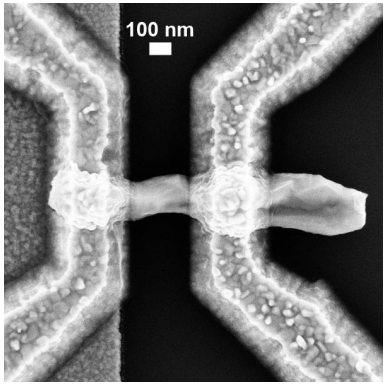

Ti$^{\#}$8

Samples for charge transport: Basic characterization

Sample	Full Name	Contact Stack	Contact Distance [nm] ±10 nm	NW Width [nm] ±10 nm	R [Ω] ±5%
Al#1	QW36/S09/M5c	Au cap	210	155	1392
Al#2	QW36/S08/M4b	5 nm Ti	290	190	995
Al#3	QW36/S09/M5a	thick Al	160	190	773
Al#4	QW36/S08/M4c	5 nm Ti	280	240	517
Al#5	QW36/S10/M4a		210	135	1871
Al#6	QW36/S10/M1b		200	130	1633
Al#7	QW36/S10/M4b		140	175	876
Al#8	QW36/S08/M6b		270	220	572
Ti#1	QW36/S11/M4a	Au cap	290	180	1339
Ti#2	QW36/S11/M4b	thick Ti	290	140	1122
Ti#3	QW36/S11/M4c		290	125	1022
Ti#4	QW36/S11/M4f		160	125	576
Ti#5	QW36/S11/M6b		300	180	1591
Ti#6	QW36/S11/M6d		300	125	1636
Ti#7	QW36/S11/M6c		290	130	1394
Ti#8	QW36/S11/M6a		285	170	1085

Basic characterization of the charge transport samples. R is the low temperature resistance at a small magnetic field to exclude superconducting effects thus making the measurements with different contact material comparable.

References

[1] L. Fu *et al.* "Topological Insulators with inversion symmetry", *Phys. Rev. B* **76**, 045302 (2007).

[2] M. Z. Hasan *et al.* "Colloquium: Topological Insulators", *Rev. Mod. Phys.* **82**, 3045 (2010).

[3] J. E. Moore, "The birth of topological insulators", *Nature* **464**, pp. 194-198 (2010).

[4] Xiao-Liang Qi and Shou-Cheng Zhang, "Topological insulators and superconductors", *Rev. Mod. Phys.* **83**, pp. 1057-1110 (2011).

[5] B. A. Bernevig *et al.* "Quantum Spin Hall Effect and Topological Phase Transition in HgTe Quantum Wells", *Science* **314**, 5806, pp. 1757-1761 (2006).

[6] M. König, S. Wiedmann, C. Brüne, A. Roth, H. Buhmann, L. W. Molenkamp, X.-L. Qi, and S.-C. Zhang, "Quantum Spin Hall Insulator State in HgTe Quantum Wells", *Science* **318**, 5851, pp. 766-770 (2007).

[7] X. Dai *et al.* "Helical edge and surface states in HgTe quantum wells and bulk insulators", *Phys. Rev. B* **77**, 12, 125319 (2008).

[8] Y. L. Chen *et al.* "Experimental Realization of a Three-Dimensional Topological Insulator, Bi_2Te_3", *Science* **325**, 5937, pp. 178-181 (2009).

[9] R. Egger, A. Zazunov, and A. Levy Yeyati, "Helical Luttinger liquid in topological insulator nanowires", *Phys. Rev. Lett.* **105**, 13, 136403 (2010).

[10] S. S. Hong *et al.* "One-dimensional helical transport in topological insulator nanowire interferometers", *Nano Letters* **14**, 5, pp. 2815-2821 (2014).

[11] C. Brüne *et al.* "Quantum Hall effect from the topological surface states of strained bulk HgTe", *Phys. Rev. Lett.* **106**, 12, 126803 (2011).

[12] A. Cook, and M. Franz, "Majorana fermions in a topological-insulator nanowire proximity-coupled to an s-wave superconductor", *Phys. Rev. B* **84**, 20, 201105 (2011).

[13] J. Alicea, "New directions in the pursuit of Majorana fermions in solid state systems", arXiv:1202.1293v1 (2012).

[14] C. W. J. Beenakker, "Search for Majorana fermions in superconductors", arXiv:1112.1950v2 (2012).

[15] M. A. Herman, and H. Sitter, "Molecular Beam Epitaxy - Fundamentals and Current Status", *Materials Science* **7**, Springer (1989).

[16] P. Capper, and J. Garland, "Mercury Cadmium Telluride: Growth, Properties and Applications", John Wiley & Sons (2011).

[17] R. G. Benz, B.K. Wagner, A. Conte, and C.J. Summers, "CdTe and HgTe Surface Growth Kinetics for Molecular and Metalorganic Molecular Beam Epitaxy", *Journal of Electronic Materials* **22**, 8, pp. 815 (1993).

[18] G. Dhanaraj, K. Byrappa, V. Prasad, M. Dudley, "Springer Handbook of Crystal Growth", Springer (2010).

[19] C. Ames, "Molecular beam epitaxy of 2D and 3D HgTe, a topological insulator", Dissertation, Universität Würzburg (2015).

[20] R. Wagner, and W. Ellis, "Vapour-liquid-solid mechanism of single crystal growth", *Appl. Phys. Lett.* **4**, pp. 89-90 (1964).

[21] H. J. Fan, P. Werner, and M. Zacharias, "Semiconductor Nanowires: From Self-Organization to Patterned Growth", *small 2006* **2**, 6, pp. 700-717 (2006).

[22] Chang Liu *et al.* "Tunable spin helical Dirac quasiparticles on the surface of three-dimensional HgTe", *Phys. Rev. B* **92**, 115436 (2015).

[23] D. Ferrand, and J. Cibert, "Strain in crystalline core-shell nanowires", *Eur. Phys. J. Appl. Phys.* **67**, 3, 30403 (2014).

[24] C. P. Kuo *et al.* "Effect of mismatch strain on band gap in III-V semiconductors", *J. Appl. Phys.* **57**, 12, pp. 5428-5432 (1985).

[25] Huxian Zhao *et al.* "Band gap tuning in HgTe through uniaxial strains", *Solid State Communications* **166**, 1-5 (2013).

[26] O. Crauste, Y. Ohtsubo, P. Ballet, P. Delplace, D. Carpentier, C. Bouvier, T. Meunier, A. Taleb-Ibrahimi, and L. P. Lévy, "Topological surface states of strained Mercury-Telluride probed by ARPES", arXiv:1307.2008v1 (2013).

[27] C. Brüne, C. Thienel, M. Stuiber, J. Böttcher, H. Buhmann, E. G. Novik, Chao-Xing Liu, E. M. Hankiewicz, and L. W. Molenkamp, "Dirac-Screening Stabilized Surface-State Transport in a Topological Insulator", *Phys. Rev. X* **4**, 041045 (2014).

[28] J. Wiedenmann *et al.* "4π-periodic Josephson supercurrent in HgTe-based topological Josephson junctions", *Nat. Commun.* **7**, 10303 (2016).

[29] S. Neretina, R. A. Hughes, J. F. Britten, N. V. Sochinskii, J.S. Preston and P. Mascher, "Vertically aligned wurtzite CdTe nanowires derived from a catalytically driven growth mode", *Nanotechnology* **18**, 275301 (2007).

[30] L. Huang, S. Lu, P. Chang, K. Banerjee, R. Hellwarth and J. G. Lu, "Structural and optical verification of residual strain effect in single crystalline CdTe nanowires", *Nano Research* **7** (2), pp. 228-235 (2014).

[31] T. Wojtowicz, E. Janik, W. Zaleszczyk, J. Sadowski, G. Karczewski, P. Dluzewski, S. Kret, W. Szuszkiewicz, E. Dynowska, J. Domagala, M. Aleszkiewicz, L. T. Baczewski and A. Petroutchik, "MBE Growth and Properties of ZnTe- and CdTe-Based Nanowires", *Journ. of the Korean Phys. Soc.* **53**, 5, pp. 3055-3063 (2008).

[32] E. Janik, J. Sadowski, P. Dluzewski, S. Kret, L. T. Baczewski, A. Petroutchik, E. Lusakowska, J. Wróbel, W. Zaleszczyk, G. Karczewski, T. Wojtowicz, and A. Presz, "ZnTe nanowires grown on GaAs(100) substrates by molecular beam epitaxy", *Appl. Phys. Lett.* **89**, 133114 (2006).

[33] E. Janik, P. Dluzewski, S. Kret, A. Presz, H. Kirmse, W. Neumann, W. Zaleszczyk, L. T. Baczewski, A. Petroutchik, E. Dynowska, J. Sadowski, W. Caliebe, G. Karczewski and T. Wojtowicz, "Catalytic growth of ZnTe nanowires by molecular beam epitaxy: structural studies", *Nanotechnology* **18**, 475606 (2007).

[34] S. Bieker, R. Pfeuffer, T. Kiessling, N. V. Tarakina, C. Schuhmacher, W. Ossau, L. W. Molenkamp, and G. Karczewski, "Polytypism and band alignment in ZnSe nanowires revealed by photoluminescence spectroscopy of embedded (Zn,Cd)Se quantum dots", *Phys. Rev. B* **91**, 12, 125301 (2015).

[35] E. Selvig, S. Hadzialic, T. Skauli, H. Steen, V. Hansen, L. Trosdahl-Iversen, A. D. van Rheenen, T. Lorentzen and R. Haakenaasen, "Growth of HgTe nanowires", *Phys. Scr.* **T126**, pp. 115-120 (2006).

[36] R. Haakenaasen, E. Selvig, S. Foss, L. Trosdahl-Iversen and J. Tafto, "Segmented nanowires of HgTe and Te grown by molecular beam epitaxy", *Appl. Phys. Lett.* **92**, 133108 (2008).

[37] N. W. Ashcroft, N. D. Mermin, "Solid State Physics", Thomson Learning (1979).

[38] A. Pfeuffer-Jeschke, "Bandstruktur und Laudau-Niveaus quecksilberhaltiger II-VI-Heterostrukturen", Dissertation, Universität Würzburg (2000).

[39] B. Predel, "Au-Ga", *Landolt-Börnstein - Group IV Physical Chemistry* **5a**, pp. 1-5, Springer (1992).

[40] V. H. Etgens, M. Sauvage-Simkin, R. Pinchaux, J. Massies, N. Jedrecy, A. Waldhauer, S. Tatarenko, and P. H. Jouneau, "ZnTe/GaAs(001): Growth mode and strain evolution during the early stages of molecular-

beam-epitaxy heteroepitaxial growth", *Phys. Rev. B* **47**, 16, 10608 (1992).

[41] M. Longo, N. Lovergine, A. M. Mancini, G. Leo, and M. Berti, "Investigation of growth mode behavior and surface morphology evolution of metalorganic vapor phase epitaxy grown ZnTe layers on (001) GaAs", *Jour. Vac. Sci. Tech. B* **16**, 2650 (1998).

[42] F. Brochard, "Motions of Droplets on Solid Surfaces Induced by Chemical or Thermal Gradients", *Langmuir* **5**, pp. 432-438 (1989).

[43] R. S. Subramanian, N. Moumen, and J. B. McLaughlin, "Motion of a Drop on a Solid Surface Due to a Wettability Gradient", *Langmuir* **21**, pp. 11844-11849 (2005).

[44] H. Kirmse, I. Häusler, S. Kret, E. Janik, G. Karczewski and T. Wojtowicz, "TEM analysis of the container effect of Au-based catalyst droplets during vapour-liquid-solid growth of axial ZnTe/CdTe nanowires", *Cryst. Res. Technol.* **44**, 10, pp. 1047 – 1053 (2009).

[45] S. G. Walkauskas, D. A. Broido, K. Kempa, and T. L. Reinecke", Lattice thermal conductivity of wires", *J. Appl. Phys.* **85**, 2579 (1999).

[46] X. Lü, W. Z. Shen, and J. H. Chu, "Size effect on the thermal conductivity of nanowires", *J. Appl. Phys.* **91**, 1542 (2002).

[47] S. Oehling, M. Ehinger, W. Spahn, A. Waag, C. R. Becker, and G. Landwehr, "Mechanisms of molecular beam epitaxial growth of (001) HgTe", *J. Appl. Phys.* **79** (2), 748 (1995).

[48] C. R. Becker, X. C. Zhang, K. Ortner, J. Schmidt, A. Pfeuffer-Jeschke, V. Latussek, Y. S. Gui, V. Daumer, J. Liu, H. Buhmann, G. Landwehr, L.W Molenkamp, "MBE growth and characterization of Hg based compounds and heterostructures", *Thin Solid Films* **412**, 129-138 (2002).

[49] S. Sivananthan, X. Chu, J. Reno, and J. P. Faurie, "Relation between crystllographic orientation and the condensation coefficients of Hg, Cd, and Te during molecular-beam-epitaxial growth of $Hg_{1-x}Cd_xTe$ and CdTe", *J. Appl. Phys.* **60**, 1359 (1986).

[50] R. J. Koestner and H. F. Schaake, "Kinetics of molecularbeam epitaxial HgCdTe growth", *Jour. Vac. Sci. Tech. A* **6**, 2834 (1988).

[51] M. V. Yakushev, A. A. Babenko, and Yu. G. Sidorov, "Effect of Orientation of the Substrate on the Conditions of Growth of HgTe Films by Molecular Beam Epitaxy", *Inorganic Materials* **45**, 1, pp. 13-18 (2009).

[52] E. G. Gillan, A. R. Barron, "Chemical Vapor Deposition of Hexagonal Gallium Selenide and Telluride Films from Cubane Precursors: Understanding the Envelope of Molecular Control", *Chem. Mater.* **9**, pp. 3037-3048 (1997).

[53] O. A. Balitskii, B. Jaeckel, W. Jaegermann, "Surface properties of GaTe single crystals", *Physics Letters A* **372**, pp. 3303-3306 (2008).

[54] W. H. Miller, "A treatise on crystallography", Deighton, Cambridge (1839).

[55] W. Demtröder, "Experimentalphysik 3 - Atome, Moleküle und Festkörper", 3. Edition, Springer (2005).

[56] S. Hunklinger, "Festkörperphysik", 2. Auflage, Oldenbourg Wissenschaftsverlag, München (2009).

[57] M. Regnet, "Hochaufgelöste Röntgenbeugung zur Charakterisierung gestörter Heterostrukturen auf der Basis von II-VI Halbleitermaterialien", Dissertation, Universität Würzburg (1991).

[58] T. F. Gerhard, "Neue Methoden der Röntgenbeugung mit Hilfe von Synchrotronstrahlung", Dissertantion, Universität Würzburg (1999).

[59] P. P. Ewald, "Zur Theorie der Interferenzen der Röntgenstrahlen in Kristallen", *Physikalische Zeitschrift* **14**, 11, 465 (1913).

[60] F. Hottier, J. B. Theeten, A. Masson and J. L. Domange, "Competative LEED and RHEED Examination of Stepped Surfaces; Application to Cu(111) and GaAs(001) Vincial Surfaces", *Surf. Sci.* **65**, pp. 563-577 (1977).

[61] M. Henzler, "Atomic Steps on Single Crystals: Experimental Methods and Properties", *Appl. Phys.* **9**, pp. 11-17 (1976).

[62] M. Tchernycheva, J. C. Harmand, G. Patriarche, L. Travers and G. E. Cirlin, "Temperature conditions for GaAs nanowire formation by Au-assisted molecular beam epitaxy", *Nanotechnology* **17**, pp. 4025-4030 (2006).

[63] C. K. Egan, Q. Z. Jiang and A. W. Brinkmann, "Morphology and reconstructions of polar CdTe(111)A,B surfaces by scanning tunneling microscopy", *Jour. Vac. Sci. Tech. A*, 011021 (2011).

[64] E. Uccelli, J. Arbiol, C. Magen, P. Krogstrup, E. Russo-Averchi, M. Heiss, G. Mugny, F. Morier-Gernoud, J. Nygard, J. R. Morante and A. Fontcuberta i Morral, "Three-Dimensional Multiple-Order Twinning of Self-Catalyzed GaAs Nanowires on Si Substrates", *Nano Lett.* **11**, pp. 3827-3832 (2011).

[65] All STEM images have been recorded by N. Tarakina.

[66] M. Li, C. R. Becker, R. Gall, W. Faschinger, and G. Landwehr, "X-ray reciprocal space mapping of a (112) oriented HgTe/Hg0.1Cd0.9Te superlattice", *Appl. Phys. Lett* **71**, 1822 (1997).

[67] Yongxin Qiua, Meicheng Lia, Guojun Liub, Baoshun Zhangb, Yong Wangb, Liancheng Zhao, "Investigation of crystallographic tilting in GaSb/GaAs heteroepitaxial structure by high-resolution X-ray diffraction", *Journal of Crystal Growth* **308**, pp. 325-329 (2007).

[68] Haruo Nagai, "Structure of vapor-deposited $Ga_xIn_{1-x}As$ crystals", *Jour. Appl. Phys.* **45**, 3789 (1974).

[69] J. E. Ayers, S. K. Ghandhi, and L. J. Schowalter, "Crystallographic tilting of heteroepitaxial layers", *Journal of Crystal Growth* **113**, pp. 430-440 (1991).

[70] Li Wang, Fusheng Huang, Zhiyong Cui, Qin Wu, Wen Liu, Changda Zheng, Qinghua Mao, Chuanbing Xiong, and Fengyi Jiang, "Crystallographic tilting of AlN/GaN layers on miscut Si (111) substrates", *Materials Letters* **115**, pp. 89-91 (2014).

[71] C. Li, J. Poplawsky, Y. Wu, A. R. Lupini, A. Mouti, D. N. Leonard, N. Paudel, K. Jones, W. Yin, M. Al-Jassim, Y. Yan, S. J. Pennycook, "From atomic structure to photovoltaic properties in CdTe solar cells", *Ultramicroscopy* **134**, pp. 113-125 (2013).

[72] G. L. Bir and G. E. Pikus, "Symmetry and strain-induced effects in semiconductors", JOHN WILEY & SONS (1974).

[73] A. Roth, "Nanolithographie auf HgTe-Heterostrukturen", Diplomarbeit, Universität Würzburg (2007).

[74] M. J. Mühlbauer, "Nanolithography on Mercury Telluride", Dissertation, Universität Würzburg (2015).

[75] H. A. Pohl, "The Motion and Precipitation of Suspensoids in Divergent Electrical Fields", *J. Appl. Phys.* **22**, 7, pp. 869-871 (1951).

[76] B. R. Burg, V. Bianco, J. Schneider, and D. Poulikakos, "Electrokinetic framework of dielectrophoretic deposition devices", *J. Appl. Phys.* **107**, 124308 (2010).

[77] J. Hajer, "II-VI Nanodrähte: Herstellung durch VLS-MBE und Manipulation mittels Dielektrophorese", Bachelorarbeit, Universität Würzburg (2014).

[78] J. D. Jackson, "Classical Electrodynamics", 3. Auflage, John Wiley & Sons (1999).

[79] S. Raychaudhuri *et al.* "Precise Semiconductor Nanowire Placement Through Dielectrophoresis", *Nano Letters* **9**, 6, pp. 2260-2266 (2009).

[80] H. Helmholtz, "Ueber einige Gesetze der Vertheilung elektrischer Ströme in körperlichen Leitern mit Anwendung auf die thierisch-elektrischen Versuche", *Annalen der Physik und Chemie* **165**, 6, pp. 211–233 (1853).

[81] M. Schneider, "Charakterisierung des Ladungstransports in II–VI Halbleiternanodrähten", Diplomarbeit, Universität Würzburg (2013).

[82] J. Brehm, "Nanometer Lithographie an Quasi-1D HgTe Heterostrukturen", Masterarbeit, Universität Würzburg (2014).

[83] C. Thienel, "Exploring the transport properties of the three-dimensional topological insulator material HgTe", Dissertation, Universität Würzburg (2015).

[84] F. Xiu, L. He, Y. Wang, L. Cheng, Li-Te Chang, M. Lang, G. Huang, X. Kou, Y. Zhou, X. Jiang, Z. Chen, J. Zou, A. Shailos and K. L. Wang, "Manipulating surface states in topological insulator nanoribbons", *Nature Nanotechnology* **6**, 216 (2011).

[85] L. A. Jauregui, M. T. Pettes, L. P. Rokhinson, L. Shi and Y. P. Chen, "Gate Tunable Relativistic Mass and Berry's phase in Topological Insulator Nanoribbon Field Effect Devices", *Scientific Reports* **5**, 8452 (2015).

[86] H. E. Hall, P. J. Ford, and K. Thomson, "A helium-3 dilution refrigerator", *Cryogenics* **6**, pp. 80–88 (1966).

[87] J. Tian, C. Chang, H. Cao, K. He, X. Ma, Q. Xue and Y. P. Chen, "Quantum and Classical Magnetoresistance in Ambipolar Topological Insulator Transistors with Gate-tunable Bulk and Surface Conduction", *Scientific Reports* **4**, 4859 (2014).

[88] M. M. Parish, P. B. Littlewood, "Non-saturating magnetoresistance in heavily disordered semiconductors", *Nature* **426**, pp. 162–165 (2003).

[89] J. Hu, M. M. Parish, T. F. Rosebaum, "Nonsaturating magnetoresistance of inhomogeneous conductors: comparison of experiment and simulation", *Phys. Rev. B* **75**, 214203 (2007).

[90] A. A. Abrikosov, "Quantum magnetoresistance", *Phys. Rev. B* **58**, pp. 2788–2794 (1998).

[91] A. A. Abrikosov, "Quantum linear magnetoresistance", *Europhys. Lett.* **49**, pp. 789–793 (2000).

[92] A. B. Pippard, "Magnetoresistance in Metals", Cambridge University Press (1989).

[93] Y. M. Galperin, "Quantum Transport - Lecture Notes", Lund University (1998).

[94] P. A. Lee, A. D. Stone, "Universal Conductance Fluctuations in Metals", *Phys. Rev. Lett.* **55**, 15, 1622 (1985).

[95] M. Jung, J. Sung Lee, W. Song, Y. H. Kim, S. D. Lee, N. Kim, J. Park, M.-S. Choi, S. Katsumoto, H. Lee and J. Kim, "Quantum Interference in Radial Heterostructure Nanowires", *Nano Letters* **8**, 10, pp. 3189-3193 (2008).

[96] S. S. Hong, Y. Zhang, J. J. Cha, X.-L. Qi, "One-Dimensional Helical Transport in Topological Insulator Nanowire Interferometers", *Nano Letters* **14**, 5, pp. 2815-2821 (2014).

[97] L. Fu, C. L. Kane and E. J. Mele, "Topological Insulators in Three Dimensions", *Phys. Rev. Lett.* **98**, 106803 (2007).

[98] J. H. Bardarson, P. W. Brouwer and J. E. Moore, "Aharonov-Bohm Oscillations in Disordered Topological Insulator Nanowires", *Phys. Rev. Lett.* **105**, 156803 (2010).

[99] Di Xiao, Ming-Che Chang, Qian Niu, "Berry phase effects on electronic properties", *Rev. Mod. Phys.* **82**, pp. 1959-2007 (2010).

[100] Y. Zhang, Y. Ran and A. Vishwanath, "Topological insulators in three dimensions from spontaneous symmetry breaking", *Phys. Rev. B* **79**, 245331 (2009).

[101] W. Franz, "Elektroneninterferenzen im Magnetfeld", *Verhandlungen der Deutschen Physikalischen Gesellschaft* **65** (1939).

[102] Y. Aharonov, D. Bohm, "Significance of Electromagnetic Potentials in the Quantum Theory", *The Physical Review* **115**, 3, pp. 485–491 (1959).

[103] T. O. Rosdahl, A. Manolescu and V. Gudmundsson, "Spin and impurity effects on flux-periodic oscillations in core-shell nanowires", *Phys. Rev. B* **90**, 035421 (2014).

[104] M. König, A. Tschetschetkin, E. M. Hankiewicz, Jairo Sinova, V.

Hock, V. Daumer, M. Schäfer, C. R. Becker, H. Buhmann and L. W. Molenkamp, "Direct observation of a Aharonov-Casher phase", *Phys. Rev. Lett.* **96**, 076804 (2006).

[105] B. T. Matthias, T. H. Geballe, and V. B. Compton, "Superconductivity", *Rev. Mod. Phys.* **35**, 1 (1963).

[106] J. Eisenstein, "Superconducting Elements", *Reviews of Modern Physics* **26**, 3, 277 (1954).

[107] D. van Delft and P. Kes, "The discovery of superconductivity", *Physics Today* **63**, 9, pp. 38-42 (2010).

[108] H. R. Khan, "Superconducting Gold Alloys", *Gold Bull.* **17**, 3, (1984).

[109] P. Xiong, G. Xiao, R. B. Laibowitz, "Subgap ad Above-Gap Differential Resistance Anomalies in Superconductor-Normal-Metal Microjunctions", *Phys. Rev. Lett.* **71**, 12, 1907 (1993).

[110] Fan Yang *et al.* "Proximity effect at superconducting Sn-$Bi_2Se_§$ interface", *Phys. Rev. B*, **85**, 104508 (2012).

[111] J. Bardeen, L. N. Cooper, and J. R. Schrieffer, "Theory of Superconductivity", *Phys. Rev.* **108**, 5, pp. 1175-1204 (1957).

[112] W. Buckel, "Supraleitung", 4. Auflage, VCH, Weinheim (1990).

[113] G. E. Blonder, M. Tinkham, and T. M. Klapwijk, "Transition from metallic to tunneling regimes in superconducting microconstrictions: Excess current, charge imbalance, and supercurrent conversion", *Phys. Rev. B* **25**, 7, 4515 (1982).

[114] A. F. Andreev, "The thermal conductivity of the intermediate state in superconductors", *Soviet Physics JETP* **19**, 5, pp. 1228-1231 (1964).

[115] M. Catapano, F. Romeo, R. Citro, and F. Giubileo, "Generalization of Blonder-Tinkham-Klapwijk theory to particle-hole mixing boundary conditions: π-shift and conductance dips", arXiv:1502.07931v1 (2015).

[116] D. H. Douglass, Jr. "Magnetic field dependence of the superconducting energy gap", *Phys. Rev. Lett.* **6**, 7, 346 (1961).

[117] J. F. Chochran, D. E. Mapother, "Superconducting Transition in Aluminum", *Phys. Rev.* **111**, 132 (1958).

[118] V. Ambegaokar, B. Halperin, "Voltage due to thermal noise in the dc Josephson effect", *Phys. Rev. Lett.* **22**, 1364 (1969).

[119] M. Tinkham, "Introduction to Superconductivity", 2. edition, Dover (2004).

[120] Yong-Joo Doh, J. A. van Dam, A. L. Roest, E. P. A. M. Bakkers, Leo P. Kouwenhoven, S. De Franceschi, "Tunable Suppercurrent Through Semiconductor Nanowires", *Science* **309**, pp. 272-275 (2005).

[121] P. Dubos, H. Courtois, B. Pannetier, F. K. Wilhelm, A. D. Zaikin, and G. Schön, "Josephson critical current in a long mesoscopic S-N-S junction", *Phys. Rev. B* **63**, 064502 (2001).

[122] F. F. Wilhelm, A. D. Zaikin, and G. Schön, "Supercurrent in a mesoscopic proximity wire", *Jour. of Low Temp. Phys.* **106**, 314, pp. 305-310 (1997).

[123] J. B. Oostinga *et al.* "Josephson Supercurrent through the Topological Surface States of Strained Bulk HgTe", *Phys. Rev. X.* **3**, 021007 (2013).

[124] L. Maier, "Induced superconductivity in the topological insulator mercury telluride", Dissertation, Universität Würzburg (2015).

[125] B. Mühlschlegel, "Die therodynamischen Funktionen des Supraleiters", *Zeitschrift für Physik* **155**, pp. 313-327 (1959).

[126] K. Flensberg, J. Bindslev Hansen, and M. Octavio, "Subharmonic energy-gap structure in superconducting weak links", *Phys. Rev. B* **38**, 13, pp. 8707-8711 (1988).

[127] G. Niebler, G. Cuniberti, and T. Novotny, "Analytical calculation of the excess current in the Octavio–Tinkham–Blonder–Klapwijk theory", *Supercond. Sci. Technol.* **22**, 085016 (2009).

[128] M. Octavio, M. Tinkham, G. E. Blonder, and T. M. Klapwijk, "Subharmonic energy-gap structure in superconducting constrictions", *Phys. Rev. B.* **27**, 11, pp. 6739-6746 (1983).

[129] M. Kjaergaards, H. J. Suominen, M. P. Nowak, A. R. Akhmerov, J. Shabani, C. J. Palmstrom, F. Nichele, and C. M. Marcus, "Transparent Semiconductor-Superconductor Interface and Induced Gap in an Epitaxial Heterostructure Josephson Junction", arXiv:1607.04164v2 (2016).

[130] H. Y. Günel, I. E. Batov, H. Hardtdegen, K. Sladek, A. Winden, K. Weis, G. Panaitov, D. Grützmacher, and Th. Schäpers, "Supercurrent in Nb/InAs-nanowire/Nb Josephson junctions", *J. Appl. Phys.* **112**, 034316 (2012).

[131] S. Abay, D. Persson, H. Nilsson, F. Wu, H. Q. Xu, M. Fogelström, V. Shumeiko, and P. Delsing, "Charge transport in InAs nanowire Josephson junctions", *Phys. Rev. B* **89**, 214508 (2014).

[132] A. C. Pottter and P. A. Lee, "Engenieering a $p + ip$ superconductor: Comparison of topological insulator and rashba spin-orbit coupled materials", *Phys. Rev. B* **83**, 184520 (2011).

[133] P. Burset, F. Keidel, Y. Tanaka, N. Nagaosa, and B. Trauzettel, "Transport signatures of superconducting hybrids with mixed singlet and chiral triplet states", *Phys. Rev. B* **90**, 085438 (2014).

[134] M. Sigrist and K. Ueda, "Phenomenological theory of unconventional superconductivity", *Rev. Mod. Phys.* **63**, 2, pp. 239-311 (1991).

[135] L. Fu, and C. L. Kane, "Superconducting Proximity Effect and Majorana Fermions at the Surface of a Topological Insulator", *Phys. Rev. Lett.* **100**, 096407 (2008).

[136] T. D. Stanescu, J. D. Sau, R. M. Lutchyn, and S. D. Sarma, "Proximity effect at the superconductor–topological insulator interface", *Phys. Rev. B* **81**, 241310 (2010).

[137] A. M. Black-Schaffer and A. V. Balatsky, "Proximity-induced uncon-

ventional superconductivity in topological insulators", *Phys. rev. B* **87**, 220506(R) (2013).

[138] G. Tkachov, "Suppression of surface p-wave superconductivity in disordered topological insulators", *Phys. Rev. B* **87**, 245422 (2013).

[139] S. Shapiro, "Josephson currents in superconducting tunneling: the effect of microwaves and other observations", *Phys. Rev. Lett.* **11**, pp. 80–82 (1963).

[140] E. Majorana, "Symmetrical theory of electrons and positrons", *Nuovo Cimento.* **14**, pp. 171–184 (1937).

[141] L. P. Rokhinson, Xinyu Liu, and J. K. Furdyna, "The fractional a.c. Josephson effect in a semiconductor–superconductor nanowire as a signature of Majorana particles", *Nature Physics* **8**, pp. 795-799 (2012).

Acknowledgments

The scientific results presented in this thesis are not the work of a single person. Instead, many people contributed to the successful realization.

The basis for the advanced experiments is a well equipped laboratory. Many thanks go to Prof. Dr. Hartmut Buhmann and Prof. Dr. Laurens W. Molenkamp, for giving me the opportunity to realize my ideas beginning with growth and ending with low temperature and high magnetic field characterization. In this context, I also want to thank Dr. Claus Schumacher, Martin Zipf, Volkmar Hock, Petra Wolf-Müller, Carmen Bundschuh, Angelika Berger, Roland Ebert and Cornelius Ziga for technical assistance and of course for their daily affords to keep everything running. Special thanks go to Dr. Christoph Brüne, who wrote the proposal to get financial support from the DPG and thereby organized my salary.

Many thanks for the idea to use ZnTe as a growth start for CdTe NWs grown on GaAs substrates, which was introduced to me by Prof. Dr. Grzegorz Karczewski. In this thesis, all images taken with the transmission electron microscope were recorded by Dr. Nadezda V. Tarakina. The pairing symmetries in superconductors were explained to me by Dr. Grigory Tkachov and Dr. Pablo Burset.

It was a great pleasure to work together with the other PhD students in EP3. Without their help, the solution of many of the day-by-day problems would be nearly impossible. I want to thank Phillip Leubner, Christopher Ames, Rebekka Pfeuffer, Cornelius Thienel, Holger Thierschmann, Felicitas Gerhard, Stefan Schreyeck, Oliver Herrmann, Mirko Trabel, Raimund Schlereth, Simon Hartinger, David Mahler and Martin Baußenwein.

Sharing a room not only with colleagues, but with my friends, was also very beneficial. I thank Kalle Bendias for the huge personal support and the fruitful discussions in all fields. The development of metallic contacts on NWs in this work was based on his explanation of lithographic details. I also thank Andreas Budewitz, who always has a friendly ear for me. He furthermore answered every question I had during the

operation of a dilution refrigerator and explained some parts of the measurement equipment to me.

During my time as a PhD, I supervised the experiments of several Bachelor- and Master-students, who contributed to the scientific output. Lukas Lunczer analyzed strain in NWs for his Bachelor's thesis. Johannes Brehm developed the AuGe-based contacts during his time as a Master-student. Christoph Fleckenstein performed charge transport measurements on the AuGe-devices for his Bachelor's thesis. As a Bachelor-student, Sebastian Krüger investigated the frequency dependence of DEP. My last Bachelor student, Magnus Liebl, characterized the charge transport in samples with Ti-based contacts.

In this context, I want to thank Jan Hajer, who wrote both theses under my supervision. Working together with him was always very nice and effective. He analyzed the formation of eutectic droplets, fabricated many of the samples with superconducting contacts and performed charge transport experiments with these. I can say, I am happy, that he continues as a PhD to start the search for Majorana bound states in our wires. I know for sure, the project is in good hands.

In addition, I want to thank numerous people for the assistance in proof-reading the manuscript.

Danke Anna-Maria, dass du mich ertragen und unterstützt hast, vom ersten Satz meiner Doktorarbeit, bis hin zu diesem letzten.